UNIVERSITE D'AIX-MARSEILLE

Laboratoire de Mécanique, Modélisation et Procédés Propres
- UMR 7340 -

THESE
pour obtenir le grade de
DOCTEUR DE L'UNIVERSITE d'AIX-MARSEILLE
Discipline : ENERGETIQUE
Ecole Doctorale 353, Sciences de l'Ingénieur
présentée et soutenue publiquement
par
Damien FURFARO
le 6 novembre 2015

SIMULATION NUMERIQUE D'ECOULEMENTS MULTIPHASIQUES, PROBLEMES A INTERFACES ET CHANGEMENT DE PHASE

Directeur de thèse : Professeur Richard Saurel – M2P2 – Université d'Aix-Marseille

JURY

M.	SAGAUT P.,	Professeur – M2P2 – Université d'Aix-Marseille (Président)
M.	DUMBSER M.,	Professeur – IT Universita degli studi di Trento (Rapporteur)
M.	LOUBERE R.,	Chargé de recherche CNRS – Université Toulouse 3 (Rapporteur)
M.	SAUREL R.,	Professeur – M2P2 – Université d'Aix-Marseille (Examinateur)

Avant-propos

Je voudrais remercier en tout premier lieu Richard Saurel, pour ses précieux conseils, le temps qu'il m'a consacré et surtout la confiance qu'il m'a accordée. Ses valeurs, sa culture scientifique et sa pédagogie sont pour moi un exemple.

Je tiens également à remercier mes rapporteurs, Messieurs Michael Dumbser, Professeur à l'Université de Trento (Italie) et Raphaël Loubere, chargé de recherche (CNRS) à Toulouse. Leurs remarques et suggestions précieuses m'ont permis de prendre encore plus de recul sur ma problématique. Je tiens de plus à faire part de ma gratitude envers Monsieur Pierre Sagaut, Professeur à l'Université d'Aix-Marseille, pour avoir présidé le jury.

Ces années de doctorat se sont déroulées dans un cadre idéal, toutes les conditions étant réunies pour allier travail, efficacité et épanouissement personnel.

François Fraysse, personne dont la sagesse et les valeurs sont peu communes, n'y est d'ailleurs pas du tout étranger. Les débuts prometteurs de notre binôme laissent présager une belle complicité autant humaine que technique. Je le remercie pour son soutien et ses conseils de qualité.

Un clin d'œil amical à Jeaniffer Vides que j'apprécie beaucoup. Son humour et sa générosité participent vivement à la saine ambiance du quotidien.

Un petit mot aussi sur Sarah Hank, plus exactement Docteur H. Une personne vraie tout simplement, avec qui j'ai eu la chance de partager de bons moments durant cette thèse. Je lui souhaite beaucoup de réussite.

Et que dire de « Monsieur le Magicien »? Si vos problèmes numériques persistent malgré des journées d'efforts, faites appel à Boniface Nkonga. Dans les heures qui suivront, votre contrariété ne sera plus qu'un mauvais souvenir! Sa bonne humeur constante ne fait qu'amplifier le plaisir de travailler avec lui.

Un clin d'œil à Pierre Boivin, avec qui j'ai la chance de partager la même passion pour la musique et peut-être bientôt le vélo ? Je tiens aussi à saluer Alexandre Chiapolino à qui je souhaite le meilleur pour sa thèse à venir.

Je tiens de plus à exprimer mon profond respect et mon amitié à Sergey Gavrilyuk, auprès de qui j'ai beaucoup appris.

Je souhaiterais remercier mes parents pour le soutien inconditionnel qu'ils m'ont apporté. Le moindre doute est très vite effacé grâce à leurs précieux et sages conseils et chaque réussite est fêtée. Cette thèse aura été placée sous les signes de l'effort et de la confiance en l'avenir qu'ils ont su encourager avec brio. Je suis très chanceux de les avoir à mes côtés.

Enfin, mes pensées vont vers la personne que j'aime et qui se reconnaîtra à la lecture de ces lignes. Sa présence et son soutien m'ont permis de franchir cette étape avec la confiance et la détermination nécessaires.

Table des matières

Introduction générale…………………………………………………………………………………… 1

1. Un solveur de Riemann de type HLLC dans le cadre d'écoulements diphasiques compressibles en déséquilibre total………………………………………………………….. 14

1.1. Introduction…………………………………………………………………………………………… 14
1.2. Two-phase flow model and properties……………………………………………………… 17
1.3. Local constants and local conservative formulation…………………………………… 18
  1.3.1. DEM basis………………………………………………………………………………… 18
  1.3.2. Determination of the interfacial variables u_I and P_I ……………………………… 19
1.4. Two-phase Riemann solver………………………………………………………………………… 21
  1.4.1. Wave speed estimates $S_{L,k}$, $S_{R,k}$ and $S_{M,k}$ ……………………………………… 22
  1.4.2. Determination of the intermediate states ……………………………………… 22
  1.4.3. Summary………………………………………………………………………………… 25
  1.4.4. Solution sampling……………………………………………………………………… 26
1.5. Entropy preserving…………………………………………………………………………………… 26
1.6. Godunov type scheme……………………………………………………………………………… 28
1.7. Computational examples and validations………………………………………………… 31
  1.7.1. Velocity disequilibrium two-phase flow tests ……………………………………… 32
  1.7.2. Velocity equilibrium two-phase flow tests ………………………………………… 38
  1.7.3. 3D computations……………………………………………………………………… 40
1.8. Conclusion……………………………………………………………………………………………… 45
Appendix 1.A. HLLC Riemann solver when $S_{L,k} < u_I < S_{M,k} < S_{R,k}$ ……………………………… 45
Appendix 1.B. Stiff velocity relaxation solver……………………………………………………… 47
Appendix 1.C. Stiff pressure relaxation solver……………………………………………………… 48
Appendix 1.D. Non conservative terms in the numerical scheme – Other flow configurations…………………………………………………………………………… 49

2. Construction d'une technique numérique pour la répartition de l'énergie d'une onde de choc dans les différentes phases………………………………………………… 51

2.1. Introduction…………………………………………………………………………………………… 51
2.2. Modification of the numerical method to preserve convergence at two-phase shocks…………………………………………………………………………………………………… 54
  2.2.1. Presentation of the 1D method……………………………………………………… 54
  2.2.2. Multi-dimensional extension on tetrahedral meshes…………………………… 58
  2.2.3. Tests on reflected shock waves……………………………………………………… 61
2.3. Conclusion……………………………………………………………………………………………… 63

3. Extension du solveur de Riemann de type HLLC au cas multiphasique................ 64
3.1. Introduction..64
3.2. Multiphase Riemann solver..67
3.2.1. Local conservative formulation...67
3.2.2. Phase k wave pattern.. 67
3.2.3. Comment on Rankine-Hugoniot relations..69
3.2.4. Determination of the Riemann problem solution state – Algorithm........... 70
3.3. Godunov type scheme 72
3.4. Computations and validations.. 73
3.4.1. Three-phase shock tube test...73
3.4.2. Three-phase 3D impact test.. 74
3.5. Conclusion...75
Appendix 3.A. Determination of the contact surfaces at the cell boundaries for an arbitrary number of fluids...75
Appendix 3.B. Noble-Abel EOS... 77

4. Modélisation du changement de phase de gouttelettes liquides en présence d'un gaz multi-constituant.. 79
4.1. Introduction...79
4.2. Two-phase flow model and properties.. 81
4.3. Conventional closure relations... 82
4.3.1. Equations of state...82
4.3.2. Interfacial variables... 83
4.3.3. Mechanical relaxation rates... 84
4.4. Building the symmetric heat and mass transfer model... 86
4.4.1. Interface conditions.. 86
4.4.2. Examination of the mass interface condition 87
4.4.3. Examination of the energy jump relation at the interface.......................... 89
4.5. Local thermodynamic equilibrium..91
4.6. Heat exchanges...92
4.6.1. Short-term solutions... 93
4.6.2. Long-term solutions.. 94
4.6.3. Validation...95
4.7. Solving the local heat and mass transfer model.. 98
4.8. Computational examples and validations... 101
4.8.1. Relaxation towards equilibrium...101
4.8.2. Shock tube with droplets...102
4.8.3. 3D explosive liquid water test-case.. 107
4.9. Conclusions...108
Appendix 4.A. Phase equilibrium..108

Conclusion générale.. 110
Références...111

Introduction générale

Les écoulements multiphasiques suscitent depuis longtemps un réel engouement de la part des industriels et des scientifiques. Leur champ d'applications est très vaste de par la richesse de la physique qu'ils contiennent, il touche d'ailleurs la plupart des secteurs industriels. Les capacités informatiques étant aussi en plein essor, la simulation numérique de ces écoulements complexes devient de plus en plus abordable.

Les écoulements qui suscitent notre intérêt mettent en jeu des phénomènes complexes et divers. Généralement, les vitesses et pressions sont élevées. Dans le cas d'une explosion par exemple, la vitesse du gaz peut atteindre des valeurs de l'ordre de plusieurs milliers de m/s, et la pression du milieu peut être de plusieurs centaines de milliers de Bars (Figure A). Les secteurs de la Défense et du Spatial sont ainsi particulièrement visés.

Figure A : Explosion d'une charge initialement placée dans du sable.

Ces conditions extrêmes s'accompagnent de la propagation d'ondes de choc, de détente, de discontinuités de contact, d'ondes de détonation, de transition de phase,… Les phénomènes de propagation sont ainsi très présents et la modélisation envisagée doit nécessairement reposer sur des équations hyperboliques. En effet, les phénomènes de propagation ne peuvent être reproduits par des modèles non-hyperboliques, bien que ceux-ci soient encore largement utilisés dans certaines communautés.

La simulation d'écoulements en conditions extrêmes nécessite aussi la prise en compte de la compressibilité d'au moins un des fluides qui constituent le milieu. Il en est de même pour l'étude de phénomènes tels que la transition de phase rapide (cavitation et flashing) pour lesquels une approche incompressible serait tout-à-fait inadaptée.

Nous nous intéressons de plus au traitement des interfaces entre fluides ainsi qu'aux milieux en déséquilibre de vitesse. Un exemple simple permet de comprendre ces motivations.
Prenons le cas d'une charge explosive cylindrique composée d'un gaz dense pur et entourée d'une couche d'eau liquide. L'ensemble gaz dense – eau liquide est placé à l'air libre (Figure B).

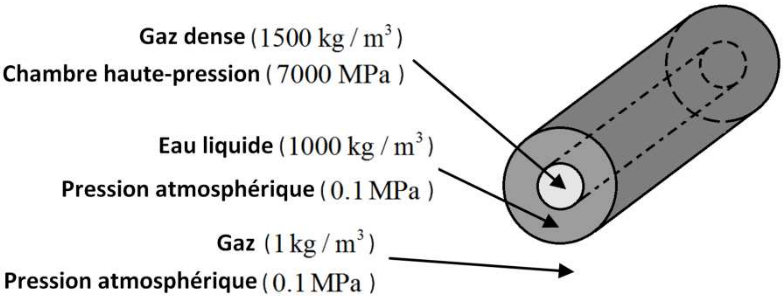

Figure B: Représentation schématique d'une explosion cylindrique gaz-liquide

Nous sommes initialement en présence de deux interfaces séparant des fluides purs :
- gaz dense / eau liquide
- eau liquide / gaz à pression atmosphérique

Dans les premiers instants de l'explosion, le fort gradient de pression implique la déformation et la propagation de ces interfaces. Leur suivi est par définition indispensable à la bonne compréhension du phénomène étudié. De plus, en chaque point de l'écoulement, une seule vitesse est à considérer : celle du fluide pur présent localement.
Au bout d'un certain temps, l'eau liquide qui était jusqu'alors considérée comme une seule et unique masse de fluide pur se transforme petit à petit en un nuage de gouttes sous la violence de l'écoulement. Le brouillard obtenu (mélange Gaz – Eau liquide) nécessite alors la connaissance des vitesses de chacun des fluides. En effet, chaque volume infinitésimal considéré au sein de l'écoulement est alors constitué d'un mélange de 2 fluides, chacun avec sa propre vitesse (Figure C).

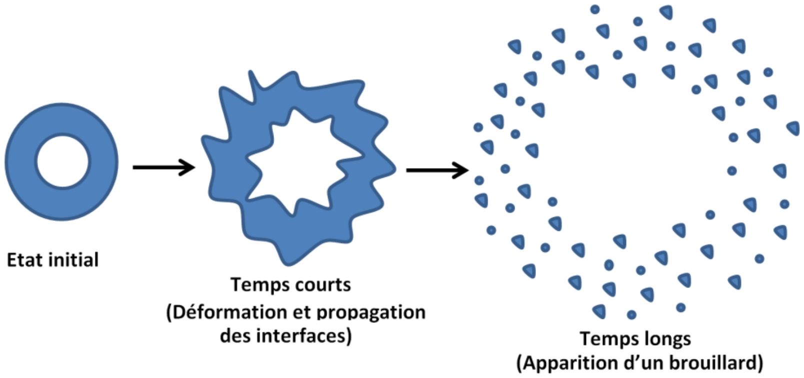

Figure C: Devenir des interfaces gaz/eau dans le cas de l'explosion d'une charge cylindrique placée à l'air libre.

Ainsi, il est nécessaire d'opter pour un modèle multi-vitesses capable de traiter correctement la déformation, propagation et création d'interfaces.

Deux types de méthodes numériques se distinguent pour le traitement des problèmes à interfaces.

Méthodes à diffusion nulle ou quasi-nulle

Elles sont pour la plupart basées sur la localisation de l'interface.

- Certaines de ces méthodes considèrent des maillages mobiles (méthodes Lagrangiennes (Benson, 1992) et ALE (Farhat et Roux, 1991)). Cependant, de nombreuses complications apparaissent dans le cas d'interfaces fortement déformées ou lors d'apparition de nouvelles interfaces.
- Les méthodes de « Front tracking ». Le caractère conservatif des équations est cependant mis en défaut dans les problèmes 2D et 3D.
- Les méthodes de « Reconstruction d'interface » donnent apparemment de bons résultats mais ne sont pas (ou peu) adaptées au traitement des écoulements compressibles.
- Enfin, les méthodes Level Set (Mulder et al., 1992) donnent des résultats visuels remarquables mais restent non-conservatives.

Les méthodes à diffusion quasi-nulle présentent des avantages évidents, mais les pertes de conservation dans les cas 2D et 3D, ainsi que l'importance des temps de calcul et de développement nous incitent à opter pour le type de méthode qui suit.

Méthode autorisant la diffusion numérique de l'interface

Dans cette approche, une ou plusieurs interfaces sont susceptibles de traverser une cellule de discrétisation du domaine. Dans ces mailles dites de « mélange », plusieurs fluides cohabitent avec leur propre thermodynamique (Figure D). Il est par nature impossible de construire des paramètres d'état pour ces cellules par une simple moyenne des paramètres thermodynamiques des fluides purs qui la composent. En effet, des problèmes numériques importants résulteraient de cette approche, comme des oscillations de vitesse et de pression aux interfaces ou plus simplement l'échec du calcul.

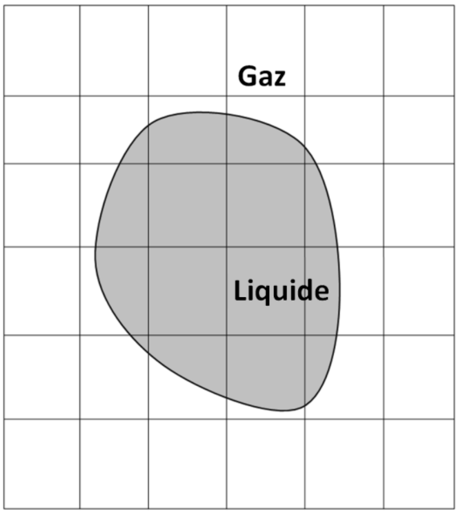

Figure D : Mise en évidence de l'existence de mailles de mélange traversées par une interface. Ici, cas d'une interface liquide/gaz sur un maillage fixe.

Pour compenser cela, il s'agit de considérer des modèles eulériens diphasiques introduisant explicitement la notion de volume partiel occupé par chaque fluide. Une équation de transport de la fraction volumique de chaque fluide (rapport entre le volume occupé par le fluide et le volume du mélange) est alors considérée. Le choix de cette approche implique certes la représentation de l'interface par une zone diffuse, mais la mise en œuvre informatique est beaucoup plus simple et robuste que les méthodes à diffusion nulle.

Le modèle eulérien diphasique compressible de référence est celui de Baer & Nunziato (BN) (1986). Ce modèle hyperbolique est le plus général possible, chaque fluide possédant sa propre densité, vitesse et pression, évoluant dans son propre sous-volume. Au-delà du traitement des problèmes à interfaces, cette approche peut être reprise dans des domaines divers. La formulation multi-vitesses permet le traitement d'une large gamme d'applications (écoulements à bulles, brouillard, milieux granulaires,…).

Le présent travail de thèse s'intéresse donc particulièrement au modèle de Baer et Nunziato (1986), à sa résolution numérique, aux écoulements hors d'équilibre des vitesses ainsi qu'aux interfaces entre fluides.

Dans le domaine des méthodes numériques, de nombreuses contributions (Andrianov and Warnecke (2004), Schwendeman et al. (2006), Deledicque and Papalexandris (2007), Tokareva and Toro (2010), …) ont été apportées dans le cadre de l'étude du problème de Riemann pour le système de Baer et Nunziato.

Ce modèle présente une particularité qui rend complexe la recherche de méthodes numériques permettant de le résoudre. Les interactions entre phases sont en effet décrites par des termes non-conservatifs. Notons d'ailleurs que le respect des conditions d'interface est assuré par la présence de ces termes.

Les équations écrites pour chaque phase en termes de variables conservatives ne se présentent donc pas sous forme conservative. Il est alors difficile de définir sans ambiguïté les relations de Rankine-Hugoniot appliquées aux chocs et de déterminer la discrétisation appropriée des termes correspondants.

La plupart des solveurs de Riemann précités se basent sur des solveurs à 6 ondes avec une méthode de régularisation pour l'onde interfaciale, celle-ci étant en effet dégénérée dans le modèle BN.

De plus, à la connaissance des auteurs, il n'est pas assuré que ces solveurs soient suffisamment robustes dans le cadre d'écoulements en conditions sévères. Nous prendrons pour exemples les détonations et explosions en présence d'importants gradients de fraction volumique (cas des interfaces), et d'importants gradients de pression.

Pour surmonter cette difficulté, la Méthode des Equations Discrètes (DEM) a été proposée par Abgrall et Saurel (2003). Contrairement aux approches citées précédemment, la DEM ne se base pas sur un système donné d'EDPs. Dans cette méthode, la maille diphasique est divisée en deux sous-volumes, chacun correspondant à une phase donnée. Sur chaque bord de maille, le problème de Riemann pour les équations d'Euler est résolu. Ces solutions sont ensuite moyennées dans chaque sous-volume et sont à l'origine d'un système d'équations discrètes. Le passage à la limite continue (Saurel et al., 2003), lorsque les pas de temps et d'espace tendent vers zéro, permet l'obtention d'une variante symétrique du modèle BN. Le terme « symétrique » signifie que les indices des phases peuvent être inversés sans pour autant modifier la formulation finale du modèle.

La robustesse et la précision de la DEM ont été vérifiées dans le cadre d'écoulements à interfaces (Abgrall and Saurel, 2003), ondes de détonation dans les explosifs hétérogènes (Chinnayya et al., 2004), chocs en milieux multiphasiques (Saurel et al., 2007),…

Cette robustesse a pour origine le « bon » calcul des produits non-conservatifs, via l'étude d'un problème physique de diffraction d'ondes. Ces termes non-conservatifs sont par exemple $u_I \frac{\partial \alpha}{\partial x}$ ou $P_I \frac{\partial \alpha}{\partial x}$, où u_I et P_I représentent respectivement les vitesse et pression d'interface, et α la fraction volumique de l'un des fluides . Lorsqu'une onde de choc interagit avec une discontinuité de fraction volumique, u_I et P_I peuvent être des fonctions de Heaviside, alors que le gradient de α peut être un Dirac. Lors de l'interaction, le choc est diffracté en un choc plus faible transmis et une onde de détente réfléchie, permettant ainsi de considérer les pression et vitesse constantes dans la zone diffractée (Figure E). Le produit d'une constante avec une fonction Dirac (gradient de fraction volumique) est ainsi bien défini et les termes non-conservatifs perdent toute ambiguité.

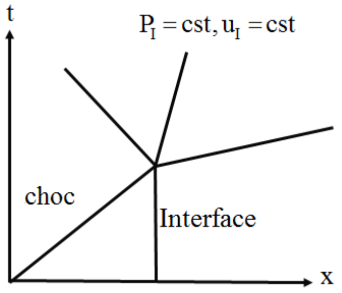

Figure E : Diffraction du choc à l'interface en un choc plus faible transmis et une onde de détente réfléchie

Cependant, cette méthode n'est pas simple à implémenter et implique des temps de calcul quelque peu élevés. Ces deux arguments ont motivé l'étude réalisée dans le chapitre 1 au sein duquel un solveur de Riemann diphasique de type HLLC robuste, rapide et précis est développé. Son implémentation est simple, ce qui est très important pour le développement d'un code multiphasique 3D.

Un solveur de Riemann de type HLLC dans le cadre d'écoulements diphasiques compressibles en déséquilibre total (Chapitre 1)

La méthode numérique que nous allons proposer se base sur la variante symétrique du modèle de Baer & Nunziato proposée par Saurel et al. (2003) et obtenue dans le cadre de l'étude de la limite continue des équations discrètes de la DEM.

Le modèle est un système d'EDPs hyperbolique, chaque phase possédant ses propres équations de bilan (masse $(\alpha_k \rho_k)$, quantité de mouvement $(\alpha_k \rho_k u_k)$ et énergie $(\alpha_k \rho_k E_k)$, $k = 1,2$). Une équation sur la fraction volumique (α_k) assure le transport de celle-ci à la vitesse de l'interface. Le modèle peut s'écrire sous la forme suivante :

$$\frac{\partial U_k}{\partial t} + \frac{\partial F_k}{\partial x} + \alpha_k \frac{\partial H_k}{\partial x} = 0, \ \forall k \in \{1,2\} \qquad \text{(A)}$$

avec $U_k = \begin{pmatrix} \alpha_k \\ (\alpha\rho)_k \\ (\alpha\rho u)_k \\ (\alpha\rho E)_k \end{pmatrix}$; $F_k = \begin{pmatrix} \alpha_k u_I \\ (\alpha\rho u)_k \\ \alpha_k \left(\rho u^2 + P\right)_k - \alpha_k P_I \\ \alpha_k \left(\rho E + P\right)_k u_k - \alpha_k P_I u_I \end{pmatrix}$ et $H_k = \begin{pmatrix} -u_I \\ 0 \\ P_I \\ P_I u_I \end{pmatrix}$.

Le solveur de Riemann diphasique de type HLLC que nous proposons fait évoluer 4 ondes par phase, c'est-à-dire les trois ondes conventionnelles plus une onde dite 'interfaciale'.

Inspirée par la Méthode des Equations Discrètes (Abgrall et Saurel, 2003), cette vitesse d'onde u_I est supposée fonction uniquement des états initiaux et se calcule ainsi facilement à partir de ces états. Il en est de même pour la pression d'interface P_I. Les variables interfaciales u_I et P_I sont ainsi localement constantes dans le cadre de l'étude du problème de Riemann.

Il n'y a ainsi aucune difficulté à exprimer le système (A) d'EDPs non conservatives sous une forme localement conservative :

$$\frac{\partial U_k}{\partial t} + \frac{\partial F_k}{\partial x} = 0\,,\ \forall k \in \{1,2\}$$

A l'aide des vitesses d'onde HLLC conventionnelles et de l'onde interfaciale supplémentaire, le problème de Riemann faisant intervenir 4 ondes par phase est résolu selon la même stratégie que celle adoptée par Toro et al. (1994) pour les équations d'Euler. Comme u_I et P_I sont fonctions uniquement des données initiales du problème de Riemann, le problème de Riemann diphasique est réduit à deux problèmes de Riemann indépendants constitués uniquement de 4 ondes chacun.

Il sera par ailleurs montré que le solveur de Riemann proposé est en accord avec la seconde loi de la thermodynamique. De plus, la méthode numérique proposée a été validée à partir de solutions exactes et de données expérimentales et comparée à des résultats numériques issus de la DEM.

La méthode est par la suite étendue au cas 3D, dans le cadre de maillages non-structurés tétraédriques.

La capacité de la méthode numérique à simuler des écoulements diphasiques compressibles a été présentée et justifiée. Il est toutefois important de remarquer que le traitement numérique de la propagation d'ondes de chocs dans un milieu hétérogène présente quelques difficultés, même lorsque la fraction volumique ne présente initialement aucun gradient. Les équations diphasiques étant non-conservatives, les relations de saut sont non triviales et les conditions de choc présentées dans Saurel et al. (2007) doivent être imposées numériquement pour que la dynamique des ondes de chocs soit respectée. La partie qui suit présente ainsi une méthode permettant le respect des conditions de choc multiphasiques.

Construction d'une technique numérique pour la répartition de l'énergie d'une onde de choc dans les différentes phases (Chapitre 2)

Lorsqu'une onde de choc (ou de détonation) se propage dans un milieu hétérogène le calcul de sa dynamique nécessite la correcte répartition de son énergie dans les différentes phases en présence. La difficulté principale consiste à « forcer » cette répartition au niveau discret, en accord avec les relations de choc de Saurel et al. (2007).

Ce problème de convergence est une conséquence de la diffusion numérique du front de choc. Celui-ci est résolu numériquement comme une succession de faibles chocs dont le chemin thermodynamique est différent du chemin thermodynamique qui serait suivi par le passage d'un seul choc fort.

Il est intéressant de remarquer que le chemin thermodynamique suivi par le fluide à l'intérieur de la couche de choc numérique et sa courbe d'Hugoniot théorique sont très différents (voir Figure F). Ceci est dû à la succession de chocs faibles qui se propagent de maille en maille et qui n'imposent pas la même transformation thermodynamique qu'un seul choc fort (Courant and Friedrichs, 1948). Pour chaque choc faible se propageant dans une maille de calcul, l'équation d'état est modifiée due à la présence de la fraction volumique (variable non-conservative) dans le cas d'un mélange. Ainsi, en un point donné de la couche de choc numérique, il n'y a aucune chance pour que ce point appartienne à la courbe d'Hugoniot diphasique théorique. Ceci implique que la fraction volumique est mal calculée, imposant ainsi une erreur sur l'équation d'état du mélange. Ces différentes erreurs s'accumulent le long de la couche de choc et l'état final n'appartient pas à la courbe d'Hugoniot du mélange.

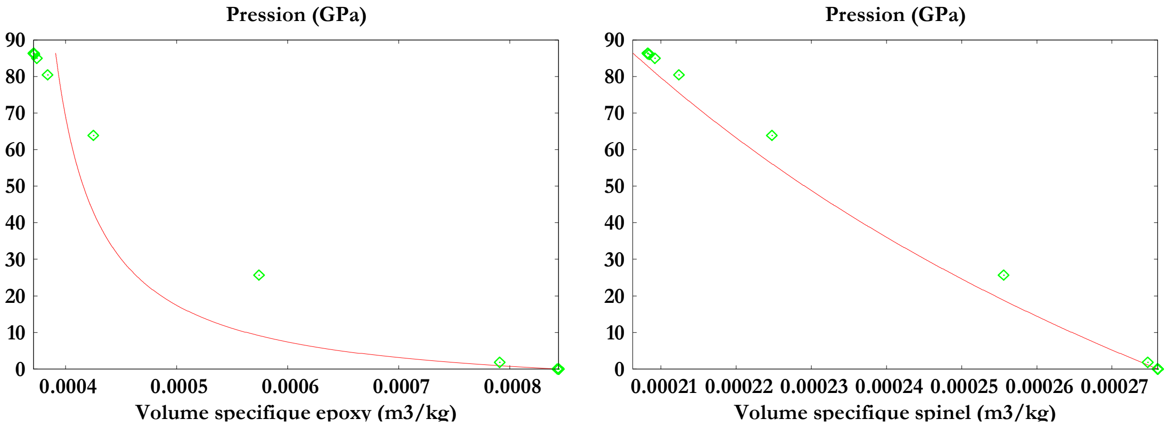

Figure F : Comparaison entre le chemin thermodynamique suivi dans la couche de choc numérique (symboles) et les courbes d'Hugoniot théoriques (trait) dans le cas d'un mélange Epoxy-Spinel. Le chemin thermodynamique ne suit pas les courbes d'Hugoniot théoriques et dans ce cas, l'état final n'est pas correctement calculé.

Pour permettre la convergence de la solution, des échanges de chaleur artificiels ont été introduits au sein de la couche de choc de manière à répartir correctement les énergies entre phases (Petitpas et al., 2007). Cette méthode s'est avérée présenter un certain nombre d'inconvénients.

Petitpas et al. (2009) ont ensuite proposé une méthode plus simple et efficace. Elle consiste à corriger le chemin thermodynamique à l'intérieur de la couche de choc numérique en forçant chaque point de la zone de diffusion à appartenir aux courbes d'Hugoniot théoriques (Figure G).

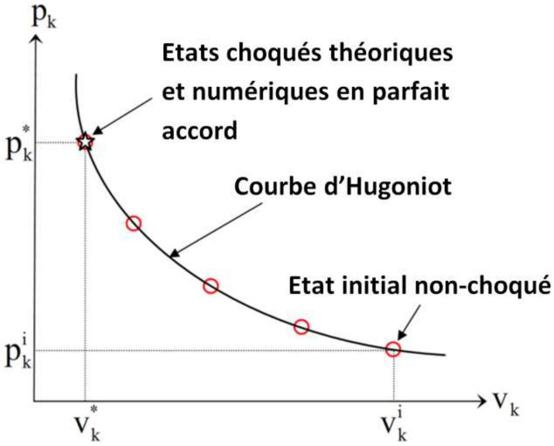

Figure G : Chaque point de la couche de choc numérique est forcé à appartenir à la courbe d'Hugoniot théorique, de façon à retrouver le bon état choqué.

Pour réussir à faire cette correction, il est nécessaire de garder la « mémoire » des états initiaux non choqués (c'est-à-dire les pressions et volumes spécifiques devant le choc) $\left(p_k^i, v_k^i\right)$. Ceci est assuré par l'ajout de nouvelles équations au système :

$$\begin{cases} \dfrac{d_k p_k^i}{dt} = 0 \\ \dfrac{d_k v_k^i}{dt} = 0 \end{cases}$$

Ainsi, durant la phase de relaxation des pressions et des vitesses à l'intérieur d'une couche de choc numérique, il devient possible de remplacer les formes intégrales des équations d'énergie en imposant que chacune des phases reste sur sa propre courbe d'Hugoniot :

$$\forall k, \quad e_k^*\left(p^*, v_k^*\right) - e_k^i\left(p_k^i, v_k^i\right) + \frac{p + p_k^i}{2}\left(v_k^* - v_k^i\right) = 0$$

En utilisant ces nouvelles relations dans la même étape de relaxation, il devient possible de déterminer les pressions et volume spécifiques relaxés. De cette façon, à la fin de l'étape de relaxation, les volumes spécifiques sont en parfaite adéquation avec les courbes d'Hugoniot des phases et du mélange en chaque point de la zone de diffusion du choc.

Cette correction doit être effectuée dans la couche de choc seulement. Un indicateur de choc doit alors être utilisé pour détecter les mailles dans lesquelles un choc est présent. Ce point n'est pas discuté dans Petitpas et al. (2009) bien que non-trivial.

Dans le chapitre 2, nous réalisons une extension de cette méthode aux maillages non-structurés 3D et mettons en place une procédure robuste et efficace de détection des chocs.

Il s'agit maintenant de décrire l'extension de la méthode 'HLLC diphasique' (chapitre 1) à un nombre arbitraire de phases. En effet, les applications qui nous intéressent font souvent intervenir plus de deux milieux, un milieu étant caractérisé par une équation d'état avec son jeu de paramètres. Ainsi, il est fréquent d'utiliser le code pour décrire un écoulement faisant intervenir deux gaz et un solide, chaque phase ayant sa propre thermodynamique.

Extension du solveur de Riemann de type HLLC au cas multiphasique (Chapitre 3)
Comme énoncé précédemment, le point de départ de la nouvelle méthode diphasique est la limite continue du système d'équations discrètes obtenues dans le cadre de la DEM diphasique.

La mise en place d'un solveur de type HLLC multiphasique nécessitant la donnée d'un modèle continu, l'idée naturelle consiste, à partir de la DEM généralisée à un nombre arbitraire N de fluides, à chercher la limite continue du système discret obtenu.

De la même manière que dans le cas diphasique, chaque maille est divisée en N sous-volumes, chacun correspondant à une phase donnée. Sur chaque bord de maille, le problème de Riemann pour les équations d'Euler est résolu. Ces solutions sont ensuite moyennées dans chaque sous-volume et sont à l'origine d'un système d'équations discrètes (voir Figure H – cas d'un écoulement tri-phasique).

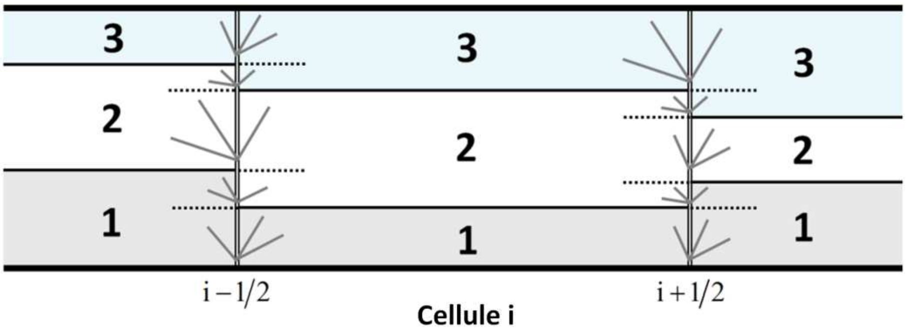

Figure H : Exemple de topologie stratifiée d'écoulement tri-phasique. De la même manière que dans le cas diphasique, le problème de Riemann pour les équations d'Euler est résolu sur chaque bord de maille et pour chaque type de contact.

Cependant, le passage à la limite continue du système discret à N phases est beaucoup plus complexe que dans le cas diphasique, la forme continue des termes non-conservatifs étant extrêmement complexe. L'idée est donc de baser la méthode multiphasique sur un modèle semi-discret avec :

- les termes temporels et conservatifs sous forme continue,
- les termes non-conservatifs sous forme discrète.

Le modèle multiphasique semi-discret considéré s'écrit, $\forall k \in \{1,...,N\}$:

$$\frac{\partial U_k}{\partial t} + \frac{\partial F_k}{\partial x} = \frac{\sum_{l,m}\left(h\left[\chi_k^*\right]F^{*,lag}\right)_{lm,i-1/2} + \sum_{l,m}\left(h\left[\chi_k^*\right]F^{*,lag}\right)_{lm,i+1/2}}{\Delta x}, \tag{B}$$

avec

$$U_k = \begin{pmatrix} \alpha_k \\ \alpha_k\rho_k \\ \alpha_k\rho_k u_k \\ \alpha_k\rho_k E_k \end{pmatrix}, \; F_k = \begin{pmatrix} 0 \\ \alpha_k\rho_k u_k \\ \alpha_k\left(\rho_k u_k{}^2 + P_k\right) \\ \alpha_k\left(\rho_k E_k + P_k\right)u_k \end{pmatrix} \text{ et } F_{lm}^{Lag,*} = \left(-u_{lm}^* \quad 0 \quad P_{lm}^* \quad P_{lm}^* u_{lm}^*\right)^T,$$

où :

- $(l,m) \in \{1,...,N\} \times \{1,...,N\}$ sont les indices des phases ($l \neq m$),

- h_{lm} est la hauteur du canal représentant le contact 'l-m' sur un bord de maille donné,
- $\left[\chi_k^*\right]_{lm}$ est le saut de fonction de phase suivant la direction x à travers le contact 'l-m',
- $F_{lm}^{Lag,*}$ est le flux Lagrangien solution du problème de Riemann pour les équations d'Euler et pour le contact 'l-m' sur un bord de maille donné.

Une fois les définitions posées, il s'agit de considérer le problème de Riemann local. De la même manière que les variables interfaciales u_I et P_I dans le cas diphasique, les vitesse u_{lm}^* et pression P_{lm}^* présentes dans les termes non-conservatifs sont solutions du problème de Riemann pour les équations d'Euler et pour le contact 'l-m', et sont ainsi localement constantes. Les hauteurs h_{lm} sont aussi constantes pour un bord de maille donné. En gardant à l'esprit que $\Delta x = \varepsilon << 1$, le système (B) s'écrit naturellement sous la forme localement conservative :

$$\frac{\partial U_k}{\partial t} + \frac{\partial\left(F_k - \sum_{l,m}\left(hF^{*,lag}\chi_k\right)_{lm}\right)}{\partial x} = 0$$

De plus, la constance locale des variables u_{lm}^* et P_{lm}^* permet de justifier le fait que le problème de Riemann pour une phase donnée est découplé de ceux des autres phases.

Une extension 3D de la méthode multiphasique dans le cadre d'un maillage non-structuré a été réalisée suivant le même principe que dans le cas diphasique. Dans les Figures I et J, un exemple d'impact de projectile en cuivre sur une cuve en cuivre remplie d'eau est présenté. Le reste du domaine est constitué d'air quasi-pur. Dans ce cas-test, les solveurs de relaxation instantanée des pressions et des vitesses sont activés.

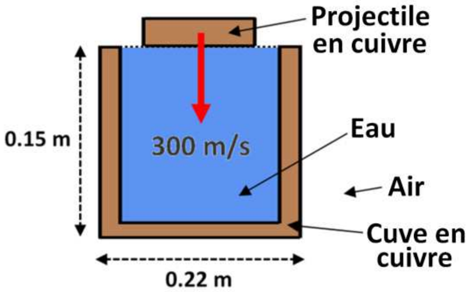

Figure I: Test d'impact - état initial

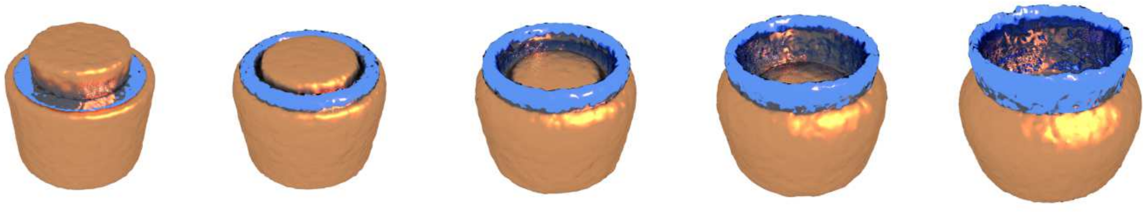

Figure J: Test d'impact – Résultats numériques à différents instants.
($t = 0$, $t = 90\mu s$, $t = 170\mu s$, $t = 250\mu s$ et $t = 360\mu s$).

Tout ce qui précède considère les phases comme non-dissipatives, la seule dissipation apparaissant dans les ondes de choc. Cependant, dans les écoulements diphasiques, de nombreux autres phénomènes dissipatifs sont présents et apparaissent aux interfaces du milieu diphasique (bulles, gouttes, …). Il s'agit des transferts de chaleur, de masse et de quantité de mouvement.
Le chapitre qui suit porte sur la modélisation des transferts de chaleur et de masse dans un brouillard de gouttes ou nuage de bulles, en présence d'effets couplés de diffusion thermique et massique.

Modélisation du changement de phase de gouttelettes liquides en présence d'un gaz multi-constituant (Chapitre 4)
Les écoulements constitués de gouttelettes liquides dispersées au sein d'un gaz multi-constituant en présence d'évaporation et de condensation apparaissent dans de nombreuses applications liées aux écoulements diphasiques (combustion dans les moteurs d'automobiles ou de fusées, combustion cryogénique,…). Le gaz peut par exemple être composé de vapeur d'eau et d'autres espèces chimiques telles que l'air.

L'objectif de la présente approche est de modéliser les échanges de chaleur et de masse dans le cadre du mécanisme d'évaporation/condensation en vue d'une insertion dans le modèle d'écoulement (A).
Le mélange considéré est constitué d'un gaz multi-constituant (g) et d'une phase liquide dispersée (L).
L'équation de bilan de masse de la phase gazeuse a été remplacée par deux équations d'évolution des fractions massiques des espèces composant le gaz. Le gaz est en effet constitué d'air et de vapeur d'eau dont les fractions massiques sont respectivement définies par les variables $Y_{g,air}$ et $Y_{g,wat}$.
Par ailleurs, l'ajout d'une équation sur le nombre de gouttelettes d'eau liquide par unité de masse permet la connaissance de l'aire interfaciale A_I entre les phases liquide et gazeuse.
Les termes de transfert de chaleur et de masse sont implémentés en tant que termes sources. Les inconnues relatives à ces transferts sont les suivantes:

- le débit massique de gaz $\dot{m}_g$,
- la température d'interface T_I,
- la fraction massique $Y_{g,wat,I}$ de vapeur d'eau dans le gaz déterminée à l'interface,
- le coefficient d'échange de chaleur au sein de la phase liquide H_{TL}.

La détermination de ces 4 inconnues va résulter d'un système algébrique à 4 équations, fortement non-linéaire, qui est établi dans le chapitre 4.

De nombreux efforts ont été réalisés dans cette direction, principalement dans le cadre de la combustion de sprays diphasiques (Spalding (1953), Williams (1958), Law (1982), Abramzon et Sirignano (1989), Abramzon et Sazhin (2005), Sirignano (2014),…).

Notre contribution suit les lignes directrices d'Abramzon et Sirignano (1989) (AS89) dans le sens où :

- la méthode permet le calcul des effets de diffusion de chaleur et de masse à l'interface,

- le chauffage de la gouttelette est considéré au-travers d'un coefficient d'échange de chaleur entre l'interface liquide-gaz et le cœur de la gouttelette.

Cependant, le modèle AS89 cherche en particulier à traiter la combustion de sprays. Dans de telles situations, le changement de phase se produit comme la conséquence d'un échange de chaleur entre le gaz chaud et la gouttelette initialement froide. Mais dans des situations différentes de la combustion de sprays, un taux de transfert de masse non nul peut provenir de l'énergie déjà emmagasinée au sein de la gouttelette liquide.

Dans notre approche, les contraintes de saturation, la masse et l'énergie à l'interface étant liées de manière non-linéaire, le flashing est désormais possible alors que seule l'évaporation l'était dans les modèles cités précédemment (Figure K). De plus, les équations à l'échelle locale (celle de la goutte) sont en parfait accord avec le système diphasique d'EDPs moyennées en volume.

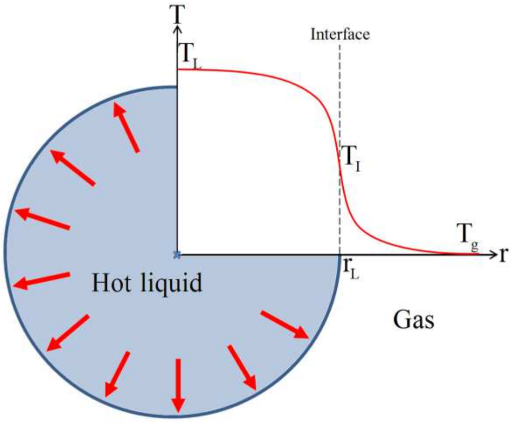

Figure K: Représentation d'une goutte liquide dont la température est plus grande que celle du gaz environnant. Le modèle proposé est symétrique et permet l'apparition de flashing.

Rappelons que le modèle local présenté dans le chapitre 4 se base sur la configuration d'une goutte de liquide pur entourée d'un gaz multi-constituant composé d'air et de vapeur d'eau. La construction du modèle passe par la considération d'équations de bilan locales (conservation de la masse de chaque espèce $i \in \{air, wat\}$ dans une phase donnée $k \in \{L, g\}$ et conservation de l'énergie pour chaque phase k).

L'intégration de ces équations sur une interface conduit à deux équations algébriques :

- $$\dot{m}_g = \frac{\rho_g H_{Mg} \left(Y_{g,wat,I} - Y_{g,wat,\infty} \right)}{1 - Y_{g,wat,I}}, \quad \text{(C)}$$

  où $Y_{g,wat,\infty}$ représente la concentration de vapeur d'eau dans la phase gazeuse loin de l'interface et où H_{Mg} est le coefficient d'échange de masse dans la phase gazeuse déterminé à l'aide de la définition du nombre de Sherwood.

- $$\dot{m}_g = \frac{H_{Tg} \left(T_{g,\infty} - T_I \right) + H_{TL} \left(T_c - T_I \right)}{L_{v,wat} \left(T_I \right)}, \quad \text{(D)}$$

  où H_{Tg} est le coefficient d'échange de chaleur dans la phase gazeuse obtenu à l'aide du nombre de Nusselt, $L_{v,wat}(T_I)$ représente la chaleur latente de vaporisation, et où $T_{k,\infty}$

représente la température de la phase k loin de l'interface. En particulier, $T_{L,\infty} = T_c$, la température du cœur de la goutte.

Par ailleurs, l'interface est considérée à l'équilibre thermodynamique local, ce qui donne une troisième équation :

$$Y_{g,wat,I} = \frac{M_{g,wat}}{\hat{M}_g\left(Y_{g,wat,I}\right)} \frac{P_{sat,wat}\left(T_I\right)}{P} \tag{E}$$

où $\frac{1}{\hat{M}_g} = \frac{Y_{g,wat,I}}{M_{g,wat}} + \frac{1-Y_{g,wat,I}}{M_{g,air}}$, avec $\begin{cases} M_{g,air} = 29\times10^{-3}\,\text{kg.mol}^{-1} \\ M_{g,wat} = 18\times10^{-3}\,\text{kg.mol}^{-1} \end{cases}$ et où $P_{sat,wat}\left(T_I\right)$ représente la pression de saturation de l'eau à la température de l'interface.

Le modèle algébrique local d'échange de chaleur et de masse est ainsi constitué des équations (C), (D) et (E). Il reste à déterminer le coefficient d'échange de chaleur au sein de la phase liquide H_{TL} qui apparaît dans (D). Son obtention est basée sur la recherche d'une solution approchée du profil de température dans la goutte (Figure L).

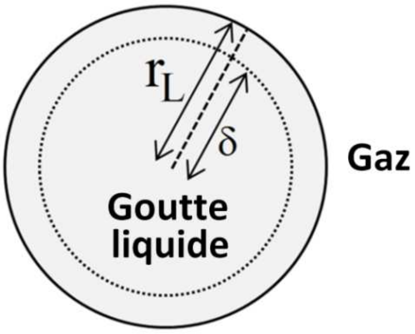

Figure L : Représentation schématique d'une goutte liquide divisée en 2 zones, une couche limite d'épaisseur $r_L - \delta$ et une zone de cœur de rayon δ. Dans la couche limite, la température varie fortement tandis qu'elle est supposée uniforme dans le cœur.

Finalement, un algorithme permet la résolution du système local d'échange de chaleur et de masse (C)+(D)+(E) en s'assurant de respecter les différentes contraintes mathématiques et physiques qui nous sont imposées. Nous sommes ainsi en possession des variables $\dot{m}_g, T_I$ et $Y_{g,wat,I}$ qui sont injectées dans le système diphasique d'EDPs moyennées en volume.

Divers cas-tests ont été effectués, la partie hyperbolique du modèle d'écoulement diphasique moyennées en volume ayant été résolue à l'aide de la méthode présentée dans le chapitre 1. En particulier, un test 0D d'évaporation simple permet de vérifier la relaxation des variables de l'écoulement vers leur propre valeur d'équilibre. De plus, les capacités du modèle à traiter la propagation d'ondes de chocs et de détente ont été confirmées et dévoilent des résultats intéressants. Enfin, le cas d'une charge explosive cylindrique placée à l'air libre (Figure B) a été étudié suite à l'intégration du modèle de transition de phase dans le code 3D non-structuré. Cela nous a permis de mesurer l'impact de ce modèle sur les résultats numériques obtenus et de nous rendre compte de la robustesse de l'algorithme permettant de le résoudre.

Chapitre 1

Un solveur de Riemann de type HLLC dans le cadre d'écoulements diphasiques compressibles en déséquilibre total

1.1. Introduction

This paper deals with the building of an approximate HLLC-type Riemann solver for hyperbolic two-phase non-equilibrium flows. It exists a wide range of physical and industrial applications where phase compressibility is mandatory (detonations, phase change, explosions,...) in conjunction with velocity disequilibrium. In this frame Baer and Nunziato (1986) type models are hyperbolic, this property being important with respect to the causality principle. To be more precise, the present work considers the Saurel et al. (2003) symmetric variant of Baer and Nunziato (BN) model. It involves 7 wave speeds instead of 6, this detail having importance as will be examined further.

BN-type models correspond to hyperbolic systems of partial differential equations (PDEs) with 7 equations, each phase having its own set of mass, momentum and energy balance equations. The seventh equation expresses the volume fraction transport, with the transport velocity u_I and involves a pressure relaxation term. Each phase evolves with its own density, velocity and pressure, in its own sub-volume.

This type of hyperbolic system involves many fundamental difficulties for the derivation of numerical methods. First, many non-linear waves are present (6 or 7) rendering complex the Riemann problem solution determination. Second, non-conservative terms are present as well as stiff relaxation terms. They both render difficult the determination of jump relations across waves.

The first Godunov type scheme developed for these equations is due to Saurel and Abgrall (1999) where the Riemann problem solution is approximated in the two-wave HLL context. Non-conservative terms are solved consistently with the fluxes approximation. This method is simple and robust, but too dissipative and unable to handle steady contact discontinuities.

The BN system Riemann problem has been studied by Andrianov and Warnecke (2004) in an 'inverse' context as the solution is anticipated and initial data rebuilt. A 3-wave HLLC-type solver was proposed by Li et al. (2004), restricted however to flows in mechanical equilibrium, i.e. in the limit of stiff pressure and velocity relaxation (Lallemand and Saurel, 2000), resulting in the single velocity flow model of Kapila et al. (2001).

Schwendeman et al. (2006) have built a 6-wave exact-type Riemann solver for the BN model with the help of a regularization method for the interfacial wave. Indeed, in the BN model, such regularization is needed as the interface wave is degenerate. Deledicque and Papalexandris (2007) developed another exact-type Riemann solver without regularization and gave existence conditions for the solution. Dumbser et al. (2010) considered the central scheme (FORCE solver) of Toro and Billet (2000) with the regularisation method of Parés (2006) for non-conservative terms. The method was developed in the frame of very high order schemes in conjunction with 3D unstructured meshes, producing impressive results (Dumbser et al., 2010). The method was improved again in Dumbser and Toro (2011) with an upwind solver based on Osher and Solomon (1982) method with 5 intermediate states in the Riemann problem. The regularisation method of Parés (2006) was still used for non-conservative terms. Tokareva and Toro (2010) also developed a HLLC-type Riemann solver with 6 waves and 5 intermediate states.

Ambroso et al. (2012) considered a BN-type model with 7 waves instead of 6, resulting in an algorithm free of regularization method. Such extended BN-type model was proposed by Saurel et al. (2003) with 'interfacial' pressure and velocity estimates issued of the acoustic Riemann solver for the Euler equations. The present contribution follows the same lines regarding this specific point. Last, Liang et al. (2014) have reconsidered the 3-wave HLLC solver of Li et al. (2004), still in the context of mechanical equilibrium solutions, i.e. in conjunction with stiff mechanical relaxation solvers, in the frame of GPU computing.

Generally speaking, these methods are restricted to flows in mechanical equilibrium or to flows with velocity disequilibrium but with extra restrictions. These restrictions can be for example low volume fraction jumps. In the authors knowledge, there is no evidence that these solvers are robust enough for flows in severe conditions, such as in detonations and explosions in the presence of stiff volume fraction gradients such as those appearing at material interfaces, in conjunction with both high velocity drift and high pressure gradients.

Aware of these limitations, another approach was developed by Abgrall and Saurel (2003). In the aforementioned methods, the Riemann problem is considered for given systems of PDEs, as done conventionally. A non-conventional method was derived by Abgrall and Saurel (2003) following the basic ideas of the Godunov method for the Euler equations. The first version of the Godunov method considers cell averaging of Riemann problem solutions. See Toro (1997) for details and Toro (1989) for second-order extension. In Abgrall and Saurel (2003) the two-phase computational cell is divided in two sub volumes, each one corresponding to a given phase. At each phase cell boundaries the Riemann problem for the Euler equations is solved. These solutions are then averaged in each sub volume and provide a set of discrete equations that correspond to some kind of two-phase Godunov method (Discrete Equations Method – DEM). In the continuous limit, when both space and time steps tend to zero, a BN-type model is recovered, as shown in Saurel et al. (2003). This model variant has 7 waves, is hyperbolic, symmetric in the sense that indexes of the phase can be reversed without changing the results, and is in agreement with the second law of thermodynamics.

The DEM method is also both accurate and robust. It has been successfully applied to material interfaces (Abgrall and Saurel, 2003), detonation waves in heterogeneous explosives (Chinnayya et al., 2004), cavitation around hypervelocity underwater bodies (Le Metayer et al., 2005), shocks in multiphase mixtures (Saurel et al., 2007) and two-phase nozzle flows (Berry et al., 2010). A variant of this method was derived by Chang and Liou (2007). Its ability to deal with phase transition fronts with the help of thermochemical relaxation solvers was demonstrated in Zein et al. (2010).

One of the reasons for this robustness is that non-conservative products are unambiguously solved by a physical wave diffraction problem. For instance, when a shock interacts with a volume fraction discontinuity, the product of Heaviside and Dirac functions appear. However, as soon as interaction occurs, the shock wave is diffracted in a weaker transmitted shock and reflected expansion wave (local Riemann problem of the Euler equations). As the pressure and velocity in the diffracted region are constants, the product with the Dirac function (volume fraction gradient) is unambiguous. This remark is at the core of the treatment of non-conservative terms with the DEM.

However, this method is not so easy to implement and is quite computational expensive. These two arguments are the motivation of the present work where a simplified method, easier to implement, faster and even more robust is developed.

From the DEM, we have learnt an important fact: The interfacial velocity is fairly approximated as a function only of the initial data at phase contacts separating two phases (contacts 1-2 or 2-1) as shown in Figure 1. In this figure, the interface velocity is determined as solution of the Riemann problem for the Euler equations, with initial data corresponding to two fluids separated by an interface, fluid 1 on the left and fluid 2 on the right. The same remark is valid for the interfacial pressure.

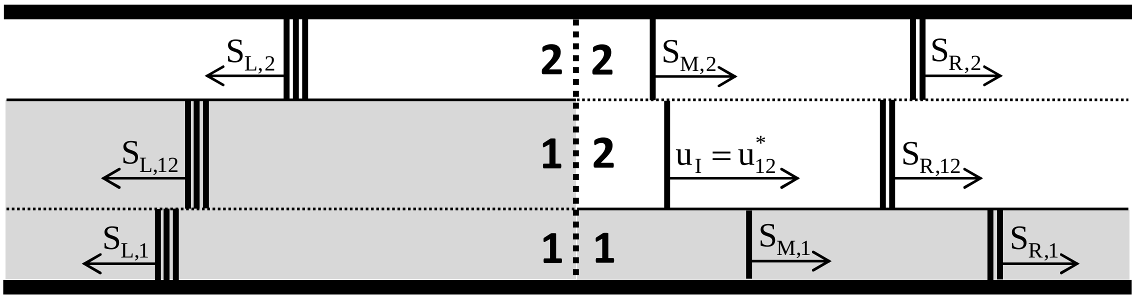

Figure 1: Stratified flow reference topology used in the DEM. Each flow channel (1-1, 1-2 and 2-2) sets in contact the phases, that involve initial discontinuities separating the left (L) and right (R) states. From these initial discontinuities, wave emerge and propagate in the various channels with their own speeds (S_L , S_R and S_M) as well as u_I , the local interfacial velocity. This cell boundary representation used in the DEM assumes 1D flow in each channel during the hyperbolic step. Multi-D effects are considered through relaxation terms.

A second major fact also appeared from the equations structure and DEM method. In this method, the channels 1-1, 1-2, 2-1 and 2-2 are considered frozen during wave propagation: Their height is constant during the hyperbolic step, meaning that corresponding volume fractions are locally frozen. In terms of continuous model, it means that relaxation effects are removed from the equations at each cell boundary, as done usually with Riemann solvers. Physically, it means that 2D effects in wave propagation and interface motion are locally omitted, as they are summarized in pressure relaxation effects.

Thanks to the two assumptions,

- local constancy of u_I and p_I,
- local freezing of volume fractions, or more precisely, volume fractions variations occurring only across u_I,

two major consequences result.

First, it is possible to express the two-phase model in local conservative form.

Second, each phase becomes decoupled from the other and has its own 4-wave Riemann solver.

These two properties render quite easy the development of HLLC-type Riemann solvers for the velocity and pressure non-equilibrium flow model. This solver is then analysed and is shown to be in agreement with the second law of thermodynamics. Several test problems are then addressed, showing method accuracy and robustness with respect to configurations having either exact solutions or experimental reference data.

The paper is organized as follows. The model under examination, with seven equations and seven waves is presented in Section 1.2. The issue of interfacial variables that are considered locally constant is addressed in Section 1.3 together with the local conservative formulation. The two-phase Riemann solver is built in Section 1.4. Its agreement with the second law of thermodynamics is addressed in Section 1.5. A simple Godunov type scheme is built in Section 1.6 and validation results are shown in Section 1.7.

1.2. Two-phase flow model and properties

The starting point of the analysis is a variant of the BN model derived from the DEM. Taking the continuous limit of these discrete equations (Saurel et al., 2003) the following set of PDEs has been obtained:

Phase1

$$\frac{\partial \alpha_1}{\partial t} + u_I \frac{\partial \alpha_1}{\partial x} = \mu(P_1 - P_2)$$

$$\frac{\partial \alpha_1 \rho_1}{\partial t} + \frac{\partial \alpha_1 \rho_1 u_1}{\partial x} = 0$$

$$\frac{\partial \alpha_1 \rho_1 u_1}{\partial t} + \frac{\partial \alpha_1 \rho_1 u_1^2 + \alpha_1 P_1}{\partial x} = P_I \frac{\partial \alpha_1}{\partial x} + \lambda(u_2 - u_1) \tag{1}$$

$$\frac{\partial \alpha_1 \rho_1 E_1}{\partial t} + \frac{\partial \alpha_1 (\rho_1 E_1 + P_1) u_1}{\partial x} = P_I u_I \frac{\partial \alpha_1}{\partial x} + \lambda \overline{u_I}(u_2 - u_1) - \mu \overline{P_I}(P_1 - P_2)$$

Phase2

$$\frac{\partial \alpha_2 \rho_2}{\partial t} + \frac{\partial \alpha_2 \rho_2 u_2}{\partial x} = 0$$

$$\frac{\partial \alpha_2 \rho_2 u_2}{\partial t} + \frac{\partial \alpha_2 \rho_2 u_2^2 + \alpha_2 P_2}{\partial x} = P_I \frac{\partial \alpha_2}{\partial x} - \lambda(u_2 - u_1)$$

$$\frac{\partial \alpha_2 \rho_2 E_2}{\partial t} + \frac{\partial \alpha_2 (\rho_2 E_2 + P_2) u_2}{\partial x} = P_I u_I \frac{\partial \alpha_2}{\partial x} - \lambda \overline{u_I}(u_2 - u_1) + \mu \overline{P_I}(P_1 - P_2)$$

This model considers each phase as compressible, evolving with its own velocity, temperature and pressure. Here, heat and mass transfers, as well as body forces have been omitted. The notations are conventional in the two-phase flow literature. The variable α_k represents the volume fraction of phase k, such that $\sum_k \alpha_k = 1$. ρ, u, P, e and E represent respectively the density, the velocity, the pressure, the internal energy and the total energy ($E = e + \frac{1}{2}u^2$).

The interfacial variables are symmetric with respect to the phase's indexes,

$$u_I = \frac{Z_1 u_1 + Z_2 u_2}{Z_1 + Z_2} + \operatorname{sgn}\left(\frac{\partial \alpha_1}{\partial x}\right) \frac{P_2 - P_1}{Z_1 + Z_2}, \tag{2}$$

$$P_I = \frac{Z_2 P_1 + Z_1 P_2}{Z_1 + Z_2} + \operatorname{sgn}\left(\frac{\partial \alpha_1}{\partial x}\right)\frac{Z_1 Z_2}{Z_1 + Z_2}\left(u_2 - u_1\right), \qquad (3)$$

where $Z_k = \rho_k c_k$ represents the acoustic impedance of phase k with c_k the associated sound speed.

These interfacial variables control the dynamics of droplet clouds, as they express velocity transport and forces acting at volume fraction gradients.

The volume average pressure and interface velocity are given by,

$$\overline{u_I} = \frac{Z_1 u_1 + Z_2 u_2}{Z_1 + Z_2}, \quad \overline{P_I} = \frac{Z_2 P_1 + Z_1 P_2}{Z_1 + Z_2}.$$

These variables express the transport velocity and pressure force inside the cloud of droplets.

The mechanical equilibrium state is reached at the end of relaxation processes controlled by the following rates,

$\mu = \dfrac{A_I}{Z_1 + Z_2}$, the pressure relaxation rate, where A_I represents the specific interfacial area,

$\lambda = \dfrac{1}{2}\mu Z_1 Z_2$, the velocity relaxation rate (or 'acoustic' drag) due to pressure forces.

Viscous effects can be added to this drag coefficient.

The thermodynamic closure of System (1) is achieved by convex equations of state $e_k = e_k\left(P_k, \rho_k\right)$.

The model fulfils the second law of thermodynamics, as the entropy equations read,

$$\frac{\partial \alpha_1 \rho_1 s_1}{\partial t} + \frac{\partial \alpha_1 \rho_1 u_1 s_1}{\partial x} =$$

$$\frac{1}{T_1}\left\{\frac{Z_1}{\left(Z_1 + Z_2\right)^2}\left((P_2 - P_1) + \operatorname{sgn}\left(\frac{\partial \alpha_1}{\partial x}\right) Z_2 (u_2 - u_1)\right)^2 \left|\frac{\partial \alpha_1}{\partial x}\right| + \lambda \frac{Z_2}{Z_1 + Z_2}(u_2 - u_1)^2 + \mu \frac{Z_1}{Z_1 + Z_2}(P_2 - P_1)^2\right\}$$

$$\frac{\partial \alpha_2 \rho_2 s_2}{\partial t} + \frac{\partial \alpha_2 \rho_2 u_2 s_2}{\partial x} =$$

$$\frac{1}{T_2}\left\{\frac{Z_2}{\left(Z_1 + Z_2\right)^2}\left((P_2 - P_1) + \operatorname{sgn}\left(\frac{\partial \alpha_1}{\partial x}\right) Z_2 (u_2 - u_1)\right)^2 \left|\frac{\partial \alpha_2}{\partial x}\right| + \lambda \frac{Z_1}{Z_1 + Z_2}(u_2 - u_1)^2 + \mu \frac{Z_2}{Z_1 + Z_2}(P_2 - P_1)^2\right\}$$

The right hand side of these two equations being positive or null, the mixture entropy production is necessarily positive too. Moreover, the system is hyperbolic with wave speeds u_I, $u_k \pm c_k$ and u_k for $k = 1,2$.

System (1) in the absence of source terms can be cast in compact form as:

$$\frac{\partial U_k}{\partial t} + \frac{\partial F_k}{\partial x} + \alpha_k \frac{\partial H_k}{\partial x} = 0, \ \forall k \in \{1,2\} \qquad (4)$$

with $U_k = \begin{pmatrix} \alpha_k \\ (\alpha\rho)_k \\ (\alpha\rho u)_k \\ (\alpha\rho E)_k \end{pmatrix}$; $F_k = \begin{pmatrix} \alpha_k u_I \\ (\alpha\rho u)_k \\ \alpha_k \left(\rho u^2 + P\right)_k - \alpha_k P_I \\ \alpha_k \left(\rho E + P\right)_k u_k - \alpha_k P_I u_I \end{pmatrix}$ and $H_k = \begin{pmatrix} -u_I \\ 0 \\ P_I \\ P_I u_I \end{pmatrix}$.

1.3. Local constants and local conservative formulation

It is now important to examine more closely the interfacial variables u_I and P_I that appear in the vectors F_k and H_k. To understand their meaning, the basic ideas of the DEM are re-examined.

1.3.1. DEM basis

This method consists in integrating Riemann problem solutions of the Euler equations on a given two-phase flow topology. The 1D Euler equations are expressed hereafter in condensed form as,

$$\frac{\partial w}{\partial t}+\frac{\partial f}{\partial x}=0,$$

with, $w=\left(\rho, \quad \rho u, \quad \rho E\right)^T$ and $f=\left(\rho u, \quad \rho u^2+P, \quad (\rho E+P)u\right)^T$.

The building of the discrete system with the DEM needs a two-phase topology as input, the simplest being the stratified flow one, as shown in Figure 1. Other topologies have been considered, such as annular flows in Saurel et al. (2003) and granular flows in Chinnayya et al. (2004). The discrete system has been shown as topology independent regarding the discrete form of (4). Only relaxation terms, that are not considered here, are topology dependent.

As shown in Figure 1, at each cell boundary four types of contact are possible between fluids $l\in\{1,2\}$ at left and fluids $m\in\{1,2\}$ at right: '1-1', '2-1', '2-2' and '1-2'. Each flow channel is solved independently of the others and has height h_{lm}, constant during the hyperbolic step. It means that volume fractions are locally frozen. It also means that wave dynamics and interface motion are assumed 1D, multi-D effects being considered in relaxation effects, omitted during the Riemann problem resolution.

The DEM uses Eulerian fluxes f_{lm}^* and Lagrangian ones $f_{lm}^{Lag,*}=\left(f-u_I w\right)_{lm}^*$. For each contact 'l-m' the Riemann problem of the Euler equation is solved to compute these fluxes. For example, considering the cell boundary $i-1/2$, the Eulerian flux for the l-m contact is computed as $f_{lm}^*=f_{lm}^*\left(w_{l,i-1}^n, w_{m,i}^n\right)$, where the superscript n denotes the time step. In the same way, the Lagrangian flux is obtained as $f_{lm}^{Lag*}=f_{lm}^{Lag*}\left(w_{l,i-1}^n, w_{m,i}^n\right)$.

The DEM discrete scheme for phase k then reads,

$$\frac{\left(U_k\right)_i^{n+1}-\left(U_k\right)_i^n}{\Delta t}+\frac{F_{i+1/2}^{Eul,k}-F_{i-1/2}^{Eul,k}}{\Delta x}=\frac{F_{i+1/2}^{Lag,k}+F_{i-1/2}^{Lag,k}}{\Delta x},$$

where Δx represents the space step, Δt the time step and the two-phase fluxes, for phase 1 (symmetric formulas being obtained for the second phase) are given by,

$$F_{i-1/2}^{Eul,1}=h_{11}f_{11}^*\left(w_{1,i-1}^n, w_{1,i}^n\right)+\frac{u_{12}^{*,+}}{\left|u_{12}^*\right|}h_{12}f_{12}^*\left(w_{1,i-1}^n, w_{2,i}^n\right)-\frac{u_{21}^{*,-}}{\left|u_{21}^*\right|}h_{21}f_{21}^*\left(w_{2,i-1}^n, w_{1,i}^n\right),$$

$$F_{i-1/2}^{Lag,1}=-\frac{u_{12}^{*,+}}{\left|u_{12}^*\right|}h_{12}f_{12}^{Lag*}\left(w_{1,i-1}^n, w_{2,i}^n\right)+\frac{u_{21}^{*,+}}{\left|u_{21}^*\right|}h_{21}f_{21}^{Lag,*}\left(w_{2,i-1}^n, w_{1,i}^n\right).$$

In these two formulas, it is clear that two-phase fluxes F are obtained as a sum of Euler equations fluxes f. For the sake of clarity, we have used the following functions,

$$\omega^+=\mathrm{Max}\left(0,\omega\right)=\frac{\omega+|\omega|}{2},\ \omega^-=\mathrm{Min}\left(0,\omega\right)=\frac{\omega-|\omega|}{2}.$$

1.3.2. Determination of the interfacial variables u_I and P_I

The determination of the interfacial variables u_I and P_I is based on the 2D topology with decoupled flow channels, as shown in Figure 1. The interfacial variables determination depends on the type of contact between the two phases: contact 1-2 or contact 2-1. It is determined by the sign of $(\alpha_{1L}-\alpha_{1R})$, as shown in Figure 2.

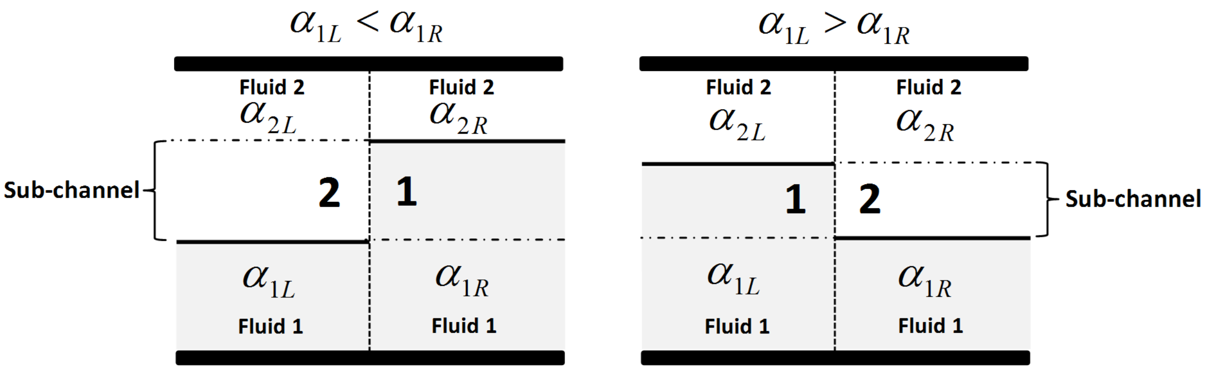

Figure 2: Schematic representation of the two types of contact that may appear at a given cell boundary.

The lower scripts L and R are relative respectively to the left and right states. For each contact the Riemann problem of the Euler equations with different fluids has to be solved. As the Riemann problem solution depends only of initial states L and R, variables u_I and P_I are locally constant during a time step at a given cell boundary. They are computed by an appropriate Riemann solver (exact or approximate) with correct initial states as inputs. The example of the HLLC Riemann solver for the Euler equations is used hereafter.

– **Contact 2-1**

The corresponding (x,t) diagram in the HLLC solver frame is shown in Figure 3.

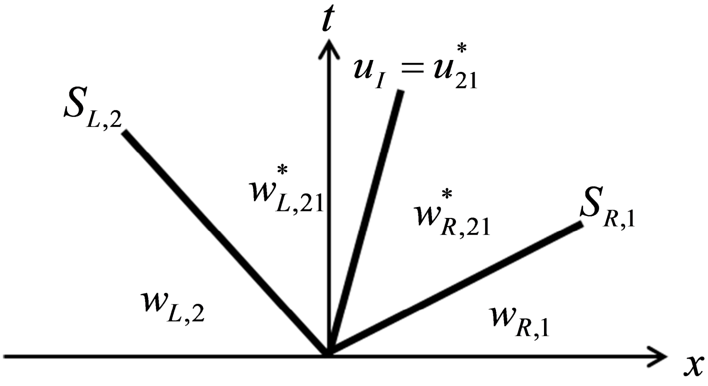

Figure 3: Wave pattern in the frame of the HLLC Riemann solver for contact 2-1. ‘w’ represents the set of variables of the Euler equations.

Contact 2-1 appears when $\alpha_{1L} < \alpha_{1R}$. The wave speeds $S_{L,2}$ and $S_{R,1}$ are estimated as:

$$S_{R,1} = \mathrm{Max}(u_{L,1} + c_{L,1}, u_{R,1} + c_{R,1}),$$

$$S_{L,2} = \mathrm{Min}(u_{L,2} - c_{L,2}, u_{R,2} - c_{R,2}).$$

The interfacial velocity and pressure are determined respectively under HLL and HLLC approximations as,

$$u_I = u_{21}^{*,HLL} = \frac{\left(\rho u^2 + P\right)_{R,1} - \left(\rho u^2 + P\right)_{L,2} + S_{L,2}(\rho u)_{L,2} - S_{R,1}(\rho u)_{R,1}}{(\rho u)_{R,1} - (\rho u)_{L,2} + S_{L,2}\rho_{L,2} - S_{R,1}\rho_{R,1}},$$

$$P_I = P_{R,21}^{*} = \rho_{R,1}\left(u_{R,1} - S_{R,1}\right)\left(u_{R,1} - u_I\right) + P_{R,1}.$$

– **Contact 1-2**

This contact corresponds to the symmetric situation when $\alpha_{1L} > \alpha_{1R}$. The corresponding wave pattern is shown in Figure 4.

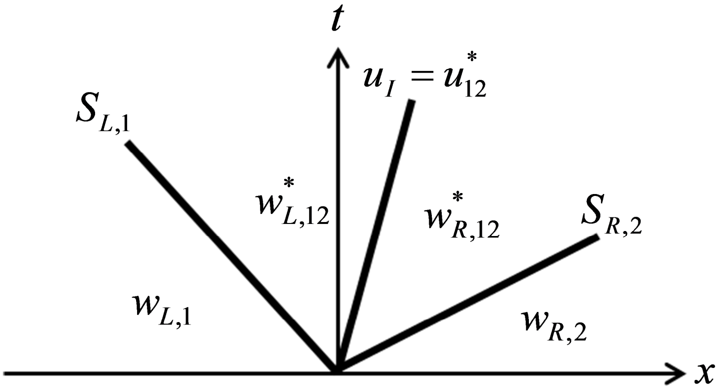

Figure 4: Wave pattern in the frame of the HLLC Riemann solver for contact 1-2.

The wave's speeds are now estimated as,

$$S_{R,2} = \mathrm{Max}\left(u_{L,2} + c_{L,2}, u_{R,2} + c_{R,2}\right),$$

$$S_{L,1} = \mathrm{Min}\left(u_{L,1} - c_{L,1}, u_{R,1} - c_{R,1}\right).$$

The interfacial variables are computed as,

$$u_I = u_{12}^{*,HLL} = \frac{\left(\rho u^2 + P\right)_{R,2} - \left(\rho u^2 + P\right)_{L,1} + S_{L,1}(\rho u)_{L,1} - S_{R,2}(\rho u)_{R,2}}{(\rho u)_{R,2} - (\rho u)_{L,1} + S_{L,1}\rho_{L,1} - S_{R,2}\rho_{R,2}},$$

$$P_I = P_{R,12}^{*} = \rho_{R,2}\left(u_{R,2} - S_{R,2}\right)\left(u_{R,2} - u_I\right) + P_{R,2}.$$

Let us mention that the interfacial variables (2) and (3) that appear in the continuous system (1) result of similar computations, in the limit of weak amplitude waves.

In the former expressions of u_I and P_I, it is clear that these variables are constant at a given cell boundary and during a given time step. As these variables are local constants, System (4) expresses locally in conservative form:

$$\frac{\partial U_k}{\partial t} + \frac{\partial F_k}{\partial x} = 0, \ \forall k \in \{1,2\} \tag{5}$$

with $U_k = \begin{pmatrix} \alpha_k \\ (\alpha\rho)_k \\ (\alpha\rho u)_k \\ (\alpha\rho E)_k \end{pmatrix}$ and $F_k = \begin{pmatrix} \alpha_k u_I \\ (\alpha\rho u)_k \\ \alpha_k\left(\rho u^2 + P\right)_k - \alpha_k P_I \\ \alpha_k(\rho E + P)_k u_k - \alpha_k P_I u_I \end{pmatrix}$.

This remark simplifies significantly the two-phase Riemann problem resolution.

1.4. Two-phase Riemann solver

The two-phase flow model under consideration (1) is hyperbolic with 7 waves. For a given cell boundary, a HLLC type Riemann solver with 6 intermediate states is quite complex to manage. These difficulties increase with increasing number of fluids (3 and more).

The variables u_I and P_I being local constants, another important simplification appears. The Riemann problem for a given phase is decoupled to the one of the other phase. Thus, for a given phase k, the Riemann problem is based on the PDEs system (5) and on its own wave pattern as shown in Figure 5.

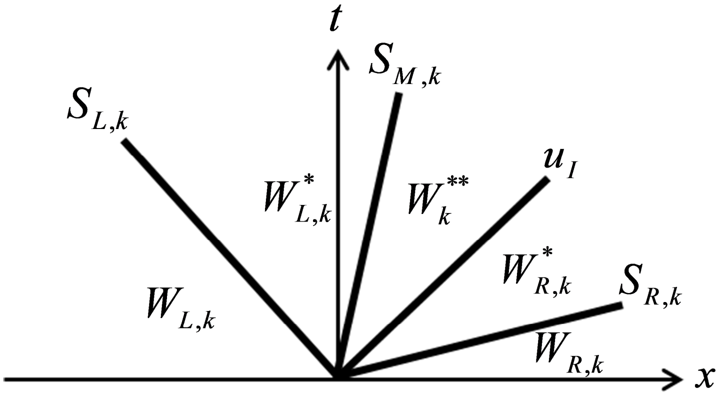

Figure 5: Schematic representation of the Riemann problem for a given phase k in the HLLC frame. 'W' represents the set of variables of the two-phase model.

In Figure 5, W_k denotes the vector of primitive variables of a given phase: $W_k = (\alpha_k, \ \rho_k, \ u_k, \ P_k)^T$.

$W_{L,k}$ and $W_{R,k}$ are respectively the left and right initial states, known at each time step. The Rankine-Hugoniot relations across the various waves link the initial data to the intermediate states $W^*_{L,k}$, W^{**}_k and $W^*_{R,k}$.

1.4.1. Wave speed estimates $S_{L,k}$, $S_{R,k}$ and $S_{M,k}$

The left- and right-facing wave speeds $S_{L,k}$ and $S_{R,k}$ are determined by the Davis (1988) estimates,

$$S_{R,k} = \mathrm{Max}\left(u_{L,k} + c_{L,k}, u_{R,k} + c_{R,k}\right),$$

$$S_{L,k} = \mathrm{Min}\left(u_{L,k} - c_{L,k}, u_{R,k} - c_{R,k}\right).$$

Let us mention that other wave speed estimates are possible. Denoting S_k^+ a positive wave speed for phase k, under Rusanov approximation it is possible to define $S_{R,k} = S_k^+$ and $S_{L,k} = -S_k^+$.

To estimate S_k^+, Davis (1988) considered the following guess:

$$S_k^+ = \mathrm{Max}\left(\left|u_{L,k} - c_{L,k}\right|, \left|u_{R,k} - c_{R,k}\right|, \left|u_{L,k} + c_{L,k}\right|, \left|u_{R,k} + c_{R,k}\right|\right).$$

Toro (2009) recommanded the following one:

$$S_k^+ = \mathrm{Max}\left(\left|u_{L,k}\right| + c_{L,k}, \left|u_{R,k}\right| + c_{R,k}\right).$$

WIth these wave speeds the intermediate contact wave is estimated under HLL (Harten et al., 1983) approximation as,

$$S_{M,k} = \frac{\alpha_{R,k}\left(\rho u^2 + P\right)_{R,k} - \alpha_{L,k}\left(\rho u^2 + P\right)_{L,k} + S_{L,k}(\alpha\rho u)_{L,k} - S_{R,k}(\alpha\rho u)_{R,k} + \left(\alpha_{L,k} - \alpha_{R,k}\right)P_I}{(\alpha\rho u)_{R,k} - (\alpha\rho u)_{L,k} + S_{L,k}(\alpha\rho)_{L,k} - S_{R,k}(\alpha\rho)_{R,k}}$$

where u_I and P_I are already computed.

1.4.2. Determination of the intermediate states

In the following, two configurations are considered, as shown in Figure 6:

a) $\boxed{S_{L,k} < S_{M,k} < u_I < S_{R,k}}$ **b)** $\boxed{S_{L,k} < u_I < S_{M,k} < S_{R,k}}$

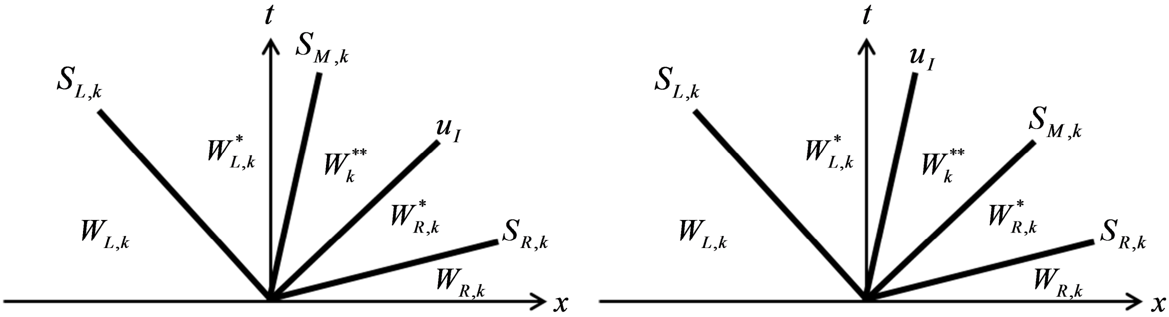

Figure 6: The two main wave configurations considered for the two-phase Riemann problem resolution.

The extreme situations $u_I > S_{R,k}$ and $u_I < S_{L,k}$ will be addressed latter.

In this section, the configuration **a)** only is considered: $S_{L,k} < S_{M,k} < u_I < S_{R,k}$. Configuration **b)** is addressed in Appendix 1.A.

Across each wave, the Rankine-Hugoniot (R) relations of System (5) read,

$$\begin{aligned}
&F^*_{L,k} = F_{L,k} + S_{L,k}\left(U^*_{L,k} - U_{L,k}\right),\\
&F^*_{R,k} = F_{R,k} + S_{R,k}\left(U^*_{R,k} - U_{R,k}\right),\\
&F^{**}_k = F^*_{R,k} + u_I\left(U^{**}_k - U^*_{R,k}\right),\\
&F^*_{L,k} = F^{**}_k + S_{M,k}\left(U^*_{L,k} - U^{**}_k\right).
\end{aligned} \tag{6}$$

To compute the flux in each intermediate state, the conservative variable vectors $U^*_{L,k}$, $U^*_{R,k}$ and U^{**}_k are needed.

Across the contact wave the RH relations reduce to:

$$u^*_{L,k} = u^{**}_k = S_{M,k} \tag{7}$$

$$P^*_{L,k} = P^{**}_k \tag{8}$$

As the interface velocity u_I is a local constant at a given cell boundary the volume fraction equation expresses in local conservation form. It has the following jumps,

$$\alpha^*_{L,k} = \alpha^{**}_k = \alpha_{L,k},$$

$$\alpha^*_{R,k} = \alpha_{R,k},$$

that are in perfect agreement with the non-conservative formulation of the volume fraction equation.

– **State** $W^*_{L,k}$

This state is readily obtained from the wave speed estimates and knowledge of the left state:

$$
\begin{aligned}
&\alpha^*_{L,k} = \alpha_{L,k}\,,\\
&\rho^*_{L,k} = \rho_{L,k}\frac{u_{L,k} - S_{L,k}}{S_{M,k} - S_{L,k}}\,,\\
&u^*_{L,k} = S_{M,k}\,,\\
&P^*_{L,k} = P_{L,k} + \rho_{L,k}\left(u_{L,k} - S_{L,k}\right)\left(u_{L,k} - S_{M,k}\right),\\
&E^*_{L,k} = E_{L,k} + \frac{(Pu)_{L,k} - P^*_{L,k}S_{M,k}}{\rho_{L,k}\left(u_{L,k} - S_{L,k}\right)}\,.
\end{aligned}
\tag{9}
$$

– **State** $W^*_{R,k}$

The main difficulty relies in the determination of $u^*_{R,k}$. To do this mass and momentum jump relations (6) across $S_{R,k}$, u_I, $S_{M,k}$ and $S_{L,k}$ are considered. Let us start with jump relations across $S_{R,k}$ and u_I :

$$\alpha_{L,k}\rho^{**}_k\left(u^{**}_k - u_I\right) = \alpha_{R,k}\rho^*_{R,k}\left(u^*_{R,k} - u_I\right) \tag{10}$$

$$\alpha_{L,k}\rho^{**}_k u^{**}_k\left(u^{**}_k - u_I\right) + \alpha_{L,k}P^{**}_k = \alpha_{R,k}\rho^*_{R,k}u^*_{R,k}\left(u^*_{R,k} - u_I\right) + \alpha_{R,k}P^*_{R,k} + \left(\alpha_{L,k} - \alpha_{R,k}\right)P_I \tag{11}$$

$$\rho^*_{R,k}\left(u^*_{R,k} - S_{R,k}\right) = \rho_{R,k}\left(u_{R,k} - S_{R,k}\right) \tag{12}$$

$$\rho^*_{R,k}u^*_{R,k}\left(u^*_{R,k} - S_{R,k}\right) + P^*_{R,k} = \rho_{R,k}u_{R,k}\left(u_{R,k} - S_{R,k}\right) + P_{R,k} \tag{13}$$

Combining (12) with (13) provides an expression for $P^*_{R,k}$:

$$P^*_{R,k} = \rho_{R,k}\left(u_{R,k} - S_{R,k}\right)\left(u_{R,k} - u^*_{R,k}\right) + P_{R,k}$$

Inserting (10) in (11) and using ((7) and (8) imply:

$$\alpha_{R,k}\rho^*_{R,k}\left(u^*_{R,k} - u_I\right)\left(S_{M,k} - u^*_{R,k}\right) = \alpha_{R,k}P^*_{R,k} - \alpha_{L,k}P^*_{L,k} + \left(\alpha_{L,k} - \alpha_{R,k}\right)P_I$$

Inserting the expression for $P^*_{R,k}$ in this equation yields,

$$\alpha_{R,k}\rho_{R,k}\left(u_{R,k} - S_{R,k}\right)\left(\frac{\left(u^*_{R,k} - u_I\right)\left(S_{M,k} - u^*_{R,k}\right)}{\left(u^*_{R,k} - S_{R,k}\right)} - \left(u_{R,k} - u^*_{R,k}\right)\right) = \alpha_{R,k}P_{R,k} - \alpha_{L,k}P^*_{L,k} + \left(\alpha_{L,k} - \alpha_{R,k}\right)P_I\,.$$

After rearrangement, the expression for $u^*_{R,k}$ is obtained:

$$u^*_{R,k} = \frac{\left((\alpha P)_{R,k} - (\alpha P)^*_{L,k} + \left(\alpha_{L,k} - \alpha_{R,k}\right)P_I\right)S_{R,k} - (\alpha\rho)_{R,k}\left(u_{R,k} - S_{R,k}\right)\left(u_I S_{M,k} - S_{R,k}u_{R,k}\right)}{(\alpha\rho)_{R,k}\left(u_{R,k} - S_{R,k}\right)\left(S_{R,k} - u_I - S_{M,k} + u_{R,k}\right) + (\alpha P)_{R,k} - (\alpha P)^*_{L,k} + \left(\alpha_{L,k} - \alpha_{R,k}\right)P_I}$$

This expression can be significantly simplified by inserting $P^*_{L,k}$ given by Equation (9). After tedious calculations the following result is obtained:

$$u^*_{R,k} = S_{M,k}$$

Consequently, all intermediate material velocities are equal:

$$u^*_{L,k} = u^{**}_k = u^*_{R,k} = S_{M,k} \tag{14}$$

This unexpected result will be shown to be in agreement with the second law of thermodynamics.

Relation (14) is a consequence of the weak form of System (5) (HLL-type approximation) that provides the intermediate flow speed, that already accounts for the interactions with the other phase through the non-conservative terms.

The $W^*_{R,k}$ state is then readily obtained,

$\alpha^*_{R,k} = \alpha_{R,k}$,

$\rho^*_{R,k} = \rho_{R,k} \dfrac{u_{R,k} - S_{R,k}}{S_{M,k} - S_{R,k}}$,

$u^*_{R,k} = S_{M,k}$,

$P^*_{R,k} = P_{R,k} + \rho_{R,k}(u_{R,k} - S_{R,k})(u_{R,k} - S_{M,k})$,

$E^*_{R,k} = E_{R,k} + \dfrac{(Pu)_{R,k} - P^*_{R,k} S_{M,k}}{\rho_{R,k}(u_{R,k} - S_{R,k})}$.

– **State** W^{**}_k

The invariance of the material velocity in the various intermediate states implies continuity of the variable $(\alpha\rho)_k$ across wave u_I :

$(\alpha\rho)^{**}_k = (\alpha\rho)^*_{R,k}$.

Moreover, the pressure in state W^{**}_k is given by,

$$P^{**}_k = P^*_{L,k} \ . \tag{15}$$

It can also be expressed by the momentum jump relation across wave u_I ,

$$P^{**}_k = \frac{\alpha_{R,k}}{\alpha_{L,k}} P^*_{R,k} + \frac{\alpha_{L,k} - \alpha_{R,k}}{\alpha_{L,k}} P_I \ . \tag{16}$$

This last expression is used hereafter to express the total energy,

$$E^{**}_k = E^*_{R,k} - \frac{\alpha_{L,k} - \alpha_{R,k}}{(\alpha\rho)^*_{R,k}} P_I \ . \tag{17}$$

1.4.3. Summary

We now have in hands the three intermediate states conservative variable vectors,

$$U^*_{L,k} = \begin{pmatrix} \alpha_{L,k} \\ (\alpha\rho)^*_{L,k} \\ (\alpha\rho)^*_{L,k} S_{M,k} \\ (\alpha\rho)^*_{L,k} E^*_{L,k} \end{pmatrix}, \ U^*_{R,k} = \begin{pmatrix} \alpha_{R,k} \\ (\alpha\rho)^*_{R,k} \\ (\alpha\rho)^*_{R,k} S_{M,k} \\ (\alpha\rho)^*_{R,k} E^*_{R,k} \end{pmatrix} \text{ and } U^{**}_k = \begin{pmatrix} \alpha_{L,k} \\ (\alpha\rho)^{**}_k \\ (\alpha\rho)^{**}_k S_{M,k} \\ (\alpha\rho)^{**}_k E^{**}_k \end{pmatrix},$$

with,

$$S_{M,k} = \frac{\alpha_{R,k}(\rho u^2 + P)_{R,k} - \alpha_{L,k}(\rho u^2 + P)_{L,k} + S_{L,k}(\alpha\rho u)_{L,k} - S_{R,k}(\alpha\rho u)_{R,k} + (\alpha_{L,k} - \alpha_{R,k})P_I}{(\alpha\rho u)_{R,k} - (\alpha\rho u)_{L,k} + S_{L,k}(\alpha\rho)_{L,k} - S_{R,k}(\alpha\rho)_{R,k}} .$$

– **State** $W^*_{L,k}$

$\alpha^*_{L,k} = \alpha_{L,k}$; $\rho^*_{L,k} = \rho_{L,k} \dfrac{u_{L,k} - S_{L,k}}{S_{M,k} - S_{L,k}}$; $u^*_{L,k} = S_{M,k}$;

$P^*_{L,k} = P_{L,k} + \rho_{L,k}(u_{L,k} - S_{L,k})(u_{L,k} - S_{M,k})$; $E^*_{L,k} = E_{L,k} + \dfrac{(Pu)_{L,k} - P^*_{L,k} S_{M,k}}{\rho_{L,k}(u_{L,k} - S_{L,k})}$.

– **State** $W^*_{R,k}$

$\alpha^*_{R,k} = \alpha_{R,k}$; $\rho^*_{R,k} = \rho_{R,k} \dfrac{u_{R,k} - S_{R,k}}{S_{M,k} - S_{R,k}}$; $u^*_{R,k} = S_{M,k}$;

$$P_{R,k}^{*} = P_{R,k} + \rho_{R,k}\left(u_{R,k} - S_{R,k}\right)\left(u_{R,k} - S_{M,k}\right); \qquad E_{R,k}^{*} = E_{R,k} + \frac{(Pu)_{R,k} - P_{R,k}^{*} S_{M,k}}{\rho_{R,k}\left(u_{R,k} - S_{R,k}\right)} .$$

– **State** W_k^{**}

$$\alpha_k^{**} = \alpha_{L,k} \; ; \qquad (\alpha\rho)_k^{**} = (\alpha\rho)_{R,k}^{*} \; ; \qquad u_k^{**} = S_{M,k} \; ;$$

$$P_k^{**} = P_{L,k}^{*} \; ; \qquad E_k^{**} = E_{R,k}^{*} - \frac{\alpha_{L,k} - \alpha_{R,k}}{(\alpha\rho)_{R,k}^{*}} P_I .$$

The fluxes in the various intermediate states are deduced from (6).

1.4.4. Solution sampling

Let us recall that two wave patterns are possible,

– $S_{L,k} < S_{M,k} < u_I < S_{R,k}$,

– $S_{L,k} < u_I < S_{M,k} < S_{R,k}$.

In the cases of very high drift velocity among the phases, it is possible that u_I be outside the range $\left]S_{L,k}, S_{R,k}\right[$ of a given phase. To avoid this issue the following strategy has been adopted. If u_I exceeds 90% of the wave velocity $S_{R,k}$, then $S_{R,k}$ is reset to the maximum wave speed of all phases,

$S_{R,k} := \underset{k}{\mathrm{Max}}\left(S_{R,k}\right)$.

The same is done for the left facing wave speed,

$S_{L,k} := \underset{k}{\mathrm{Min}}\left(S_{L,k}\right)$.

With the help of the intermediate states and fluxes summarized in Section 1.4.3 the last step consists in the solution sampling,

– if $S_{M,k} < u_I$, then $F_k^{*} = \begin{cases} F_{L,k} & \text{if} \quad S_{L,k} \geq 0 \\ F_{L,k}^{*} & \text{if} \quad S_{L,k} < 0 \text{ and } S_{M,k} \geq 0 \\ F_k^{**} & \text{if} \quad S_{M,k} < 0 \text{ and } u_I > 0 \\ F_{R,k}^{*} & \text{if} \quad u_I \leq 0 \text{ and } S_{R,k} > 0 \\ F_{R,k} & \text{if} \quad S_{R,k} \leq 0 \end{cases}$,

– if $u_I < S_{M,k}$, then $F_k^{*} = \begin{cases} F_{L,k} & \text{if} \quad S_{L,k} \geq 0 \\ F_{L,k}^{*} & \text{if} \quad S_{L,k} < 0 \text{ and } u_I \geq 0 \\ F_k^{**} & \text{if} \quad u_I < 0 \text{ and } S_{M,k} > 0 \\ F_{R,k}^{*} & \text{if} \quad S_{M,k} \leq 0 \text{ and } S_{R,k} > 0 \\ F_{R,k} & \text{if} \quad S_{R,k} \leq 0 \end{cases}$.

We now check solver's agreement with the second law of thermodynamics.

1.5. Entropy preserving

Robustness of the solver is related to densities and volume fractions positivity as well as agreement with the second law of thermodynamics. These properties are matched by the HLLC solver for the Euler equations (Bouchut, 2004). We examine entropy production of the solver in the present two-phase context, for the wave configuration $S_{M,k} < u_I$ considered previously.

Waves speeds $S_{L,k}$ and $S_{R,k}$ are considered as single phase shocks in phase k. The single phase analysis and results of Bouchut (2004) are therefore still valid, showing agreement with the second law of thermodynamics across these waves. However, a fourth wave (u_I) appears in the two-phase context and it is necessary to show that the entropy production is positive across this wave, separating states $W^*_{R,k}$ and W^{**}_k. There is no evidence, as it has been shown previously that the material velocity is constant across this wave, a non intuitive fact.

Expanding the energy jump relation (17) the following result is obtained,

$$e^{**}_k + \frac{1}{2} u^{**2}_k = e^*_{R,k} + \frac{1}{2} {u^*_{R,k}}^2 - \frac{\alpha_{L,k} - \alpha_{R,k}}{(\alpha\rho)^*_{R,k}} P_I .$$

The invariance of the material velocity in these two states implies,

$$e^{**}_k = e^*_{R,k} - \frac{\alpha_{L,k} - \alpha_{R,k}}{(\alpha\rho)^*_{R,k}} P_I . \tag{18}$$

The Gibbs identity of a given phase reads,

$$de_k = T_k d\eta_k - P_k dv_k$$

with η_k and $v_k = \frac{1}{\rho_k}$ representing respectively the entropy and the specific volume of phase k.

The Gibbs relation expressed across wave u_I thus reads,

$$\overline{T}_k \left(\eta^{**}_k - \eta^*_{R,k}\right) = e^{**}_k - e^*_{R,k} + \overline{P}_k \left(v^{**}_k - v^*_{R,k}\right),$$

where $\overline{T}_k$ and $\overline{P}_k$ represent respectively temperature and pressure averages.

With the help of (18) and mass jump condition expressed as,

$$v^{**}_k = \frac{\alpha_{L,k}}{\alpha_{R,k}} v^*_{R,k},$$

the discrete Gibbs identity becomes,

$$\overline{T}_k \left(\eta^{**}_k - \eta^*_{R,k}\right) = \left(\overline{P}_k - P_I\right)\left(\frac{\alpha_{L,k}}{\alpha_{R,k}} - 1\right) v^*_{R,k} \quad . \tag{19}$$

As $\overline{T}_k$ is obviously positive, it is necessary to show that the right hand side of (19) is positive too.

For weak enough discontinuities it is reasonable to assume,

$$\overline{P}_k = \frac{1}{2}\left(P^{**}_k + P^*_{R,k}\right). \tag{20}$$

Inserting (20) and (16) in (19) the entropy jump now reads,

$$\overline{T}_k \left(\eta^{**}_k - \eta^*_{R,k}\right) = \frac{1}{2}\left(P^*_{R,k} - P_I\right)\left(\frac{\alpha_{L,k}}{\alpha_{R,k}} - \frac{\alpha_{R,k}}{\alpha_{L,k}}\right) v^*_{R,k} .$$

Let us now specify the calculations to phase 1:

$$T_1\left(\eta^{**}_1 - \eta^*_{R,1}\right) = \frac{1}{2}\left(P^*_{R,1} - P_I\right)\left(\frac{\alpha_{L,1}}{\alpha_{R,1}} - \frac{\alpha_{R,1}}{\alpha_{L,1}}\right) v^*_{R,1} .$$

Two instances have to be considered.

– Configuration $\alpha_{L,1} < \alpha_{R,1}$

In this situation, necessarily,

$$\left(\frac{\alpha_{L,1}}{\alpha_{R,1}}-\frac{\alpha_{R,1}}{\alpha_{L,1}}\right)<0\cdot$$

Moreover, when $\alpha_{L,1}<\alpha_{R,1}$, the interface corresponds to a contact 2-1 and the expression for P_I, as given in Section 1.3.2 reads,

$$P_I=P^*_{R,21}=\rho_{R,1}(u_{R,1}-S_{R,1})(u_{R,1}-u_I)+P_{R,1}.$$

Therefore,

$$P^*_{R,1}-P_I=\rho_{R,1}(u_{R,1}-S_{R,1})(u_I-S_{M,1}).$$

This term is negative as $u_{R,1}-S_{R,1}<0$ and $u_I-S_{M,1}>0$. The entropy production is consequently positive.

– Configuration $\alpha_{L,1}>\alpha_{R,1}$

It implies,

$$\left(\frac{\alpha_{L,1}}{\alpha_{R,1}}-\frac{\alpha_{R,1}}{\alpha_{L,1}}\right)>0\cdot$$

This situation ($\alpha_{L,1}>\alpha_{R,1}$) corresponds to a contact 1-2 with $P_I=P^*_{L,12}=P^*_{R,12}$ given by:

$$P_I=P^*_{L,12}=\rho_{L,1}(u_{L,1}-S_{L,1})(u_{L,1}-u_I)+P_{L,1}$$

With the help of Relations (9), (15) and (16) it is possible to express $P^*_{R,1}$ as a function of $P_{L,1}$ and P_I,

$$P^*_{R,1}=\frac{\alpha_{L,1}}{\alpha_{R,1}}\left(P_{L,1}+\rho_{L,1}(u_{L,1}-S_{L,1})(u_{L,1}-S_{M,1})\right)-\left(\frac{\alpha_{L,1}}{\alpha_{R,1}}-1\right)P_I\cdot$$

Consequently,

$$P^*_{R,1}-P_I=\frac{\alpha_{L,1}}{\alpha_{R,1}}\rho_{L,1}(u_{L,1}-S_{L,1})(u_I-S_{M,1}).$$

This term is positive as $u_{L,1}-S_{L,1}>0$ and $u_I-S_{M,1}>0$. The entropy production across wave u_I is therefore positive. There is no difficulty to make the same proof for phase 2.

Computational experiments of Section 1.7. illustrate the entropy preserving character of the present solver.

1.6. Godunov type scheme

Having the HLLC two-phase Riemann solver in hands, it is now possible to derive a Godunov type scheme. For the sake of simplicity, the first-order version only is presented, its higher order variant being given in Appendix 1.B.

As the entire cell is now considered, it is not possible to consider local conservative formulation. The system is thus considered under the form (4),

$$\frac{\partial U_k}{\partial t}+\frac{\partial F_k}{\partial x}+\alpha_k\frac{\partial H_k}{\partial x}=0,\ \forall k\in\{1,2\}, \tag{21}$$

with $U_k=\begin{pmatrix}\alpha_k\\(\alpha\rho)_k\\(\alpha\rho u)_k\\(\alpha\rho E)_k\end{pmatrix}$, $F_k=\begin{pmatrix}\alpha_k u_I\\(\alpha\rho u)_k\\\alpha_k(\rho u^2+P)_k-\alpha_k P_I\\\alpha_k(\rho E+P)_k u_k-\alpha_k P_I u_I\end{pmatrix}$ and $H_k=\begin{pmatrix}-u_I\\0\\P_I\\P_I u_I\end{pmatrix}$.

For a given cell i, the Godunov scheme we consider reads,

$$U_{k,i}^{n+1} = U_{k,i}^{n} - \frac{\Delta t}{\Delta x}\left[F_{k,i+\frac{1}{2}}^{*} - F_{k,i-\frac{1}{2}}^{*} + \alpha_{k,i}^{n}\left(H_{k,i+\frac{1}{2}}^{*} - H_{k,i-\frac{1}{2}}^{*}\right)\right],\ \forall k \in \{1,2\},$$

with $H_{k,i\pm\frac{1}{2}}^{*} = \left(-\left(u_{I}\right)_{k,i\pm\frac{1}{2}},\quad 0,\quad \left(P_{I}\right)_{k,i\pm\frac{1}{2}},\quad \left(P_{I}u_{I}\right)_{k,i\pm\frac{1}{2}}\right)^{T}$.

Δx and Δt represent respectively the space and time step. The superscripts n and $n+1$ denote two successive time steps t^{n} and t^{n+1}.

This method is stable under conventional CFL restriction:

$$\Delta t = \mathrm{CFL}\,\frac{\Delta x}{\mathrm{Max}\left(S_{L,k}, S_{R,k}\right)}.$$

In the above Godunov type scheme, the non-conservative terms have been approximated with the simplest method. Let us examine this approximation more deeply.

Non-conservative terms

Let us focus on the term $\alpha_{k}\dfrac{\partial H_{k}}{\partial x}$ and justify its discrete form as $\alpha_{k,i}^{n}\left(H_{k,i+\frac{1}{2}}^{*} - H_{k,i-\frac{1}{2}}^{*}\right)/\Delta x$ at least with respect to the DEM.

In the DEM framework the discrete form of the non-conservative term $H_{k}\dfrac{\partial \alpha_{k}}{\partial x}$ corresponds to $\dfrac{F_{i+1/2}^{Lag,k} + F_{i-1/2}^{Lag,k}}{\Delta x}$ appearing in the numerical scheme given in Section 1.3.1 and representing the Lagrangian fluxes contribution.

Assuming regular enough functions, we have,

$$H_{k}\frac{\partial \alpha_{k}}{\partial x} = \frac{\partial \alpha_{k} H_{k}}{\partial x} - \alpha_{k}\frac{\partial H_{k}}{\partial x}.$$

With the following discrete analog,

$$\frac{(\alpha H)_{k,i+\frac{1}{2}}^{*} - (\alpha H)_{k,i-\frac{1}{2}}^{*}}{\Delta x} - \alpha_{k,i}^{n}\frac{\left(H_{k,i+\frac{1}{2}}^{*} - H_{k,i-\frac{1}{2}}^{*}\right)}{\Delta x},$$

the formulation appearing in (21) is recovered.

To show agreement with the DEM it is necessary to show that,

$$(\alpha H)_{k,i+\frac{1}{2}}^{*} - (\alpha H)_{k,i-\frac{1}{2}}^{*} - \alpha_{k,i}^{n}\left(H_{k,i+\frac{1}{2}}^{*} - H_{k,i-\frac{1}{2}}^{*}\right) = F_{i+1/2}^{Lag,k} + F_{i-1/2}^{Lag,k}.$$

Let us now specify the calculations for phase 1.

On the one hand, we have:

$$\begin{aligned}
&(\alpha H)_{1,i+\frac{1}{2}}^{*} - (\alpha H)_{1,i-\frac{1}{2}}^{*} - \alpha_{1,i}^{n}\left(H_{1,i+\frac{1}{2}}^{*} - H_{1,i-\frac{1}{2}}^{*}\right)\\
&= \left(\alpha_{1,i+\frac{1}{2}}^{*} - \alpha_{1,i}^{n}\right)H_{1,i+\frac{1}{2}}^{*} + \left(\alpha_{1,i}^{n} - \alpha_{1,i-\frac{1}{2}}^{*}\right)H_{1,i-\frac{1}{2}}^{*} \qquad (22)\\
&= \left(\alpha_{1,i}^{n}\left(\frac{u_{I}^{+}}{|u_{I}|}\right)_{i+1/2} - \alpha_{1,i+1}^{n}\left(\frac{u_{I}^{-}}{|u_{I}|}\right)_{i+1/2} - \alpha_{1,i}^{n}\right)H_{1,i+\frac{1}{2}}^{*} + \left(\alpha_{1,i}^{n} - \alpha_{1,i-1}^{n}\left(\frac{u_{I}^{+}}{|u_{I}|}\right)_{i-1/2} + \alpha_{1,i}^{n}\left(\frac{u_{I}^{-}}{|u_{I}|}\right)_{i-1/2}\right)H_{1,i-\frac{1}{2}}^{*}
\end{aligned}$$

On the other hand we have,

$$F_{i+1/2}^{Lag,1} + F_{i-1/2}^{Lag,1} = \left(\frac{u_{12}^{*,-}}{\left| u_{12}^{*} \right|} h_{12} \right)_{i+1/2} f_{12}^{Lag*}\left(w_{1,i}^{n}, w_{2,i+1}^{n} \right) - \left(\frac{u_{21}^{*,-}}{\left| u_{21}^{*} \right|} h_{21} \right)_{i+1/2} f_{21}^{Lag,*}\left(w_{2,i}^{n}, w_{1,i+1}^{n} \right)$$

$$- \left(\frac{u_{12}^{*,+}}{\left| u_{12}^{*} \right|} h_{12} \right)_{i-1/2} f_{12}^{Lag*}\left(w_{1,i-1}^{n}, w_{2,i}^{n} \right) + \left(\frac{u_{21}^{*,+}}{\left| u_{21}^{*} \right|} h_{21} \right)_{i-1/2} f_{21}^{Lag,*}\left(w_{2,i-1}^{n}, w_{1,i}^{n} \right)$$

Inserting the heights h_{12} and h_{21} definitions,

$$F_{i+1/2}^{Lag,1} + F_{i-1/2}^{Lag,1} = \left(\frac{u_{12}^{*,-}}{\left| u_{12}^{*} \right|} \right)_{i+1/2} \mathrm{Max}\left(0, \alpha_{1,i}^{n} - \alpha_{1,i+1}^{n} \right) f_{12}^{Lag*}\left(w_{1,i}^{n}, w_{2,i+1}^{n} \right) - \left(\frac{u_{21}^{*,-}}{\left| u_{21}^{*} \right|} \right)_{i+1/2} \mathrm{Max}\left(0, \alpha_{1,i+1}^{n} - \alpha_{1,i}^{n} \right) f_{21}^{Lag,*}\left(w_{2,i}^{n}, w_{1,i+1}^{n} \right)$$

$$- \left(\frac{u_{12}^{*,+}}{\left| u_{12}^{*} \right|} \right)_{i-1/2} \mathrm{Max}\left(0, \alpha_{1,i-1}^{n} - \alpha_{1,i}^{n} \right) f_{12}^{Lag*}\left(w_{1,i-1}^{n}, w_{2,i}^{n} \right) + \left(\frac{u_{21}^{*,+}}{\left| u_{21}^{*} \right|} \right)_{i-1/2} \mathrm{Max}\left(0, \alpha_{1,i}^{n} - \alpha_{1,i-1}^{n} \right) f_{21}^{Lag,*}\left(w_{2,i-1}^{n}, w_{1,i}^{n} \right)$$

Let us consider the example of positive velocity flow at both cell boundaries. The latter expression reduces to,

$$F_{i+1/2}^{Lag,1} + F_{i-1/2}^{Lag,1} = \mathrm{Max}\left(0, \alpha_{1,i}^{n} - \alpha_{1,i-1}^{n} \right) f_{21}^{Lag,*}\left(w_{2,i-1}^{n}, w_{1,i}^{n} \right) - \mathrm{Max}\left(0, \alpha_{1,i-1}^{n} - \alpha_{1,i}^{n} \right) f_{12}^{Lag*}\left(w_{1,i-1}^{n}, w_{2,i}^{n} \right).$$

Let us now assume a monotonic decreasing volume fraction profile,

$$\alpha_{1,i-1}^{n} > \alpha_{1,i}^{n} > \alpha_{1,i+1}^{n}.$$

Therefore,

$$F_{i+1/2}^{Lag,1} + F_{i-1/2}^{Lag,1} = \left(\alpha_{1,i}^{n} - \alpha_{1,i-1}^{n} \right) f_{12}^{Lag*}\left(w_{1,i-1}^{n}, w_{2,i}^{n} \right).$$

Let us now consider (22). In the same flow conditions of positive velocity and decreasing volume fraction it reduces to,

$$(\alpha H)_{1,i+\frac{1}{2}}^{*} - (\alpha H)_{1,i-\frac{1}{2}}^{*} - \alpha_{1,i}^{n}\left(H_{1,i+\frac{1}{2}}^{*} - H_{1,i-\frac{1}{2}}^{*} \right) = \left(\alpha_{1,i}^{n} - \alpha_{1,i-1}^{n} \right) H_{1,i-\frac{1}{2}}^{*}.$$

In the present context, the only fluids contact to consider is contact 1-2. In this situation,

$$H_{1,i-\frac{1}{2}}^{*} = f_{12}^{Lag*}\left(w_{1,i-1}^{n}, w_{2,i}^{n} \right).$$

This example shows agreement between the discrete form $\alpha_{k,i}^{n}\left(H_{k,i+\frac{1}{2}}^{*} - H_{k,i-\frac{1}{2}}^{*} \right)$ and the DEM one.

The other flow configurations are examined in Appendix 1.D showing perfect agreement with the DEM in all instances.

Second-order extension

The first order Godunov method is extended to higher order with the MUSCL-Hancock strategy.

System (4) is recalled hereafter :

$$\frac{\partial U_k}{\partial t} + \frac{\partial F_k}{\partial x} + \alpha_k \frac{\partial H_k}{\partial x} = 0, \ \forall k \in \{1,2\},$$

with $U_k = \begin{pmatrix} \alpha_k \\ (\alpha\rho)_k \\ (\alpha\rho u)_k \\ (\alpha\rho E)_k \end{pmatrix}$, $F_k = \begin{pmatrix} \alpha_k u_I \\ (\alpha\rho u)_k \\ \alpha_k\left(\rho u^2 + P\right)_k - \alpha_k P_I \\ \alpha_k (\rho E + P)_k u_k - \alpha_k P_I u_I \end{pmatrix}$ and $H_k = \begin{pmatrix} -u_I \\ 0 \\ P_I \\ P_I u_I \end{pmatrix}$.

The set of primitive variables, Ψ_k reads $\Psi_k = (\alpha_k, \ \rho_k, \ u_k, \ P_k)^T$.

The MUSCL method proceeds with the following sequence.

– Riemann problem resolution for the locally conservative System (5)

The Riemann problem is solved with the extrapolated variables and the cell boundary flux is computed as $F^{*}_{k,i\pm\frac{1}{2}} = F^{*}_{k,i\pm\frac{1}{2}}\left(\Psi^{n}_{L},\Psi^{n}_{R}\right)$. Moreover, the computation of u^{n}_{I} and P^{n}_{I} provides the non-conservative flux $H^{*}_{k,i\pm\frac{1}{2}}$.

– Gradients computation

Let us denote by $\Delta^{-}_{k,i}$ and $\Delta^{+}_{k,i}$ the gradients computed on the left and right sides of computational cell i:

$\Delta^{-}_{k,i} = \dfrac{\Psi^{n}_{k,i} - \Psi^{n}_{k,i-1}}{\Delta x}$ and $\Delta^{+}_{k,i} = \dfrac{\Psi^{n}_{k,i+1} - \Psi^{n}_{k,i}}{\Delta x}$.

A slope limiter ξ is used to avoid local extrema. In the present work, MinMod and Van Leer limiters are used. After limitation, the slope is denoted by $\Delta_{k,i} = \xi\left(\Delta^{-}_{k,i},\Delta^{+}_{k,i}\right)$.

– Godunov type scheme during half time step

$$U^{n+1/2}_{k,i} = U^{n}_{k,i} - \frac{\Delta t^{n}}{2\Delta x}\left[F^{*}_{k,i+\frac{1}{2}} - F^{*}_{k,i-\frac{1}{2}} + \alpha^{n}_{k,i}\left(H^{*}_{k,i+\frac{1}{2}} - H^{*}_{k,i-\frac{1}{2}}\right)\right],\ \forall k \in \{1,2\}$$

– Variables extrapolation

For a given cell boundary $i+1/2$ at time $t^{n+1/2}$, left and right extrapolated states are given by :

$\Psi^{n+1/2}_{L,k} = \Psi^{n+1/2}_{k,i} + \dfrac{\Delta x}{2}\Delta_{k,i}$ and $\Psi^{n+1/2}_{R,k} = \Psi^{n+1/2}_{k,i+1} - \dfrac{\Delta x}{2}\Delta_{k,i+1}$.

– Riemann problem resolution for the locally conservative System (5)

The Riemann problem is solved with the extrapolated variables and the cell boundary flux is computed as $F^{**}_{k,i\pm\frac{1}{2}} = F^{*}_{k,i\pm\frac{1}{2}}\left(\Psi^{n+1/2}_{L},\Psi^{n+1/2}_{R}\right)$. Moreover, the computation of $u^{n+1/2}_{I}$ and $P^{n+1/2}_{I}$ provide the non-conservative flux $H^{**}_{k,i\pm\frac{1}{2}}$.

– Evolution step

$$U^{n+1}_{k,i} = U^{n}_{k,i} - \frac{\Delta t}{\Delta x}\left[F^{**}_{k,i+\frac{1}{2}} - F^{**}_{k,i-\frac{1}{2}} + \alpha^{n+1/2}_{k,i}\left(H^{**}_{k,i+\frac{1}{2}} - H^{**}_{k,i-\frac{1}{2}}\right)\right],\ \forall k \in \{1,2\}.$$

Relaxation solvers

Source and relaxation terms have been omitted from Section 1.3. with the quest of an appropriate hyperbolic solver. However, relaxation effects may be of paramount importance in multiphase mixtures. Stiff mechanical relaxation effects may also be used to solve interfacial flows, in order to fulfil interface conditions of equal pressures and equal normal velocities (Saurel and Abgrall, 1999). Corresponding stiff solvers are summarized in Appendix 1.B and 1.C.

1.7. Computational examples and validations

The method is validated on a series of test problems involving both velocity disequilibrium and stiff mechanical equilibrium, such as different two-phase shock tube test problems, a sedimentation test, and the Rogue et al. (1998) two-phase test. When available, exact solutions are used as well as experimental data. Comparison with the DEM is also addressed. Three-dimensional computations are also presented at the end of this section to illustrate method's capabilities.

In all tests that follow, the materials are assumed governed by the ‘stiffened-gas’ (SG) equation of state (EOS):

$P_k = (\gamma_k - 1)\rho_k e_k - \gamma_k P_{\infty,k}$, with $k \in \{g,l\}$ (23)

This EOS involves both molecular thermal agitation through the term $(\gamma_k - 1)\rho_k e_k$ and attractive short distance intermolecular effects through the term $-\gamma_k P_{\infty,k}$. These attractive effects are present only in condensed materials.

Parameters for the gas phase are $\gamma_g = 1.4$ and $P_{\infty,g} = 0\ \mathrm{Pa}$ while for the liquid phase they are $\gamma_l = 4.4$ and $P_{\infty,l} = 6\times10^8\,\mathrm{Pa}$. Obviously, other convex EOS can be used, see for example Chinnayya et al. (2004).

The entropy definition associated to (23) reads,

$$\eta_k = c_{v,k}\ln\left(\frac{P_k + P_{\infty,k}}{\rho_k^{\gamma_k}}\right) + q_k,$$

where $c_{v,k}$ represents the specific heat at constant volume of phase k and q_k the entropy of formation.

As both $c_{v,k}$ and q_k are constants, the evolution of $\left(P_k + P_{\infty,k}\right)/\rho_k^{\gamma_k}$ provides the qualitative behaviour of the entropies. This variable will be used to check the entropy preserving character of the method.

In the following, velocity non-equilibrium two-phase flows are addressed first. Method capabilities to deal with single velocity flows with the help of stiff relaxation solvers are addressed secondly.

All 1D tests shown hereafter are achieved with $\mathrm{CFL} = 0.8$.

1.7.1. Velocity disequilibrium two-phase flow tests

Two-phase shock tube without relaxation effects

The shock tube contains two-separated fluids with uniform volume fraction ($\alpha_g = 0.5$) everywhere. The left chamber has the same high pressure for both phases ($10^9\,\mathrm{Pa}$) while the right one has the same low pressure ($10^5\mathrm{Pa}$) for both phases. Gas and liquid densities are respectively set to $50\,\mathrm{kg/m^3}$ and $1000\,\mathrm{kg/m^3}$.

No source, no relaxation terms are used in this run, making the phases evolutions fully decoupled. Results are shown in Figure 7 at time $79\,\mu\mathrm{s}$. The second order variant of the method is used, with Van Leer limiter. The numerical solution is compared to the exact one, showing excellent agreement. This test is done with a uniform mesh involving 200 cells.

The phase's entropy show correct agreement with the exact solution. As the volume fraction is uniform and relaxation effects absent, the wave u_I has no influence in the Riemann problem solution. The entropy of each phase varies across shocks and contact discontinuities and is nearly constant in rarefaction waves.

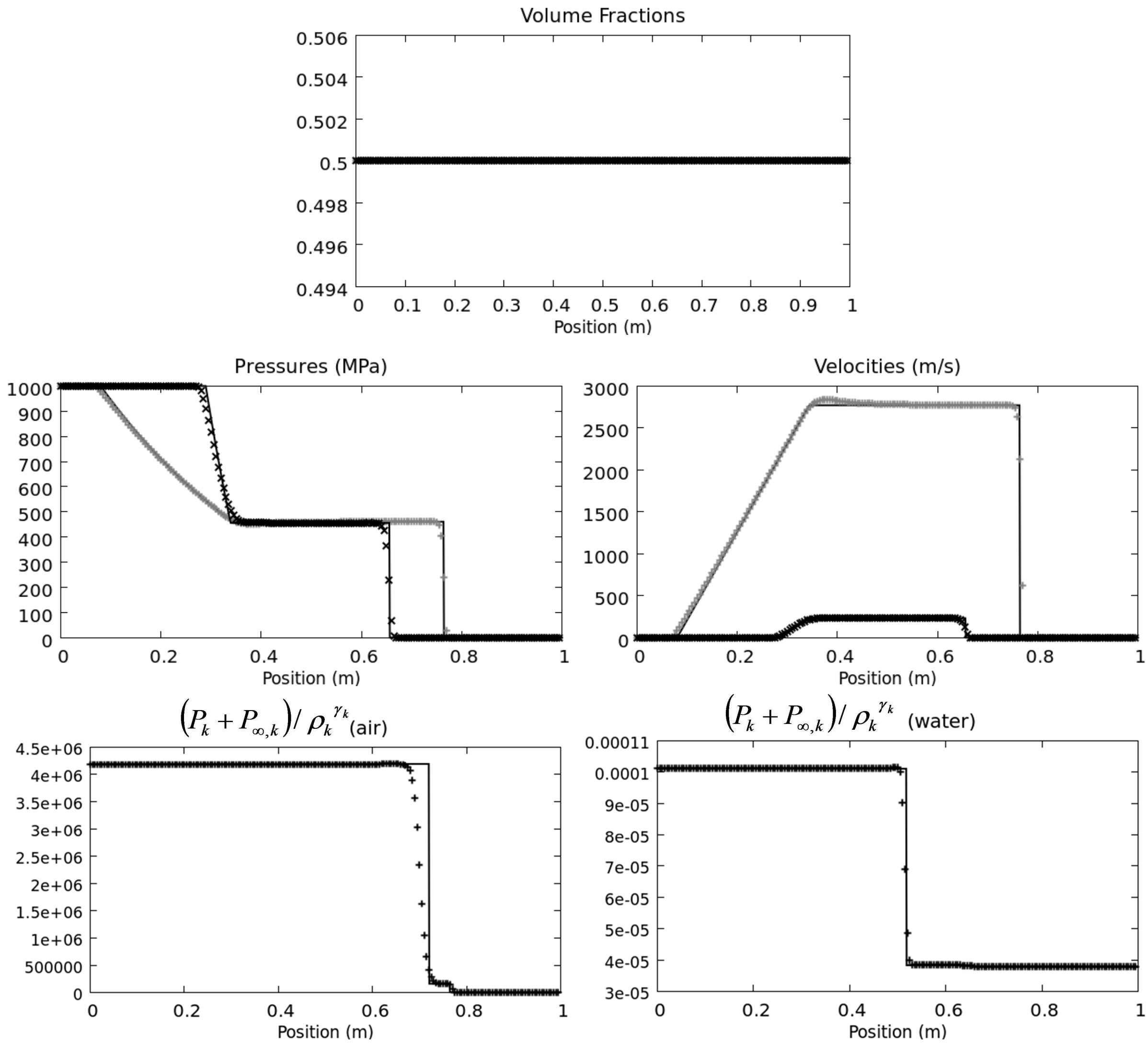

Figure 7: Two-phase shock tube with decoupled phase's evolutions. The initial volume fraction is uniform and relaxation effects are absent. The computations are made with the second order variant of the method, on a mesh involving 200 cells. Computed results are shown with symbols while exact ones are shown with lines.

Two-phase shock tube with volume fraction discontinuity - Interface separating two fluids

In the left chamber, nearly pure liquid water ($\alpha_1 = 1 - \varepsilon$ with $\varepsilon = 10^{-6}$) at the initial pressure of $2 \times 10^8\,\mathrm{Pa}$ is settled while in the right chamber is filled with nearly pure air ($\alpha_1 = \varepsilon$) at the initial pressure of $10^5\,\mathrm{Pa}$. In both chambers, liquid and gas have the same densities $1000\ \mathrm{kg/m^3}$ and $50\ \mathrm{kg/m^3}$ respectively. A volume fraction discontinuity is located at x=0.8 m and separates the high and low pressure chambers.

Computed results obtained with the second order scheme are shown in Figure 8 at time $276\mu\mathrm{s}$. The numerical solution in symbols is compared to the exact solution.

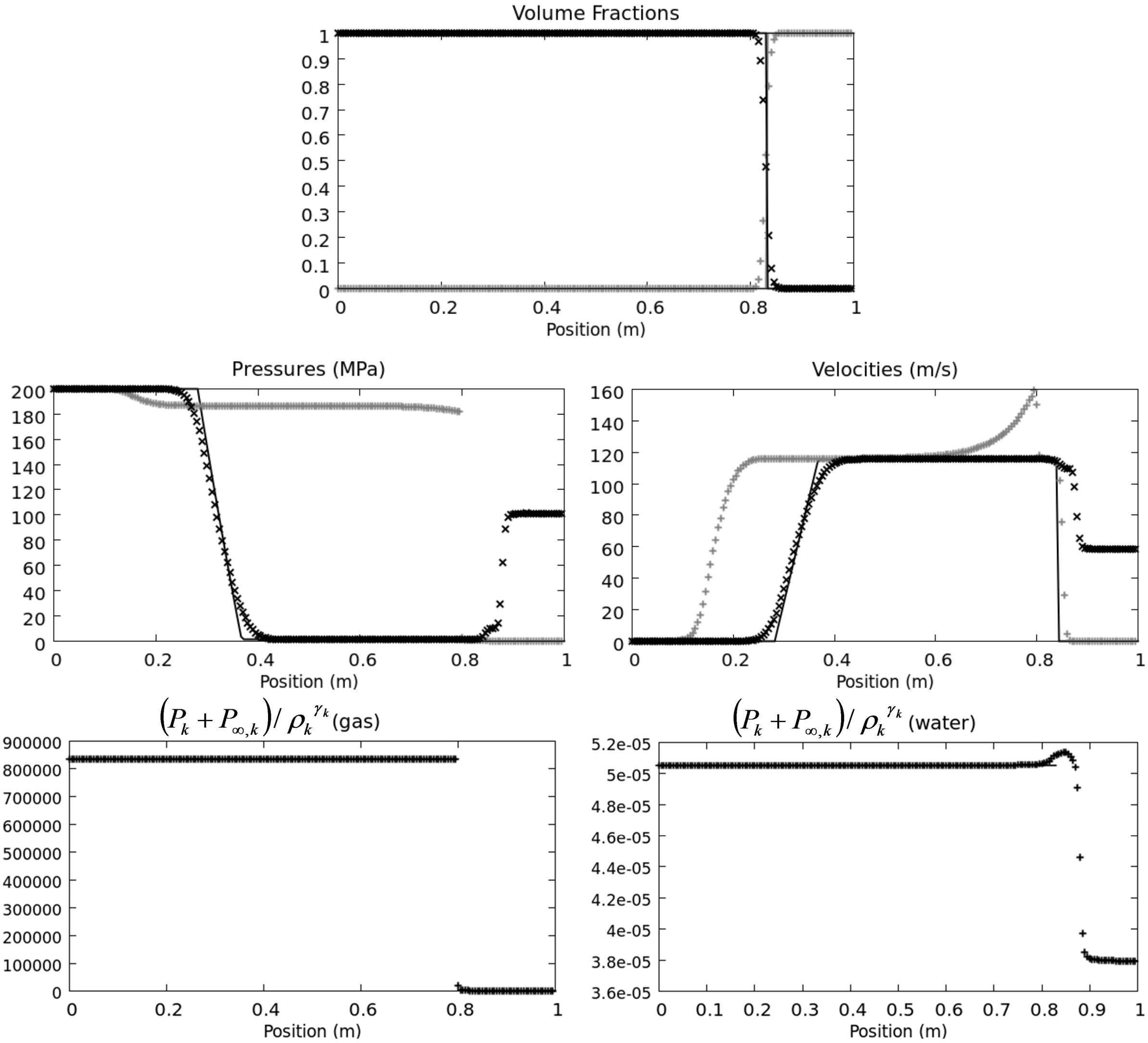
Volume Fractions

Pressures (MPa)

Velocities (m/s)

$\left(P_k + P_{\infty,k}\right)/\rho_k^{\gamma_k}$ (gas)

$\left(P_k + P_{\infty,k}\right)/\rho_k^{\gamma_k}$ (water)

Figure 8: Shock tube with an interface separating nearly pure liquid water and nearly pure gas. Computed results (in symbols) are compared to exact solution (in lines). Relaxation effects are absent. The computations are made with the second order variant of the method, on a mesh involving 200 cells.

In absence of relaxation terms, each fluid evolves with its own pressure and velocity as there is no interaction between fluids. This test puts in evidence the contribution of the non-conservative terms. In the left part of the shock tube, the liquid is nearly pure and is expanded by a strong rarefaction wave. The solution of this rarefaction wave is in excellent agreement with the exact one obtained with a pure liquid on the left and a pure gas on the right. In the left part of the shock tube, the gas is expanded too. It accelerates near the interface because its volume varies in space and time (gray symbols). In the right part of the shock tube, a shock wave propagates in the gas due to the liquid–gas interface motion. The gas variables are in good agreement with the exact solution. The liquid present in the right chamber with a negligible volume is also accelerated by the right facing shock wave (dark symbols). It can be noted that the liquid entropy in the right chamber increases exaggeratedly. But it occurs in a zone where the liquid is in very small proportions. This exaggerated entropy increase improves method's robustness and has no consequences on its accuracy.

The most important point is that interfacial pressure and velocity are perfectly matched, as shown in Figure 9. These results show that the numerical method is able to deal with multiphase mixtures in non-equilibrium velocities as well as interface problems separating pure or nearly pure materials. Interface conditions are matched as a consequence of non-conservative terms and do not need relaxation ones, that are absent in the present computations.

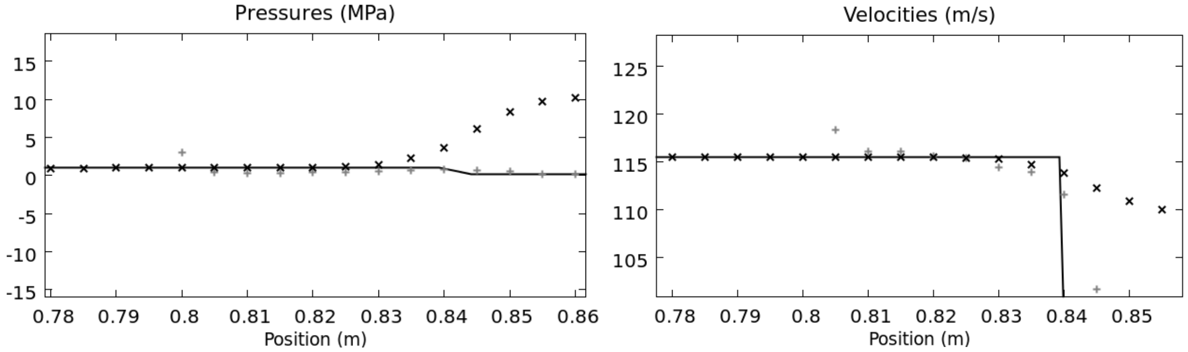

Figure 9: Magnified view of the pressure and velocity profiles obtained by the new method in the neighborhood of the interface. At position 0.8m perfect matching of the gas variables (gray symbols) and water ones (dark symbols) is clearly visible. Exact solutions are shown with lines.

Double expansion of a two-phase mixture

The initial volume fraction of the fluids is initially set to 0.5 everywhere, as well as densities and pressure of the fluids that are set uniform. The gas and liquid densities are respectively set to $10\,\mathrm{kg/m^3}$ and $1000\,\mathrm{kg/m^3}$. The pressure is set to 0.1 MPa. The initial velocities only are discontinuous at the domain centre. The two phases at left have the initial velocity of $-1000\ \mathrm{m/s}$ while the right part is set to $1000\ \mathrm{m/s}$. Results are shown at time $207\mu\mathrm{s}$ in Figure 10 and are obtained with the second order version of the method with Minmod limiter. The relative velocity is defined as the difference of the gas and liquid velocities. Stiff pressure relaxation is used everywhere contrarily to velocity drag that is absent. This test is done with a uniform mesh involving 200 cells.

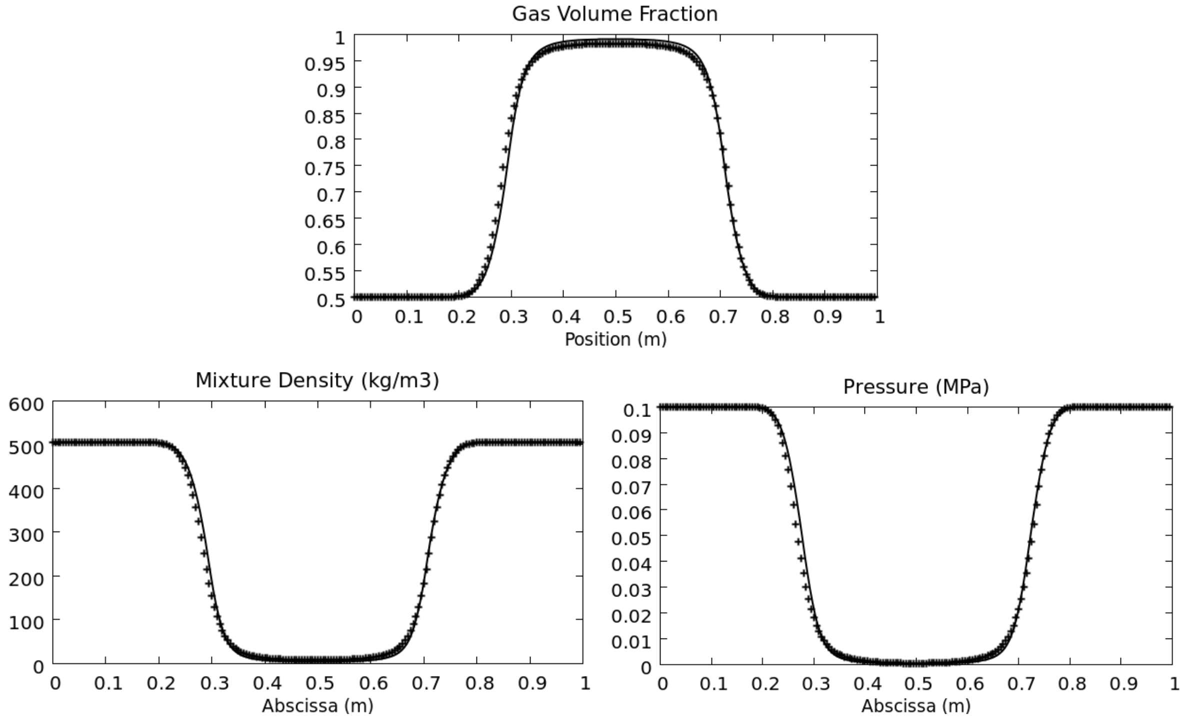

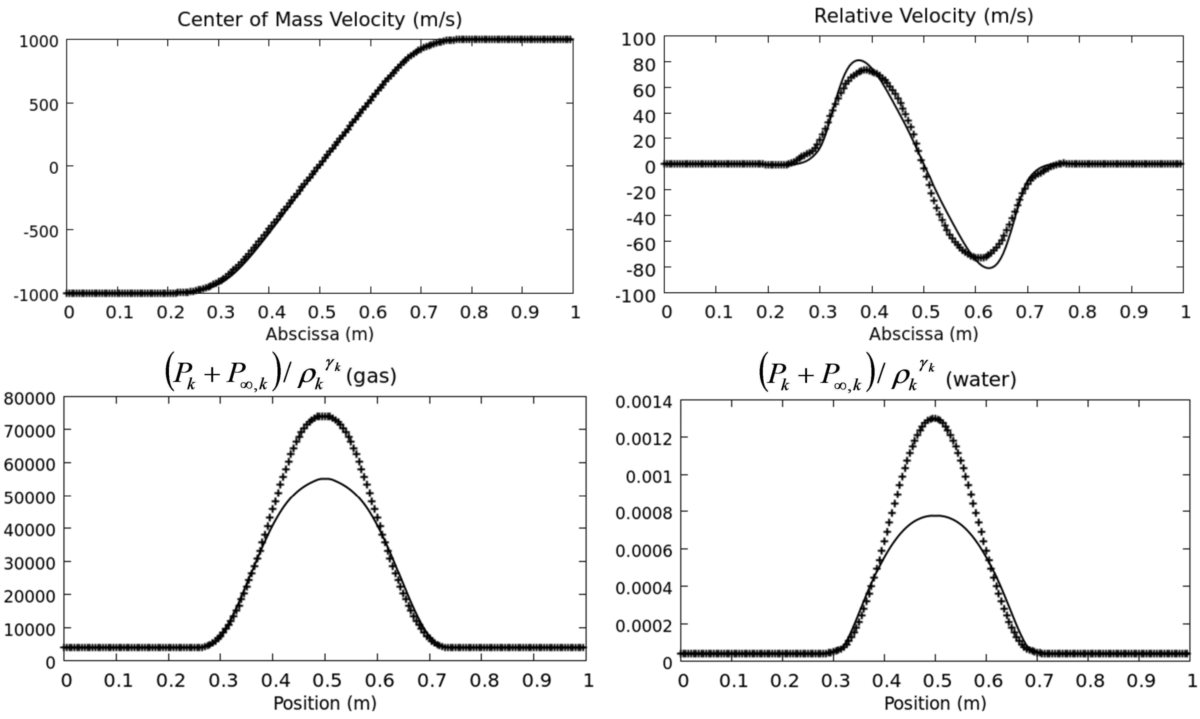

Figure 10: Double expansion test. Results of the new method are shown with symbols while those of the DEM are shown with lines. Large volume fraction increase appears at the tube center, as a consequence of pressure relaxation effects. Relative velocity also appears as a consequence of compressibility differences among the fluids. Results of the new method and those of the DEM are in good agreement. The new method produces more entropy than the DEM on this test problem.

It is worth to mention that entropy is produced in this test mainly across the interfaces (volume fraction gradient zones) that appear dynamically.

Sedimentation test problem

A 1 m height vertical tube is considered, filled with liquid water and air. The tube is closed at both ends. The initial volume fraction is set to 0.5 for both fluids, the pressure is set uniform to $10^5 \mathrm{Pa}$ as well as fluid's densities that are set to $1 \mathrm{kg/m^3}$ for the gas and $1000\ \mathrm{kg/m^3}$ for the liquid.

At $\mathrm{t} = 0$ the two-phase mixture is subjected to gravity $\mathrm{g} = 10 \mathrm{m/s^{-2}}$ acceleration. The heavy fluid falls down and the light one goes up. At equilibrium, the lower half tube is filled with water and the upper one with air. The results are shown in Figure 11 and show that the method is able to separate phases.

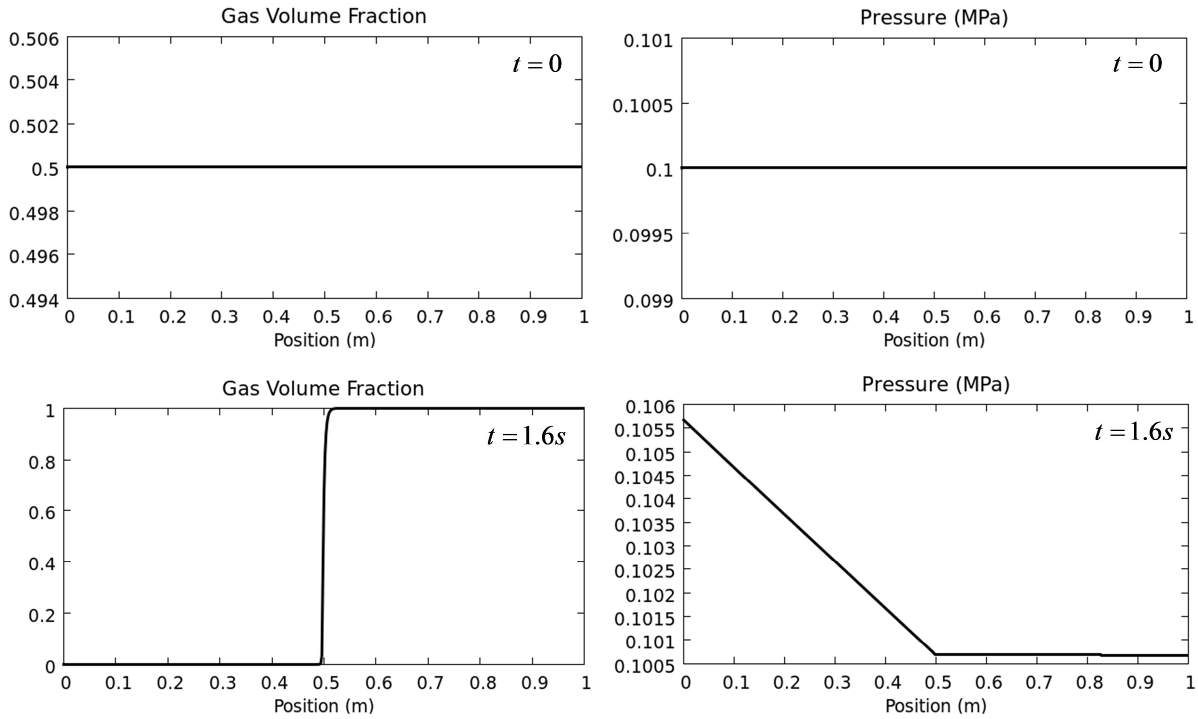

Figure 11: Sedimentation test problem. Initial data are shown in the upper graphs and the computed equilibrium state, reached after 1.6s is shown on bottom graphs.

Rogue et al. (1998) test problem

A vertical shock tube filled with air is considered as shown in Figure 12. A 2 cm particles bed is settled on a grid and is set to motion when the incident shock interacts with it. A wave refraction process occurs simultaneously: a transmitted shock propagates in the particles bed while a reflected shock wave is emitted. During particle motion, gas and particles have intense relative motion.

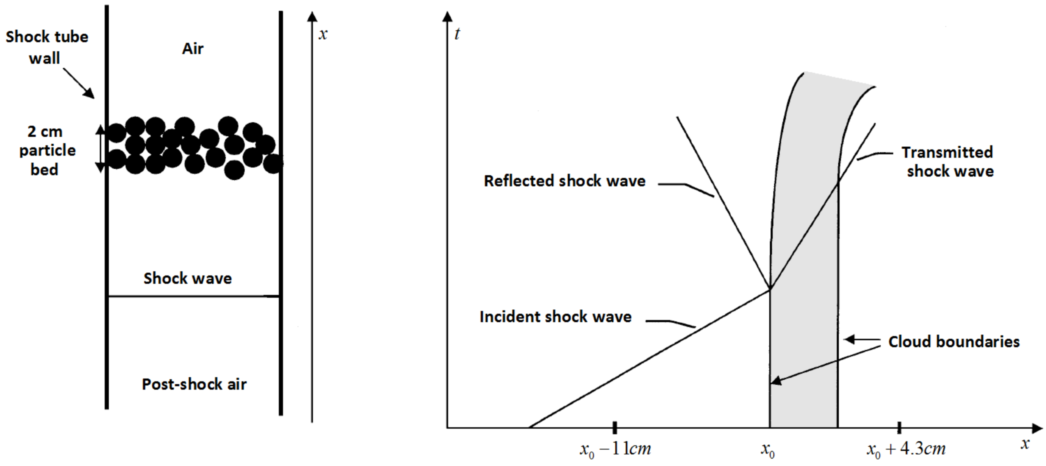

Figure 12: Schematic representation of the experimental facility of Rogue et al. (1998). A vertical shock tube is filled with air and a particle bed is settled on a grid. The incident shock wave interacts with the particle bed and induces its motion while reflected and transmitted shock waves are emitted.

Two pressure gauges are used to record the pressure history at two locations, before ($x_0 - 11\,\mathrm{cm}$) and after ($x_0 + 4.3\,\mathrm{cm}$) the particles bed. These pressures signals are used to validate the present computations.

In the present computations, solid particles are considered compressible and governed by the SG EOS, with the same parameters as water, as their compressibility is weak in the present pressure range.
In the following notations lowerscripts a and p represent respectively the air and particles.

Particles drag effects are modelled by the force, $F = A_I f_d$, where $A_I = 6\alpha_p / d_p$ represents the specific interfacial area and d_p represents the particles diameter.

The unit drag force f_d is expressed by Ergun (1952) correlation when the granular bed in compacted $(\alpha_p \geq \alpha_{cr})$ and by Bernecker and Price (1974) correlation when it becomes dilute:

$$f_d = \frac{1}{6\alpha_a} \rho_a (u_a - u_p) |u_a - u_p| C_d ,$$

$$C_d = \begin{cases} \dfrac{150\alpha_p}{R_e} + 1.75 & \alpha_p \geq \alpha_{cr} \\ \dfrac{150\,\alpha_p}{R_e} + 1.75 \left[\dfrac{(1-\alpha_{cr})\alpha_p}{\alpha_{cr}\alpha_a} \right]^{0.45} & (1-\alpha_S) \leq \alpha_p < \alpha_{cr} \\ \dfrac{150\alpha_p}{R_e} + 0.3 & \alpha_p < (1-\alpha_S) \end{cases}$$

with $\alpha_S = \left(1 + 0{,}02 \times \dfrac{1-\alpha_{cr}}{\alpha_{cr}} \right)^{-1}$ and $\alpha_{cr} = 0.63$.

In these formulas the particles Reynolds number is defined as: $R_e = \dfrac{d_p \alpha_a \rho_a |u_a - u_p|}{\mu_a}$.

Table 1 summarizes experimental data.

Parameter	**Value**
Air preshock density	$1.2\ \mathrm{kg/m^3}$
Incident shock Mach number	1.3
Particle density	$1050\ \mathrm{kg/m^3}$
Particle diameter (d_p)	$2\ \mathrm{mm}$
Particle bed thickness	$2\ \mathrm{cm}$
Initial gas volume fraction in the bed	0.35
Air viscosity (μ_a)	$2 \times 10^{-5}\ \mathrm{Pa.s}$

Table 1. Data of the Rogue et al. (1998) two-phase shock tube test.

The Rogue et al. (1998) pressure signals (grey symbols) are compared to the present computations (black symbols) in Figure 13, showing correct agreement. The computations are done with a mesh involving 1500 cells. Stiff pressure relaxation is used.

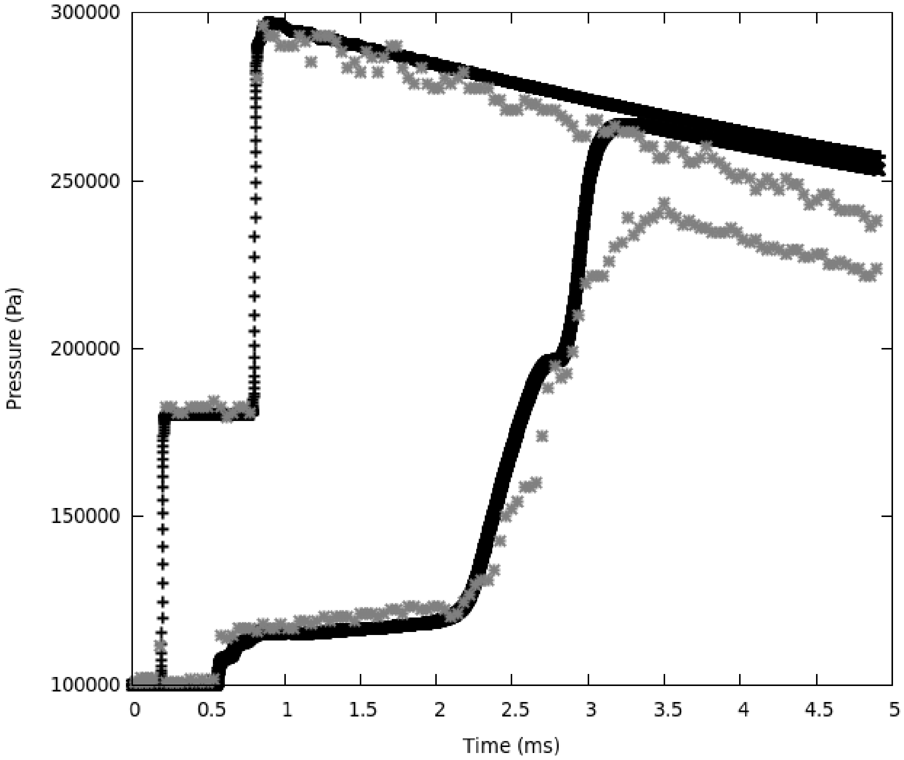

Figure 13: Comparison of recorded and computed pressure signals at the two pressure gauges for the Rogue test problem.

1.7.2. Velocity equilibrium two-phase flow tests

All tests that follow are done with a uniform mesh involving 200 cells. In these computations, both stiff pressure and velocity relaxation solvers of the Appendix 1.B and 1.C are used. Moreover, computed results are obtained with the second order method and Minmod limiter.

Interface separating two fluids

In the left chamber, nearly pure liquid water ($\alpha_1 = 1 - \varepsilon$ with $\varepsilon = 10^{-6}$) at the initial pressure of $2 \times 10^8 \mathrm{Pa}$ is settled while the right chamber is filled with nearly pure air ($\alpha_1 = \varepsilon$) at the initial pressure of $10^5 \mathrm{Pa}$. In both chambers, liquid and gas have the same densities $1000 \,\mathrm{kg/m^3}$ and $50 \,\mathrm{kg/m^3}$ respectively. A volume fraction discontinuity thus separates the high and low pressure chambers.

Computed results are shown in Figure 14 at time $291 \,\mu\mathrm{s}$. The numerical solution in symbols is compared to the exact one, determined from the Euler equations as both media are nearly pure.

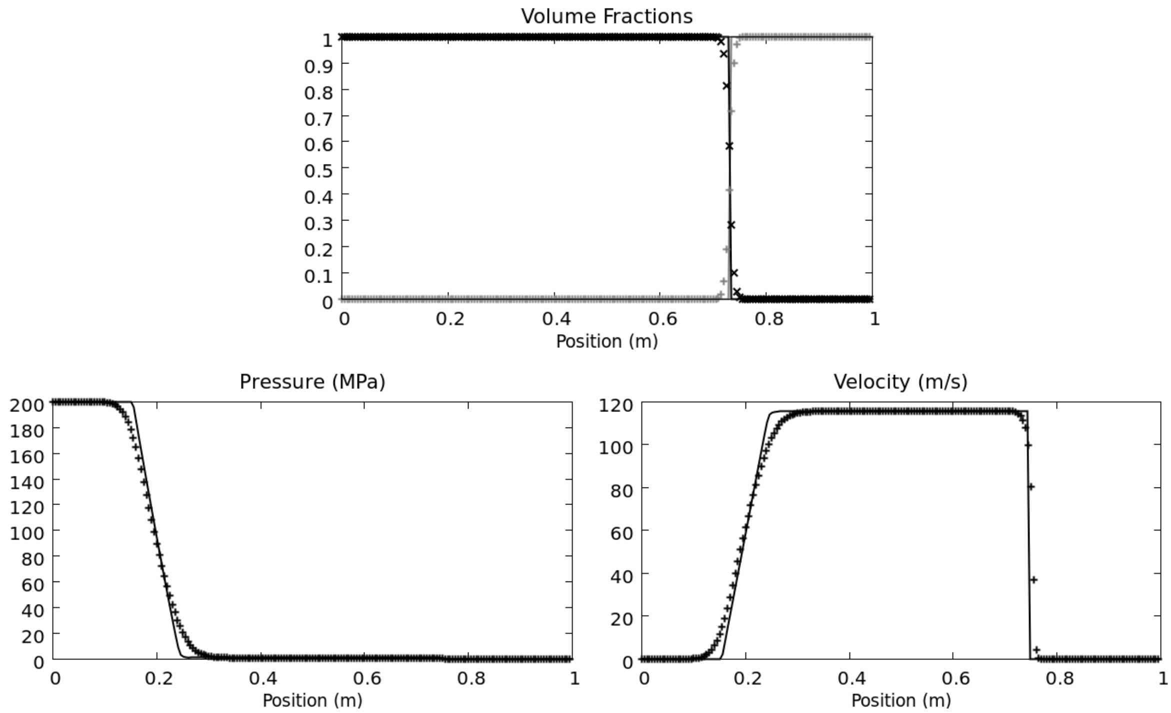

Figure 14: Shock tube with an interface separating nearly pure liquid water and nearly pure gas. Computed results (in symbols) are compared to the exact solution of the Euler equations (in lines). Perfect matching of interface conditions is observed, thanks to the stiff velocity and pressure relaxation solvers.

Shock tube with two mixtures

We now consider a mixture of two condensed phases, liquid water and aluminium. EOS parameters for the aluminium phase are $\gamma_{Al} = 3.4$ and $P_{\infty,Al} = 21.5\times10^9\,Pa$ while for the liquid EOS parameters are unchanged.

The volume fraction is set initially uniform ($\alpha_{Al} = 0.5$). The left chamber has the same high pressure for both phases ($10^9\,Pa$) while the right one has the same low pressure ($10^5 Pa$) for both phases. Aluminium and liquid densities are respectively set to $2700 kg/m^3$ and $1000\,kg/m^3$.

Stiff pressure and velocity relaxation is considered everywhere. In this context, volume fractions vary in both compression and expansion waves.

The limit model that is solved with the present method corresponds to the mechanical equilibrium model of Kapila et al. (2001). Computed results are shown with symbols in Figure 15 at time $111 \mu s$. They are compared to the exact solution of the Kapila model given in Petitpas et al. (2007).

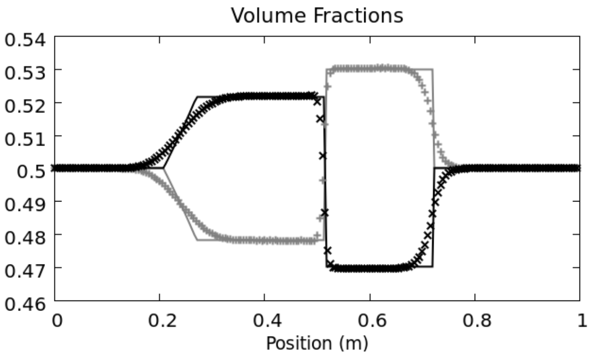

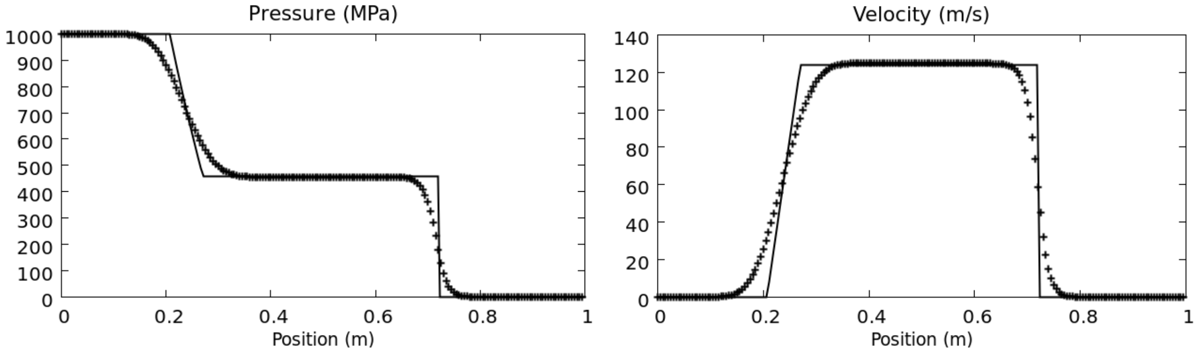

Figure 15: Shock tube with a high pressure chamber on the left containing a two-phase mixture and a low pressure chamber on the right filled by the same two-phase mixture. The computed results with the HLLC solver + mechanical relaxation in symbols are compared to the exact solution in lines, showing excellent agreement.

1.7.3. 3D computations

The present method is used in the context of 3D computations. To do this let us consider the 3D compressible two-phase system for a given phase k :

$$\begin{aligned}
&\frac{\partial \alpha_k}{\partial t} + \overrightarrow{u_I}.\vec{\nabla}\alpha_k = 0\\
&\frac{\partial \alpha_k\rho_k}{\partial t} + \mathrm{div}\left(\alpha_k\rho_k\overrightarrow{u_k}\right) = 0\\
&\frac{\partial \alpha_k\rho_k\overrightarrow{u_k}}{\partial t} + \mathrm{div}\left[\alpha_k\left(\rho_k\overrightarrow{u_k}\otimes\overrightarrow{u_k} + P_k\overline{\overline{I}}\right)\right] = P_I\vec{\nabla}\alpha_k\\
&\frac{\partial \alpha_k\rho_k E_k}{\partial t} + \mathrm{div}\left[\alpha_k\left(\rho_k E_k + P_k\right)\overrightarrow{u_k}\right] = P_I\overrightarrow{u_I}.\vec{\nabla}\alpha_k
\end{aligned}\tag{24}$$

Here, source terms (relaxation, heat and mass transfers, as well as body forces) have been omitted. Indeed, the 3D-extension of these terms does not present any particular difficulties.

The new method is implemented in the 3D code (DALPHADT) based on unstructured meshes made of tetrahedrons. In the following, we highlight the main extensions to consider.

3D two-phase flow model rewritting

System (24) is rewritten as,

$$\frac{\partial U_k}{\partial t} + \mathrm{div}\left(F_k\right) + \alpha_k\mathrm{div}\left(H_k\right) = 0, \tag{25}$$

with $U_k = \begin{pmatrix}\alpha_k\\ \alpha_k\rho_k\\ \alpha_k\rho_k\overrightarrow{u_k}\\ \alpha_k\rho_k E_k\end{pmatrix}$; $F_k = \begin{pmatrix}\alpha_k\overrightarrow{u_I}\\ \alpha_k\rho_k\overrightarrow{u_k}\\ \alpha_k\left(\rho_k\overrightarrow{u_k}\otimes\overrightarrow{u_k}\right) + \alpha_k\left(P_k - P_I\right)\overline{\overline{I}}\\ \alpha_k\left(\rho_k E_k + P_k\right)\overrightarrow{u_k} - \alpha_k P_I\overrightarrow{u_I}\end{pmatrix}$ and $H_k = \begin{pmatrix}-\overrightarrow{u_I}\\ \vec{0}\\ P_I\overline{\overline{I}}\\ P_I\overrightarrow{u_I}\end{pmatrix}$.

In the frame of 3D unstructured meshes, system (25) is integrated over the time step Δt and over a tetrahedral cell of volume V_i :

$$\int_{\Delta t}\int_{V_i}\frac{\partial U_k}{\partial t}dVdt+\int_{\Delta t}\int_{V_i}\mathrm{div}\left(F_k\right)dVdt+\int_{\Delta t}\int_{V_i}\alpha_k\mathrm{div}\left(H_k\right)dVdt=0$$

Fluxes are assumed constant during the time step. Thus, the previous equation becomes:

$$V_i\left(U_{k,i}^{n+1}-U_{k,i}^{n}\right)+\Delta t\left(\int_{V_i}\mathrm{div}\left(F_k\right)dV+\int_{V_i}\alpha_k\mathrm{div}\left(H_k\right)dV\right)=0. \quad (26)$$

To reuse concepts of the 1D Godunov type scheme (Section 1.6.), the volume fraction α_k appearing in the term $\int_{V_i}\alpha_k\mathrm{div}\left(H_k\right)dV$ is assumed to be the cell average volume fraction which is known at time t^n. Expression (26) is rewritten as,

$$V_i\left(U_{k,i}^{n+1}-U_{k,i}^{n}\right)+\Delta t\left(\int_{V_i}\mathrm{div}\left(F_k\right)dV+\alpha_{k,i}^{n}\int_{V_i}\mathrm{div}\left(H_k\right)dV\right)=0$$

Using the Green-Ostrogradski theorem, we introduce the cell surface S_i and its normal vector $\vec{\eta}$ to obtain:

$$V_i\left(U_{k,i}^{n+1}-U_{k,i}^{n}\right)+\Delta t\left(\int_{S_i}F_k.\vec{\eta}dS+\alpha_{k,i}^{n}\int_{S_i}H_k.\vec{\eta}dS\right)=0.$$

Finally, the Godunov type scheme reads,

$$U_{k,i}^{n+1}=U_{k,i}^{n}-\frac{\Delta t}{V_i}\left[\sum_{f=1}^{4}\left(F_k^*.\vec{\eta}\right)_f S_f+\alpha_{k,i}^{n}\sum_{f=1}^{4}\left(H_k^*.\vec{\eta}\right)_f S_f\right]$$

with $\left(F_k^*.\vec{\eta}\right)_f$ represents the flux solution of the Riemann problem solved on a given face f along the face normal vector $\overrightarrow{\eta_f}$. S_f represents the face area.

Remark: Denoting $u_I\equiv\overrightarrow{u_I}.\overrightarrow{\eta_f}$ the interfacial velocity calculated on a given face along the face normal vector $\overrightarrow{\eta_f}$, the following "fluxes" are obtained:

$$F_k.\overrightarrow{\eta_f}=\begin{pmatrix}\alpha_k u_I\\ \alpha_k\rho_k\overrightarrow{u_k}.\overrightarrow{\eta_f}\\ \alpha_k\rho_k\left(\overrightarrow{u_k}.\overrightarrow{\eta_f}\right)\overrightarrow{u_k}+\alpha_k\left(P_k-P_I\right)\overrightarrow{\eta_f}\\ \alpha_k\left(\rho_k E_k+P_k\right)\overrightarrow{u_k}.\overrightarrow{\eta_f}-\alpha_k P_I u_I\end{pmatrix} \text{ and } H_k.\overrightarrow{\eta_f}=\begin{pmatrix}-u_I\\ \vec{0}\\ P_I\overrightarrow{\eta_f}\\ P_I u_I\end{pmatrix}.$$

Phase-k Riemann solver

The new HLLC solver is used to compute the cell boundary fluxes along the face normal vector (Figure 16).

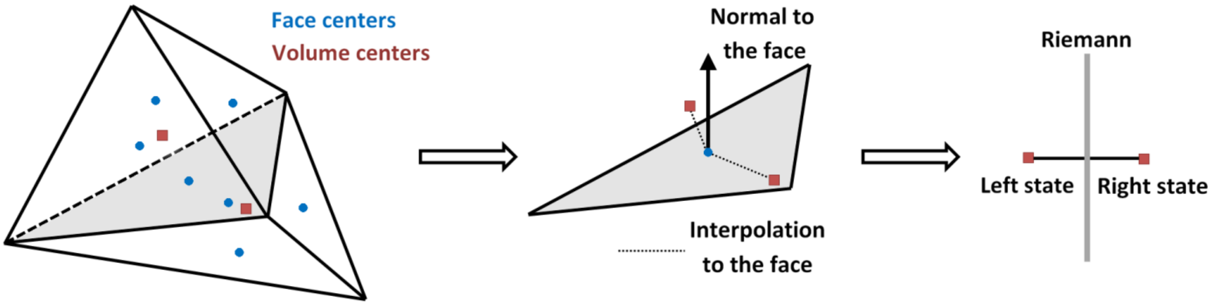

Figure 16: Schematic representation of a tetrahedron cell. The Riemann problem is solved on each face along the face normal vector.

The variables u_I and P_I being local constants on a given face, the Riemann problem for a given phase is based on local conservative formulations of (25):

$$\frac{\partial U_k}{\partial t} + \mathrm{div}\left(F_k\right) = 0 .$$

The Rankhine-Hugoniot (RH) relations across a wave of speed σ and on a given face of normal $\overrightarrow{\eta_f}$ thus read:

$$F_k.\overrightarrow{\eta_f} - \sigma U_k = \begin{pmatrix} \alpha_k\left(u_I - \sigma\right) \\ \alpha_k\rho_k\left(\overrightarrow{u_k}.\overrightarrow{\eta_f} - \sigma\right) \\ \alpha_k\rho_k\left(\overrightarrow{u_k}.\overrightarrow{\eta_f} - \sigma\right)\overrightarrow{u_k} + \alpha_k\left(P_k - P_I\right)\overrightarrow{\eta_f} \\ \alpha_k\rho_k E_k\left(\overrightarrow{u_k}.\overrightarrow{\eta_f} - \sigma\right) + \alpha_k\left(P_k\overrightarrow{u_k}.\overrightarrow{\eta_f} - P_I u_I\right) \end{pmatrix} = \text{cst} \text{ , with } \sigma \in \left\{S_{L,k}, S_{R,k}, S_{M,k}, u_I\right\}$$

For example, $\sigma = S_{L,k}$. In this case, the RH relation links the state $W^*_{L,k}$ to $W_{L,k}$ and becomes:

$$\left(F_k.\overrightarrow{\eta_f}\right)^*_L - S_{L,k}U^*_{L,k} = \left(F_k.\overrightarrow{\eta_f}\right)_L - S_{L,k}U_{L,k}$$

So the state $W^*_{L,k}$ depends on the state $W_{L,k}$ as follows :

$$\alpha^*_{L,k} = \alpha_{L,k}$$

$$\rho^*_{L,k} = \rho_{L,k}\frac{\overrightarrow{u_{L,k}}.\overrightarrow{\eta_f} - S_{L,k}}{S_{M,k} - S_{L,k}}$$

$$P^*_{L,k} = P_{L,k} + \rho_{L,k}\left(\overrightarrow{u_{L,k}}.\overrightarrow{\eta_f} - S_{L,k}\right)\left(\overrightarrow{u_{L,k}}.\overrightarrow{\eta_f} - S_{M,k}\right)$$

$$E^*_{L,k} = E_{L,k} + \frac{P_{L,k}\overrightarrow{u_{L,k}}.\overrightarrow{\eta_f} - P^*_{L,k}S_{M,k}}{\rho_{L,k}\left(\overrightarrow{u_{L,k}}.\overrightarrow{\eta_f} - S_{L,k}\right)}$$

with $\overrightarrow{u^*_{L,k}}.\overrightarrow{\eta_f} = S_{M,k}$.

<u>Remark:</u> The velocity vector tangential to a given face is equal to $\overrightarrow{u^{\perp}_k} = \overrightarrow{u_k} - \left(\overrightarrow{u_k}.\overrightarrow{\eta_f}\right)\overrightarrow{\eta_f}$.

The velocity vector determined in the state $W^*_{L,k}$ thus reads:

$$\overrightarrow{u^*_{L,k}} = S_{M,k}\overrightarrow{\eta_f} + \overrightarrow{u^{\perp}_{L,k}} = S_{M,k}\overrightarrow{\eta_f} + \overrightarrow{u_{L,k}} - \left(\overrightarrow{u_{L,k}}.\overrightarrow{\eta_f}\right)\overrightarrow{\eta_f} = \overrightarrow{u_{L,k}} + \left(S_{M,k} - \left(\overrightarrow{u_{L,k}}.\overrightarrow{\eta_f}\right)\right)\overrightarrow{\eta_f}$$

We now consider 3D computational examples and some validations.

Explosive liquid water experiments

The experimental facility is schematized in Figure 17. It consists in a solid explosive cylinder surrounded by liquid water. As the explosive detonation is very fast, constant volume explosion assumption is used to compute gas detonation products pressure, that is about 70 Kbars. From this kind of cylindrical shock tube, a complex 3D flow emerges with gas jets along the symetry axis and particles radial jets, as shown in Figure 18.

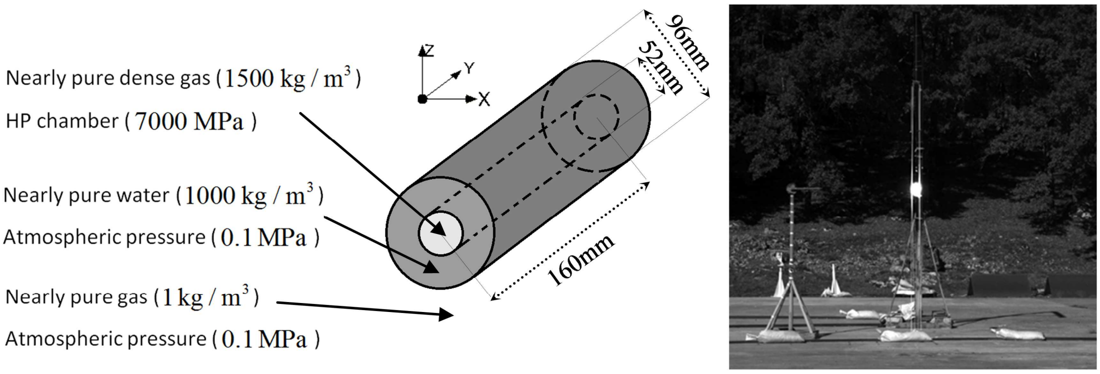

Figure 17: Schematic representation of the cylindrical gas-liquid explosion facility made at CEA Gramat. A cylindrical explosive charge is surrounded by a liquid water layer. The system is suspended in air as shown in the right photograph, fired and recorded with ultra-fast cameras.

To achieve 3D computations of this test problem the DALPHADT code is used with a mesh made of 2.383.176 tetrahedrons and with $\mathrm{CFL} = 0.5$.

In the following, front and side views of liquid water clouds are shown at two times in Figures 18 and 19. Numerical results are qualitatively compared to the experimental photographs, showing both good agreement and capabilites of the method.

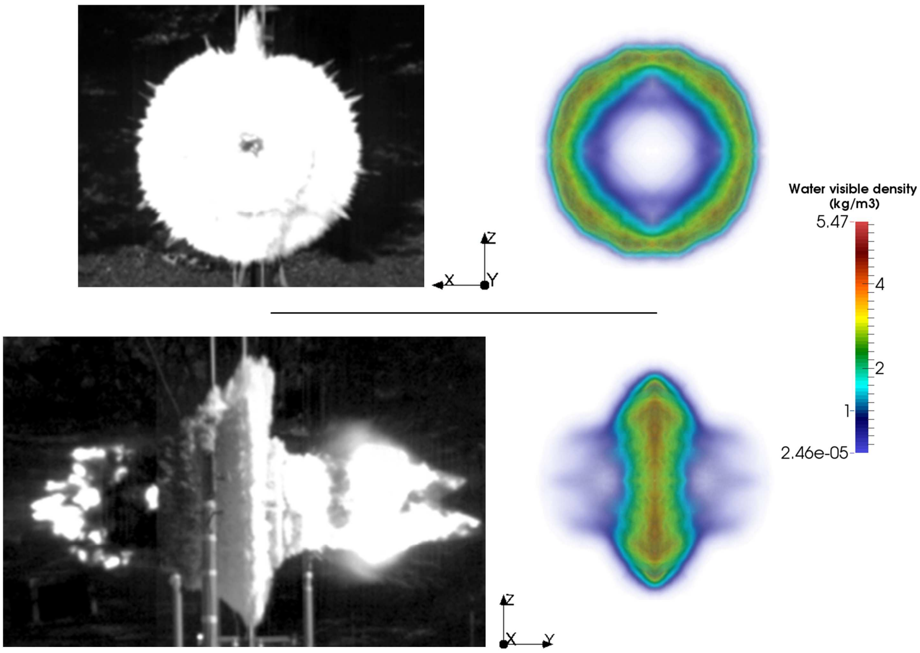

Figure 18: Comparison between experimental photographs (left) and numerical results (right) showing liquid droplet clouds at time $480\mu s$.

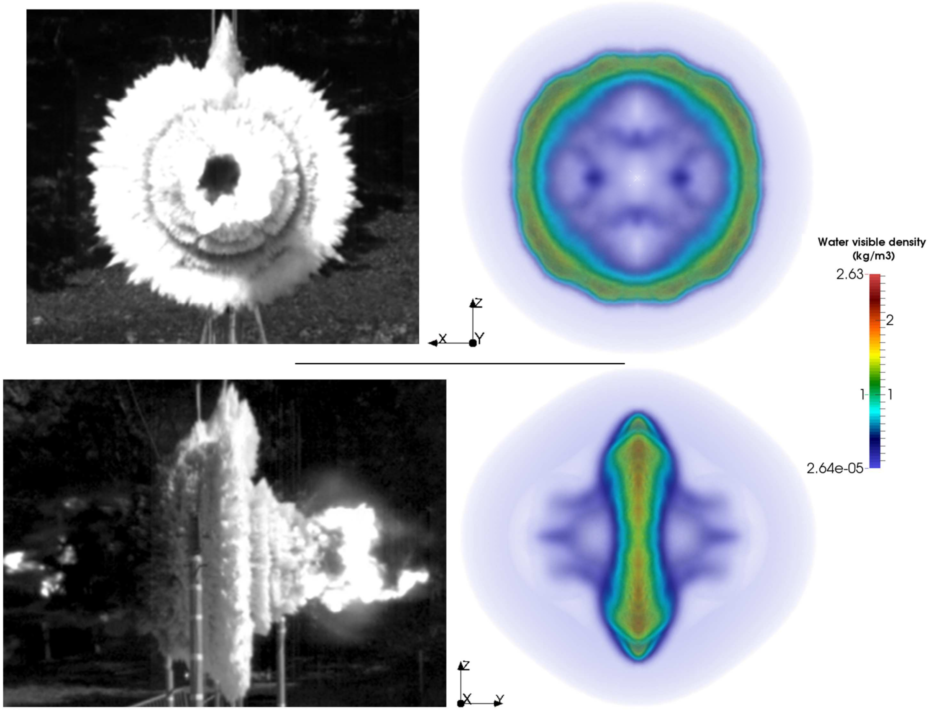

Figure 19: Same comparison as in Figure 18 showing liquid droplet clouds at time $1000\mu s$.

Then, we qualitatively compare this type of experiment (explosion in the open air) with an explosion inside a closed vessel (Figure 20).

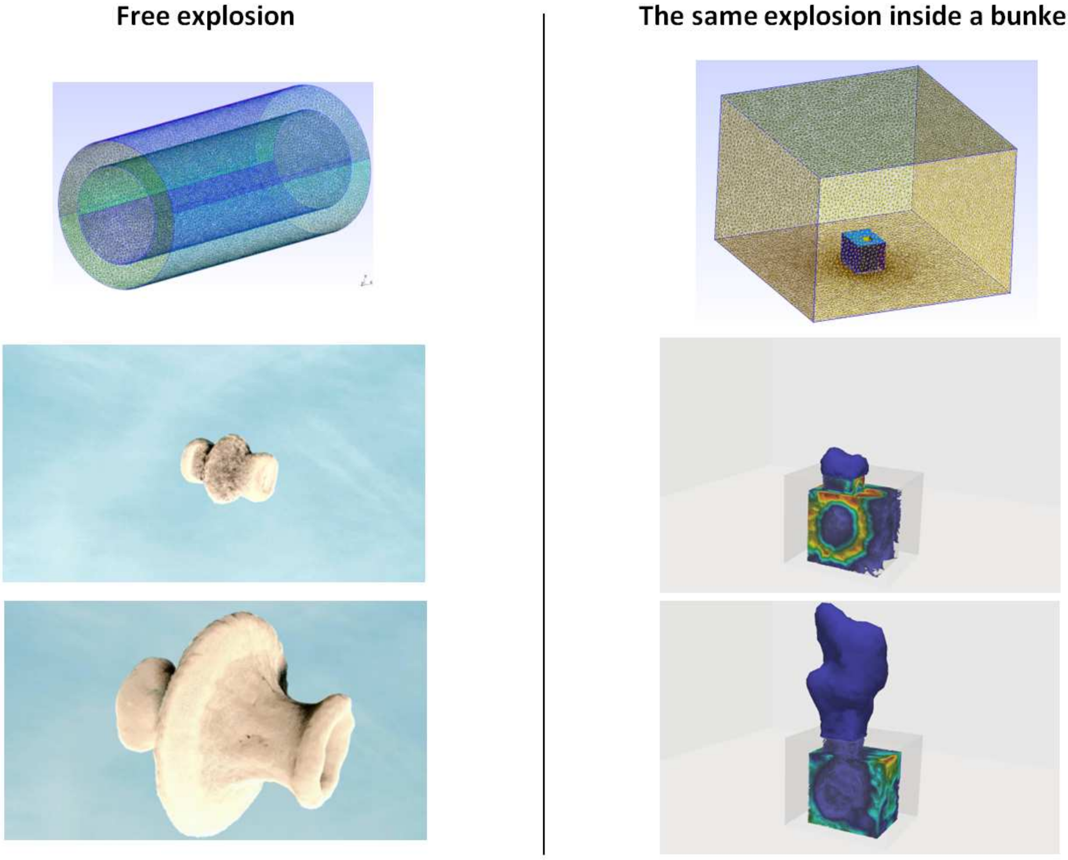
Free explosion

The same explosion inside a bunker

Figure 20: Same explosive charge with liquid layer, first in open air (left view) and second in a bunker, partly opened (right view). The results show liquid water contours at various times.

The method is thus able to deal with three-dimensional complex two-phase flows in high pressure conditions, with density and velocity gradients.

1.8. Conclusion

A new method has been built to solve non-equilibrium two-phase flows. This method is simpler than existing Godunov type schemes in this area and is of comparable accuracy and robustness as the DEM.

When dealing with a larger number of fluids, the new method is expected to be more and more efficient as it uses a single HLLC resolution per phase, while the DEM uses N^2 Riemann problem resolutions, where N represents the number of fluids. Also, its extension to implicit schemes seems much more tracktable than with the DEM.

Appendix 1.A. HLLC Riemann solver when $S_{L,k} < u_I < S_{M,k} < S_{R,k}$

The corresponding wave pattern is recalled in Figure 21.

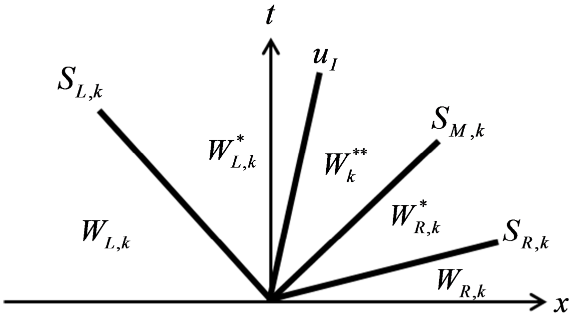

Figure 21: Wave pattern configuration when $S_{L,k} < u_I < S_{M,k} < S_{R,k}$ in the frame of HLLC approximation.

The Rankine-Hugoniot relations applied to the locally conservative system (5) read:

$$F^*_{L,k} = F_{L,k} + S_{L,k}\left(U^*_{L,k} - U_{L,k}\right),$$

$$F^*_{R,k} = F_{R,k} + S_{R,k}\left(U^*_{R,k} - U_{R,k}\right),$$

$$F^{**}_k = F^*_{R,k} + S_{M,k}\left(U^{**}_k - U^*_{R,k}\right),$$

$$F^*_{L,k} = F^{**}_k + u_I\left(U^*_{L,k} - U^{**}_k\right).$$

Vectors $U^*_{L,k}$, $U^*_{R,k}$ and U^{**}_k are determined following the same strategy as in Section 1.4.2.

– **State** $W^*_{R,k}$

$$\alpha^*_{R,k} = \alpha_{R,k},$$

$$(\alpha\rho)^*_{R,k} = (\alpha\rho)_{R,k}\frac{u_{R,k} - S_{R,k}}{S_{M,k} - S_{R,k}},$$

$$u^*_{R,k} = S_{M,k},$$

$$P^*_{R,k} = P_{R,k} + \rho_{R,k}\left(u_{R,k} - S_{R,k}\right)\left(u_{R,k} - S_{M,k}\right),$$

$$E^*_{R,k} = E_{R,k} + \frac{(Pu)_{R,k} - P^*_{R,k}S_{M,k}}{\rho_{R,k}\left(u_{R,k} - S_{R,k}\right)}.$$

– **State** $W^*_{L,k}$

$$\alpha^*_{L,k} = \alpha_{L,k} ,$$

$$(\alpha\rho)^*_{L,k} = (\alpha\rho)_{L,k} \frac{u_{L,k} - S_{L,k}}{S_{M,k} - S_{L,k}} ,$$

$$u^*_{L,k} = S_{M,k} ,$$

$$P^*_{L,k} = P_{L,k} + \rho_{L,k}(u_{L,k} - S_{L,k})(u_{L,k} - S_{M,k}),$$

$$E^*_{L,k} = E_{L,k} + \frac{(Pu)_{L,k} - P^*_{L,k} S_{M,k}}{\rho_{L,k}(u_{L,k} - S_{L,k})} .$$

– **State** W^{**}_k

$$\alpha^{**}_k = \alpha_{R,k} ,$$

$$(\alpha\rho)^{**}_k = (\alpha\rho)^*_{L,k} ,$$

$$u^{**}_k = S_{M,k} ,$$

$$P^{**}_k = P^*_{R,k} \quad \text{ou} \quad P^{**}_k = \frac{\alpha_{L,k}}{\alpha_{R,k}} P^*_{L,k} + \frac{\alpha_{R,k} - \alpha_{L,k}}{\alpha_{R,k}} P_I \qquad ,$$

$$E^{**}_k = E^*_{L,k} - \frac{\alpha_{R,k} - \alpha_{L,k}}{(\alpha\rho)^*_{L,k}} P_I .$$

Appendix 1.B. Stiff velocity relaxation solver

Stiff velocity relaxation is considered after wave dynamics, considered in the hyperbolic solver. When stiff drag interaction only is present, the system to solve is:

Phase1 Phase2

$$\frac{\partial \alpha_1}{\partial t} = 0 \qquad \frac{\partial \alpha_2}{\partial t} = 0$$

$$\frac{\partial \alpha_1 \rho_1}{\partial t} = 0 \qquad \frac{\partial \alpha_2 \rho_2}{\partial t} = 0$$

(C.1)

$$\frac{\partial \alpha_1 \rho_1 u_1}{\partial t} = \lambda(u_2 - u_1) \qquad \frac{\partial \alpha_2 \rho_2 u_2}{\partial t} = -\lambda(u_2 - u_1)$$

$$\frac{\partial \alpha_1 \rho_1 E_1}{\partial t} = \lambda \overline{u_I}(u_2 - u_1) \qquad \frac{\partial \alpha_2 \rho_2 E_2}{\partial t} = -\lambda \overline{u_I}(u_2 - u_1)$$

Knowledge of the drag coefficient λ is useless in the stiff velocity relaxation limit as this parameter is going to disappear. In this limit, $\lambda \to +\infty$.

The system above implies mass conservation for each phase and for the mixture:

$$(\alpha\rho)_k = \text{cte}$$

$$\rho = \sum_{k=1}^{2} (\alpha\rho)_k = \text{cte}$$

Consequently, mass fractions are constants during the relaxation process: $Y_k = \frac{(\alpha\rho)_k}{\rho} = \text{cte}$.

The velocity at relaxation is readily obtained as,

$$u^* = \sum_{k=1}^{2} Y_k^0 u_k^0 ,$$

where the superscript 0 denotes the state before relaxation (at the end of the hyperbolic step).

Combining the total energy and momentum equations of System (C.1) the following identities are obtained,

$$\frac{\partial(\alpha\rho E)_k}{\partial t} = \overline{u_I}\frac{\partial(\alpha\rho u)_k}{\partial t} .$$

With the help of mass conservation equations of the phases they become,

$$\frac{\partial E_k}{\partial t} = \overline{u_I}\frac{\partial u_k}{\partial t} .$$

As the relaxed velocity $u^* = \sum_{k=1}^{2} Y_k^0 u_k^0$ is a constant during the relaxation process, we assume $\overline{u_I} = \text{cte} = u^*$. Thanks to this assumption, the relaxed total energies read,

$$E_k^* = E_k^0 + u^*\left(u^* - u_k^0\right).$$

The associated relaxed internal energies read,

$$e_k^* = e_k^0 + \frac{1}{2}\left(u^* - u_k^0\right)\left(u^* - u_k^0\right).$$

Appendix 1.C. Stiff pressure relaxation solver

After wave propagation, velocity relaxation or any evolution process the pressures are in disequilibrium. The pressure relaxation time is usually very short, less than one microsecond. Also, when dealing with interfacial flows, stiff pressure and velocity relaxation are needed to fulfil interface conditions.

The system to consider reads:

$$\begin{array}{ll}
\underline{\text{Phase 1}} & \underline{\text{Phase 2}} \\
\dfrac{\partial\alpha_1}{\partial t} = \mu\left(P_1 - P_2\right) & \dfrac{\partial\alpha_2}{\partial t} = -\mu\left(P_1 - P_2\right) \\
\dfrac{\partial\alpha_1\rho_1}{\partial t} = 0 & \dfrac{\partial\alpha_2\rho_2}{\partial t} = 0 \\
\dfrac{\partial\alpha_1\rho_1 u_1}{\partial t} = 0 & \dfrac{\partial\alpha_2\rho_2 u_2}{\partial t} = 0 \\
\dfrac{\partial\alpha_1\rho_1 E_1}{\partial t} = -\mu\overline{P_I}\left(P_1 - P_2\right) & \dfrac{\partial\alpha_2\rho_2 E_2}{\partial t} = \mu\overline{P_I}\left(P_1 - P_2\right)
\end{array} \qquad (27)$$

The pressure relaxation coefficient μ has been determined for example in Saurel et al. (2003). Here, it is assumed to tend to infinity, $\mu \to +\infty$.

System (27) implies mass invariance for each phase and for the mixture:

$$(\alpha\rho)_k = \text{cte}$$

$$\rho = \sum_{k=1}^{2}(\alpha\rho)_k = \text{cte}$$

Velocity of the phases stays invariant too.

Combining the total energy and volume fraction equations, the relaxation term vanishes,

$$\frac{\partial(\alpha\rho E)_k}{\partial t} = -\overline{P_I}\frac{\partial\alpha_k}{\partial t} .$$

With the help of the mass conservation equation of the phase it reduces to,

$$\frac{\partial E_k}{\partial t} = -\overline{P_I}\frac{\partial v_k}{\partial t},$$

where v_k denotes the specific volume of phase k .

Assuming $\overline{P_I} = P^*$, the relaxed pressure, integration of the former equations read,

$$E_k^* = E_k^0 - P^*\left(v_k^* - v_k^0\right),$$

or alternatively,

$$e_k^* = e_k^0 - P^*\left(v_k^* - v_k^0\right). \tag{28}$$

When each phase is governed by the ‘stiffened-gas’ equation of state (EOS) given by (23), the relaxed pressure is determined analytically. For other convex equation of state, an iterative method is needed (see for example Lallemand and Saurel, 2000).

Inserting the EOS in (28) a relation linking the pressure and the specific volume of the phases is obtained:

$$v_k^* = \frac{v_k^0}{\gamma_k}\left(\gamma_k - 1 + \frac{P_k^0 + P_{\infty,k}}{P^* + P_{\infty,k}}\right)$$

With the help of the mass invariance of the phases it becomes:

$$\alpha_k^* = \frac{\alpha_k^0}{\gamma_k}\left(\gamma_k - 1 + \frac{P_k^0 + P_{\infty,k}}{P^* + P_{\infty,k}}\right) = \alpha_k^0 + \frac{\alpha_k^0}{\gamma_k}\left(\frac{P_k^0 + P_{\infty,k}}{P^* + P_{\infty,k}} - 1\right)$$

The saturation constraint ($\sum_{k=1}^{2}\alpha_k^* = \sum_{k=1}^{2}\alpha_k^0 = 1$) provides the closure relation:

$$\sum_{k=1}^{2}\frac{\alpha_k^0}{\gamma_k}\left(\frac{P_k^0 + P_{\infty,k}}{P^* + P_{\infty,k}}\right) = \sum_{k=1}^{2}\frac{\alpha_k^0}{\gamma_k}.$$

This equation admits a positive root: $P^* = \frac{1}{2}\left(A_1 + A_2 - P_{\infty,1} - P_{\infty,2}\right) + \sqrt{\frac{1}{4}\left(A_2 - A_1 - P_{\infty,2} + P_{\infty,1}\right)^2 + A_1A_2}$.

With the following notations, $A_1 = \dfrac{\frac{\alpha_1^0}{\gamma_1}\left(P_1^0 + P_{\infty,1}\right)}{\frac{\alpha_1^0}{\gamma_1} + \frac{\alpha_2^0}{\gamma_2}}$ and $A_2 = \dfrac{\frac{\alpha_2^0}{\gamma_2}\left(P_2^0 + P_{\infty,2}\right)}{\frac{\alpha_1^0}{\gamma_1} + \frac{\alpha_2^0}{\gamma_2}}$.

Appendix 1.D. Non conservative terms in the numerical scheme – Other flow configurations

In Section 1.6., we showed agreement between the discrete form of the term $\alpha_k\frac{\partial H_k}{\partial x}$ and the DEM one. Demonstration was made in the case of a positive flow velocity at both cell boundaries and decreasing volume fraction profile. Let us now consider the other flow configurations, in order to justify in a general way the discrete form we use.

The calculations are specified for phase 1. We have to compare both expressions,

$$(\alpha H)^*_{1,i+\frac{1}{2}} - (\alpha H)^*_{1,i-\frac{1}{2}} - \alpha^n_{1,i}\left(H^*_{1,i+\frac{1}{2}} - H^*_{1,i-\frac{1}{2}}\right) =$$

$$= \left(\alpha^n_{1,i}\left(\frac{u_I^+}{|u_I|}\right)_{i+1/2} - \alpha^n_{1,i+1}\left(\frac{u_I^-}{|u_I|}\right)_{i+1/2} - \alpha^n_{1,i}\right)H^*_{1,i+\frac{1}{2}} + \left(\alpha^n_{1,i} - \alpha^n_{1,i-1}\left(\frac{u_I^+}{|u_I|}\right)_{i-1/2} + \alpha^n_{1,i}\left(\frac{u_I^-}{|u_I|}\right)_{i-1/2}\right)H^*_{1,i-\frac{1}{2}}$$

and

$$F^{Lag,1}_{i+1/2} + F^{Lag,1}_{i-1/2} = \left(\frac{u^{*,-}_{12}}{\left|u^{*}_{12}\right|}\right)_{i+1/2} \mathrm{Max}\left(0, \alpha^n_{1,i} - \alpha^n_{1,i+1}\right) f^{Lag*}_{12}\left(w^n_{1,i}, w^n_{2,i+1}\right) - \left(\frac{u^{*,-}_{21}}{\left|u^{*}_{21}\right|}\right)_{i+1/2} \mathrm{Max}\left(0, \alpha^n_{1,i+1} - \alpha^n_{1,i}\right) f^{Lag,*}_{21}\left(w^n_{2,i}, w^n_{1,i+1}\right)$$

$$- \left(\frac{u^{*,+}_{12}}{\left|u^{*}_{12}\right|}\right)_{i-1/2} \mathrm{Max}\left(0, \alpha^n_{1,i-1} - \alpha^n_{1,i}\right) f^{Lag*}_{12}\left(w^n_{1,i-1}, w^n_{2,i}\right) + \left(\frac{u^{*,+}_{21}}{\left|u^{*}_{21}\right|}\right)_{i-1/2} \mathrm{Max}\left(0, \alpha^n_{1,i} - \alpha^n_{1,i-1}\right) f^{Lag,*}_{21}\left(w^n_{2,i-1}, w^n_{1,i}\right)$$

– Let us consider the example of a flow at positive velocity at both cell boundaries. Moreover we assume a monotonic increasing volume fraction profile,

$$\alpha^n_{1,i-1} < \alpha^n_{1,i} < \alpha^n_{1,i+1}.$$

The former expressions reduce respectively to,

$$(\alpha H)^*_{1,i+\frac{1}{2}} - (\alpha H)^*_{1,i-\frac{1}{2}} - \alpha^n_{1,i}\left(H^*_{1,i+\frac{1}{2}} - H^*_{1,i-\frac{1}{2}}\right) = \left(\alpha^n_{1,i} - \alpha^n_{1,i-1}\right) H^*_{1,i-\frac{1}{2}},$$

and,

$$F^{Lag,1}_{i+1/2} + F^{Lag,1}_{i-1/2} = \left(\alpha^n_{1,i} - \alpha^n_{1,i-1}\right) f^{Lag,*}_{21}\left(w^n_{2,i-1}, w^n_{1,i}\right).$$

In the present context, the only fluids contact to consider is contact 2-1. In this situation,

$$H^*_{1,i-\frac{1}{2}} = f^{Lag,*}_{21}\left(w^n_{2,i-1}, w^n_{1,i}\right).$$

This example shows agreement between the discrete form $\alpha^n_{k,i}\left(H^*_{k,i+\frac{1}{2}} - H^*_{k,i-\frac{1}{2}}\right)$ and the DEM one.

– It's easy to show that the example of a flow at negative velocity at both cell boundaries also shows agreement between $\alpha^n_{k,i}\left(H^*_{k,i+\frac{1}{2}} - H^*_{k,i-\frac{1}{2}}\right)$ and the DEM discrete form.

– Finally, let us consider a more complicated type of flow. We assume a positive velocity at the left cell boundary, and a negative one at the right cell boundary. Besides we suppose the following volume fraction profile,

$$\alpha^n_{1,i-1} > \alpha^n_{1,i} < \alpha^n_{1,i+1}.$$

Thus, we obtain,

$$(\alpha H)^*_{1,i+\frac{1}{2}} - (\alpha H)^*_{1,i-\frac{1}{2}} - \alpha^n_{1,i}\left(H^*_{1,i+\frac{1}{2}} - H^*_{1,i-\frac{1}{2}}\right) = \left(\alpha^n_{1,i+1} - \alpha^n_{1,i}\right) H^*_{1,i+\frac{1}{2}} + \left(\alpha^n_{1,i} - \alpha^n_{1,i-1}\right) H^*_{1,i-\frac{1}{2}}$$

and,

$$F^{Lag,1}_{i+1/2} + F^{Lag,1}_{i-1/2} = \left(\alpha^n_{1,i+1} - \alpha^n_{1,i}\right) f^{Lag,*}_{21}\left(w^n_{2,i}, w^n_{1,i+1}\right) + \left(\alpha^n_{1,i} - \alpha^n_{1,i-1}\right) f^{Lag*}_{12}\left(w^n_{1,i-1}, w^n_{2,i}\right).$$

In the present context, the fluids contact to consider at the left boundary cell is contact 1-2. In this situation, $H^*_{1,i-\frac{1}{2}} = f^{Lag*}_{12}\left(w^n_{1,i-1}, w^n_{2,i}\right)$.

On the contrary, the fluids contact to consider at the right boundary cell is contact 2-1. We have too,

$$H^*_{1,i+\frac{1}{2}} = f^{Lag,*}_{21}\left(w^n_{2,i}, w^n_{1,i+1}\right).$$

All these flow configurations show agreement between the discrete form $\alpha^n_{k,i}\left(H^*_{k,i+\frac{1}{2}} - H^*_{k,i-\frac{1}{2}}\right)$ and the DEM one.

Chapitre 2

Construction d'une technique numérique pour la répartition de l'énergie d'une onde de choc dans les différentes phases

2.1. Introduction

When a shock wave (or a detonation wave) propagates in heterogeneous media the computation of the shocked state requires the correct estimation of the energy of all phases. The main difficulty consists in enforcing the correct energy at a discrete level in agreement with the shock relations of Saurel et al. (2007). Indeed, the flow model cannot be written in conservative form, then specific shock relations are necessary. These relations enforce the jumps of non-conservative variables such as internal energies or volume fractions. The difficulty now consists in enforcing these jumps at the discrete level (Hou & Le Floch, 1994).

To illustrate this issue in the context of the model equations used in this work, we analyze the numerical results obtained when no special care is taken. The test case is a shock-tube problem of 1m composed of two chambers separated by an interface localized at 0.6m from the left boundary. Both chambers contain the same mixture of epoxy and spinel governed by the stiffened gas EOS. The initial density of the epoxy is set to $\rho_{\mathrm{epoxy}} = 1185\ \mathrm{kg.m}^{-3}$ with EOS parameters $\gamma_{\mathrm{epoxy}} = 2.43$ and $P_{\infty,\mathrm{epoxy}} = 5.3\,10^{9}\ \mathrm{Pa}$. The initial density of the spinel is set to $\rho_{\mathrm{spinel}} = 3622\ \mathrm{kg.m}^{-3}$ with EOS parameters $\gamma_{\mathrm{spinel}} = 1.62$ and $P_{\infty,\mathrm{spinel}} = 141.10^{9}\ \mathrm{Pa}$. The initial volume fraction is set to $\alpha_{\mathrm{epoxy}} = 0.5954$ ($\alpha_{\mathrm{spinel}} = 1 - \alpha_{\mathrm{epoxy}}$). This value corresponds to the the one used in the experiments of Marsh (1980). The pressure in the left chamber is set to $2.10^{11}\ \mathrm{Pa}$, atmospheric pressure is set in the right chamber. When the membrane collapses a two-phase shock-tube problem develops. 1D results based on the method described in Chapter 1 are compared to the exact solution at $t = 32\mu s$ in Figure 22 illustrating the difficulty to reach post-shock state convergence. In this test case instantaneous velocity and pressure relaxation solvers are used in order to recover the asymptotic model of Kapila (2001) and validity of Saurel et al. (2007) shock relations.

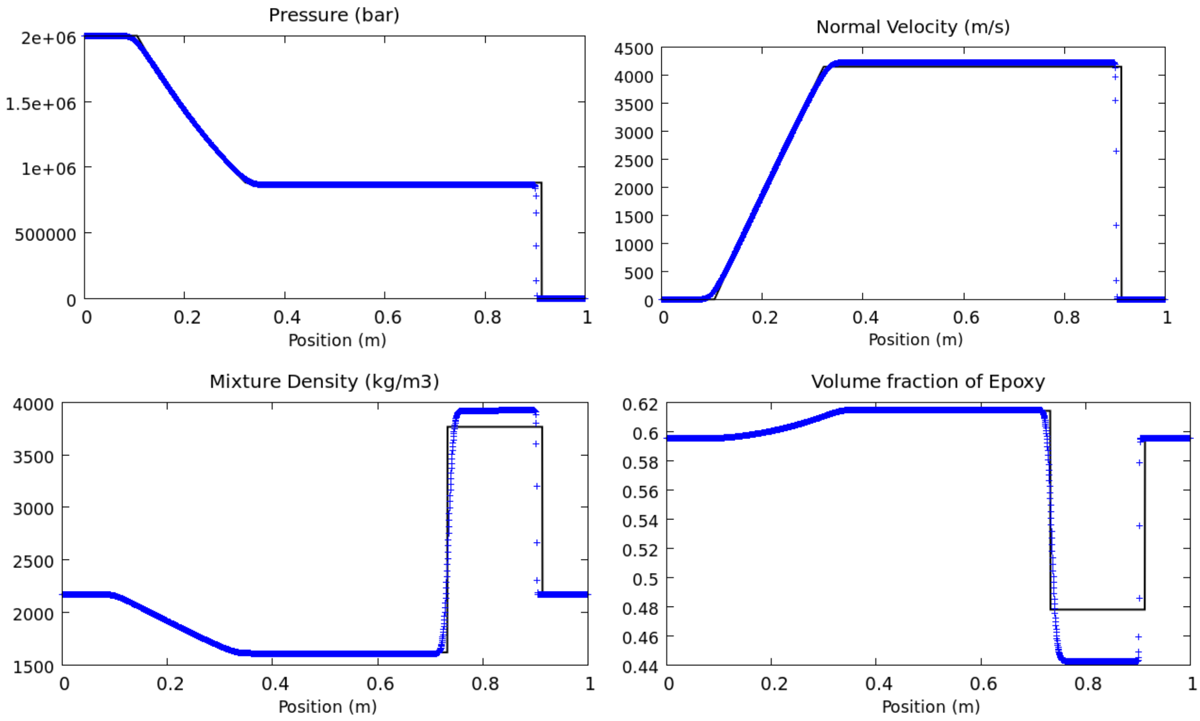

Figure 22: Two-phase shock-tube epoxy-spinel. The numerical solution (symbols – 2000 cells) is compared to the exact solution (solid line). This test shows the difficulties to achieve good convergence with non-conservative equations.

The same difficulties are obviously present in the 3D extensions and in particular in the unstructured solver DALPHADT. However, their resolution is mandatory when dealing with quasi-steady detonation propagation, as the ZND structure cannot be resolved correctly if the shock front is inaccurate (Petitpas et al., 2009, Schoch et al., 2013).

In fact, this shock convergence problem is a consequence of the numerical diffusion of the shock front. The shock front is numerically solved as succession of weak shocks whose thermodynamic path is different from the one obtained for a unique strong shock. It results in a bad energy and entropy partition among the phases. To clarify this, let's examine the numerical shock layer.

To begin, let's first examine the behavior of the numerical scheme on a single phase shock. To do this, the preceding shock tube test case is reconsidered but the spinel is replaced by epoxy so that only epoxy is present in the tube. Doing so the shock wave evolves in a single phase medium. It is thus interesting to compare the thermodynamic path followed by the fluid inside the numerical shock layer to the theoretical Hugoniot curve. This is displayed in Figure 23.

It is clear that the thermodynamic paths are very different. This is caused by the successive weak shocks propagating from a cell to another, which is not equivalent to the thermodynamic transformation given by a single strong shock (Courant and Friedrichs, 1948). Moreover, the successive averaging process of flow variables produces again transformations in disagreement with the single phase Hugoniot curve. However, this numerical problem does not have any consequence on the computation of the shocked state when dealing with single phase flows. As can be seen in Figure 23, the end of the shock layer coincides with the Hugoniot curve. This is a consequence of the conservative character of the Euler equations.

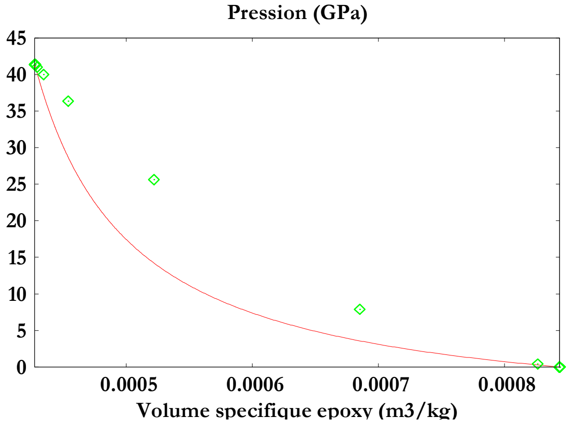

Figure 23: Comparison between the thermodynamic path followed inside the numerical shock layer (symbols) and the theroretical Hugoniot curve (solid lines) in the single phase case. The theoretical and numerical paths are different but the shocked states are the same.

In the two-phase case, the same disagreement with the theoretical Hugoniot curve is observed with however more important issues. The main reason is that, for each weak shock propagating in a cell, the equation of state is modified. Indeed, in the case of mixtures, there is an additional degree of freedom which is the volume fraction, a non-conservative variable. At a given point of the numerical shock layer, it is impossible for this point to belong to the two-phase Hugoniot curve. This fact implies that the volume fraction variable is not computed correctly yielding errors in the mixture equation of state. These various errors add up along the shock layer and contrarily to the single phase case, the final state does not coincide with the theoretical curve. This difficulty is shown in Figure 24 where the thermodynamic path followed in the numerical shock layer is compared to the theoretical Hugoniot curve in the two-phase case epoxy-spinel presented previously.

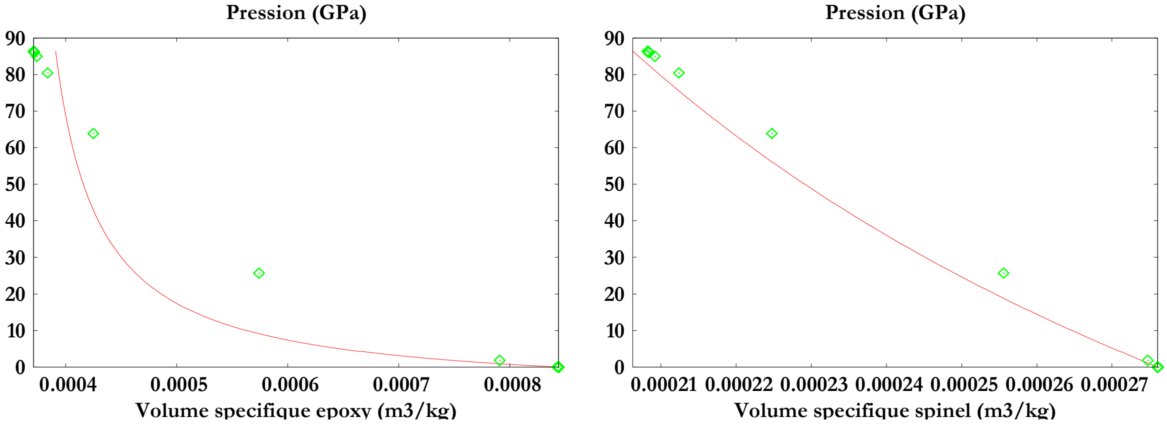

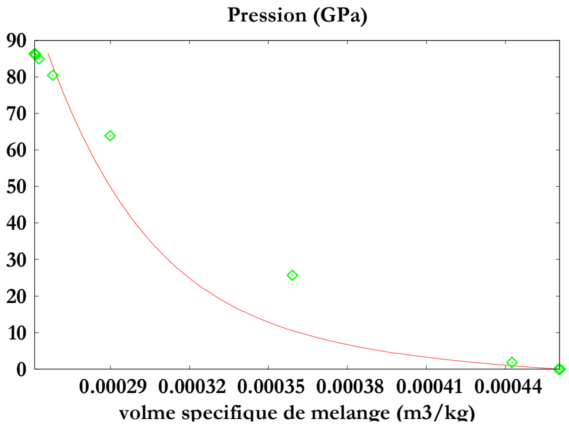

Figure 24: Comparison between the thermodynamic path inside the numerical shock layer (symbols) and the theoretical Hugoniot curves (solid lines) in the two-phase case. The shock wave is the one presented in Figure 22. The thermodynamic path does not follow the Hugoniot curves and in this case, the final state is not computed correctly.

2.2. Modification of the numerical method to preserve convergence at two-phase shocks

2.2.1. Presentation of the 1D method

To force convergence of the solution at shocks artificial heat exchanges have been introduced inside the shock layer in order to properly partition the energies among the phases (Petitpas et al., 2007). This method showed however some drawbacks: implementation difficulties, need to construct the artificial exchange parameter when the initial mixture is modified, multi-D extension impossible on unstructured meshes, impossibility to capture shock wave reflections, etc. All these issues rendered the method impracticable to detonation wave computations in multi-D.

Petitpas et al. (2009) suggested a simpler and more efficient approach. It consists in correcting the thermodynamic path inside the shock layer by enforcing each point of the diffusion zone to belong to the theoretical Hugoniot curve (Figure 25).

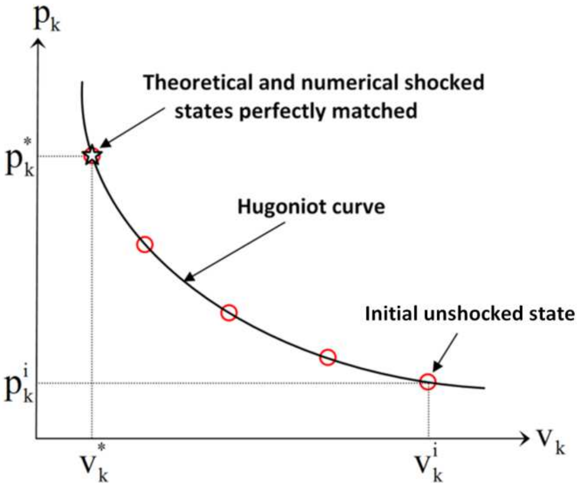

Figure 25: Each point inside the shock layer is enforced to belong to the Hugoniot curve in order to catch the correct shocked state.

In order to perform this correction, it is necessary to keep a trace of the initial unshocked states (e.g. the pressures and specific volumes in front of the shock) $\left(p_k^i, v_k^i\right)$. This is done by adjoining to the system the following set of equations:

$$\begin{cases} \dfrac{d_k p_k^i}{dt} = 0 \\ \dfrac{d_k v_k^i}{dt} = 0 \end{cases}$$

These equations are simple transport equations. They can then be written in conservative form with the help of mass conservation:

$$\begin{cases} \dfrac{\partial \alpha_k \rho_k p_k^i}{\partial t} + \dfrac{\partial \alpha_k \rho_k p_k^i u_k}{\partial x} = 0 \\ \dfrac{\partial \alpha_k \rho_k v_k^i}{\partial t} + \dfrac{\partial \alpha_k \rho_k v_k^i u_k}{\partial x} = 0 \end{cases} \tag{29}$$

Then, during pressure and velocity relaxation stage inside the numerical shock layer, it becomes possible to replace the integral form of the energy equations by imposing each phase stands on its own Hugoniot curve:

$$\forall k, \quad e_k^*\left(p^*, v_k^*\right) - e_k^i\left(p_k^i, v_k^i\right) + \frac{p + p_k^i}{2}\left(v_k^* - v_k^i\right) = 0 \tag{30}$$

Using these new relations in the relaxation stage, it becomes possible to determine the relaxed pressures and specific volumes. In this way, at the end of the relaxation stage, the specific volumes are in perfect agreement with the phases' and mixture's Hugoniot curves at each point inside the diffusion zone.

This correction has to be done inside the shock layer only. A shock indicator has to be used to detect the cells where a shock is present. This particular point is not discussed in Petitpas et al. (2009) even though not obvious.

Let us denote by p_M^n the mixture pressure relaxed at time n, the condition $p_M^{n+1} \geq \left(1+\varepsilon_{sh}\right) p_M^n$ allows to locate the shock, with a parameter ε_{sh} to be defined. Numerical experiments demonstrate that $\varepsilon_{sh} = 0.01$ is a fair choice.

With the help of system (29), the transport of the Hugoniot poles with the flow is ensured through the shock layer. However, through rarefaction waves and in quasi-uniform flows, the poles have to be reset so that the propagation of another shock wave can be treated correctly:

$\left(p_k^i, v_k^i\right) = \left(p_k, v_k\right)$ oustide shock layers.

A difficulty appears when the variables $\left(p_k^i, v_k^i\right)$ are reset in the neighborhood of the numerical shock layer detected by the indicator. Indeed, when the variables are reset, the inherent artificial discontinuity yields an additional source of error in the transport of the variables (29).

If the Hugoniot poles are not transported accurately enough, the solution diverges inside the shock layer affecting the whole shock dynamics (Figures 26 and 27).

It is thus necessary to introduce another indicator covering a wider range than the shock indicator. This second indicator is defined as:

"If at least one neighbor of a given cell verifies the condition $p_M^{n+1} \geq (1+\varepsilon_{res}) p_M^n$, then no reset of (p_k^i, v_k^i) is done inside the cell considered. The parameter ε_{res} is defined as $\varepsilon_{res} = \varepsilon_{sh} / 10$."

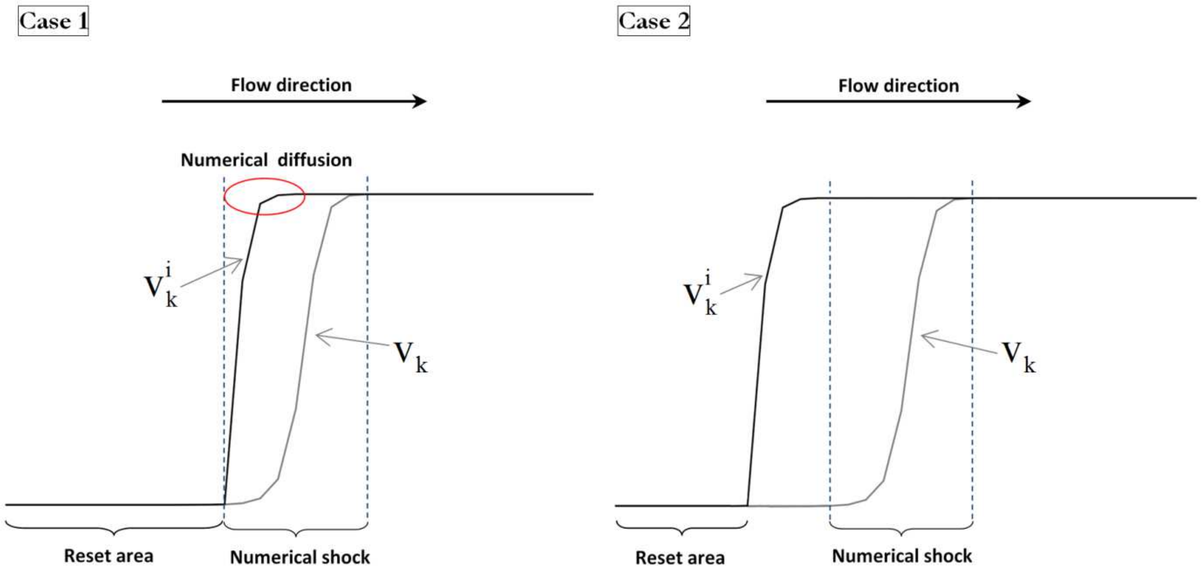

Figure 26: Transport of the specific volume of the Hugoniot pole for a generic phase k in the neighborhood of the numerical shock layer. In Case 1, the reset is done in each cell away from the numerical shock layer. It results in smeared specific volume profiles that enter the shock numerical diffusion zone, yielding loss of the shock Hugoniot correction, as the specific volumes are now incorrect. In Case 2, the reset of v_k^i is not activated in the cells neighbouring the shock. The poles numerical diffusion zone is far enough of the shock layer where correct shock correction is now acheived.

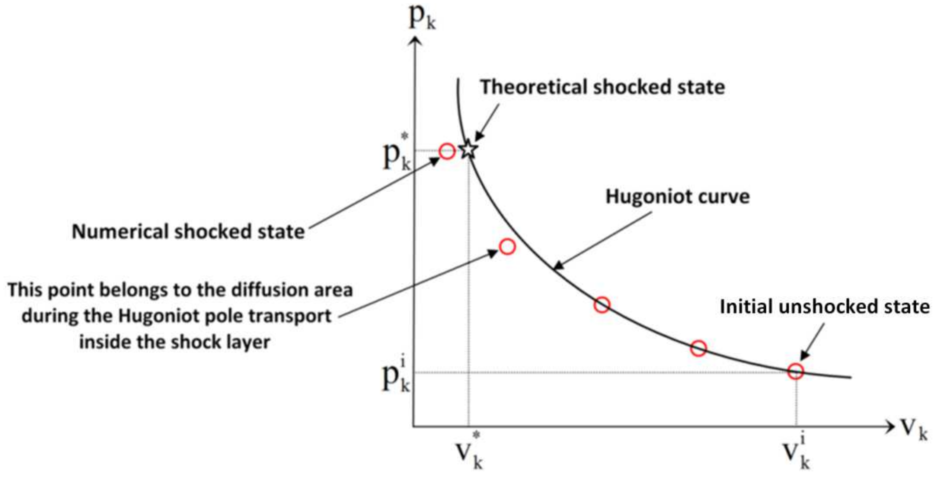

Figure 27: When a numerical diffusion zone appears during the transport of the Hugoniot poles inside the numerical shock layer (Case 1 in Figure 26), the points in this zone do not have the correct poles values (p_k^i, v_k^i). Then, it is not possible to match the Hugoniot curve. Consequently, the final shocked state is badly predicted.

Thus, the method is summarized as follows:

1. **Shock indicator**

   The cells verifying $p_M^{n+1} \geq (1+\varepsilon_{sh}) p_M^n$, with $\varepsilon_{sh} = 0.01$, are corrected during the relaxation stage using relations (30).

2. **Non-reset indicator**

   The (p_k^i, v_k^i) belonging to the cells for which at least one neighbor verifies the condition $p_M^{n+1} \geq (1+\varepsilon_{res}) p_M^n$, with $\varepsilon_{res} = \varepsilon_{sh}/10$ are not reset.

3. **Remaining cells**

   The (p_k^i, v_k^i) belonging to the remaining cells are reset: $(p_k^i, v_k^i) = (p_k, v_k)$.

To illustrate this technique, the test case from Figure 22 is rerun using the above correction. The results are compared to the exact solution in Figure 28, which clearly demonstrates that the method converges.

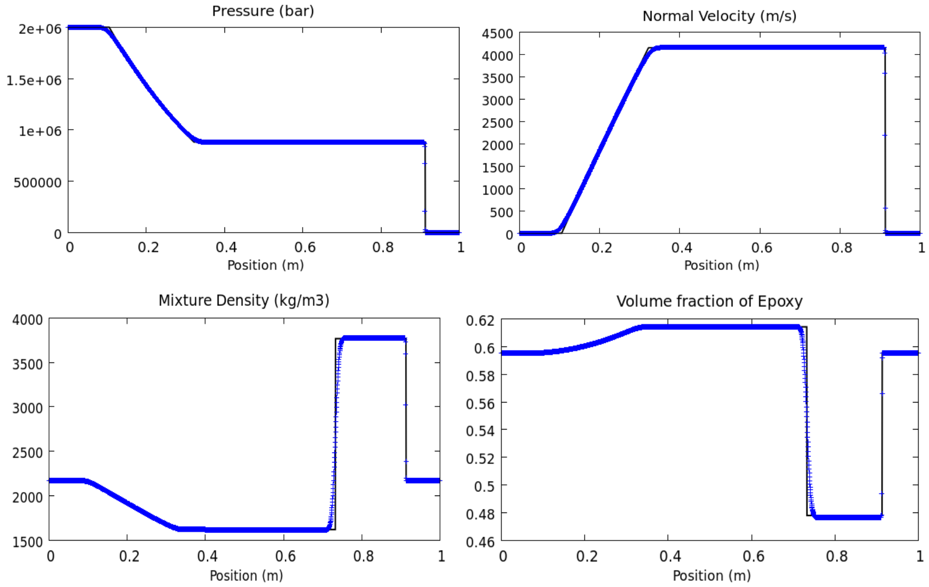

Figure 28: Two-phase shock tube epoxy-spinel with correction for shock convergence. The numerical solution (symbols – 2000 cells) is compared to the exact solution (solid lines). The convergence at the shock is obtained.

Using the same parameters ε_{sh} and ε_{res}, the convergence is checked for several mesh densities (see Figure 29).

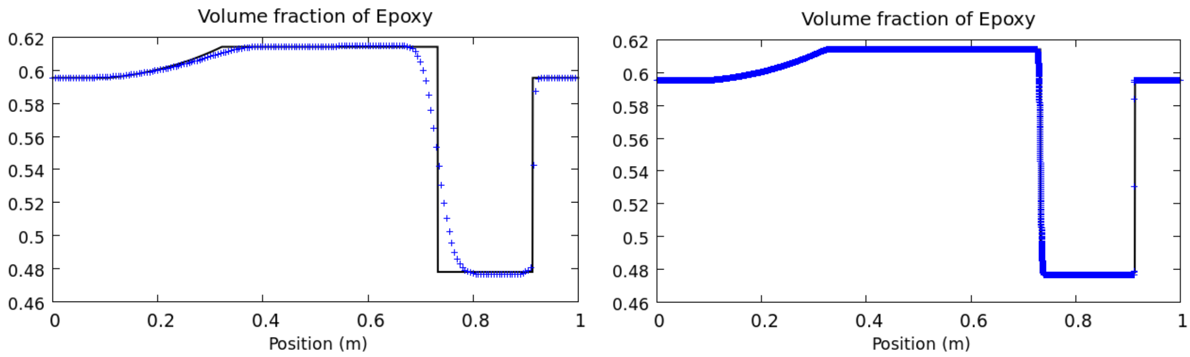

Figure 29: Mesh refinement analysis for the convergence of the volume fraction at the shock. Left: 200 cells, right: 20 000 cells.

2.2.2. Multi-dimensional extension on tetrahedral meshes

The method presented in the last section works nicely on Cartesian meshes. It however needs some modifications on unstructured meshes. To better understand the diffuclty let's have a look at Figure 30.

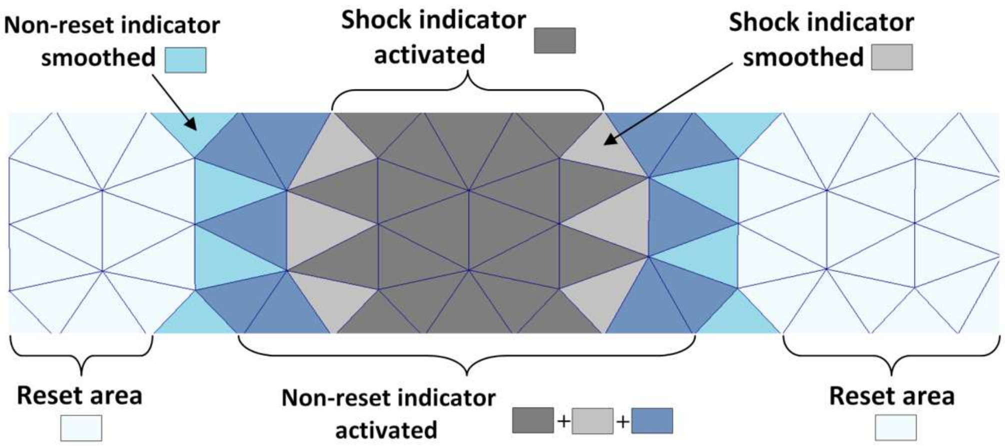

Figure 30: 2D unstructured mesh. Treatment in the neighborhood of a shock.

As previously mentionned, the shock indicator is activated when the condition $p_M^{n+1} \geq (1+\varepsilon_{sh}) p_M^n$ is valid for a given cell.

In the case of an unstructured mesh, the zone inside which the shock indicator is activated has an irregular shape. It does not necessarily catch well the whole shock layer. Let us take as an example a very stretched cell: its barycenter may not have been reached by the shock wave whereas the neighboring cells have been.

To reset the Hugoniot poles properly a smoothing operator is introduced.

This operator is defined as: If a mesh cell c has any neighbor v for which the shock indicator is activated then the shock indicator is also activated in the cell c considered:

If $\exists v$ such that $p_{M,v}^{n+1} \geq (1+\varepsilon_{sh}) p_{M,v}^n$, then $p_{M,c}^{n+1} \geq (1+\varepsilon_{sh}) p_{M,c}^n$ is assumed.

It is possible to repeat the smoothing operator as many times as necessary to artificially obtain a wider zone. In Figure 30, a single smoothing step has been performed once and results in the activation of light gray color cells.

This operator is also applied to the non-reset indicator. This procedure allows obtaining a wider zone inside which the Hugoniot poles are not reset, allowing for their transport on the whole domain covered by the numerical shock layer.
In this figure, we assume that the indicator of non-reset is activated inside the dark gray, light gray and dark blue cells. The smoothing operator adds up an additional layer of cells (light blue) inside which the indicator is activated.

Let us consider a two-phase shock tube composed of epoxy and spinel in the same initial conditions as before. The domain is now 3D (Figure 31) and the mesh is composed of 40000 tetrahedrons.

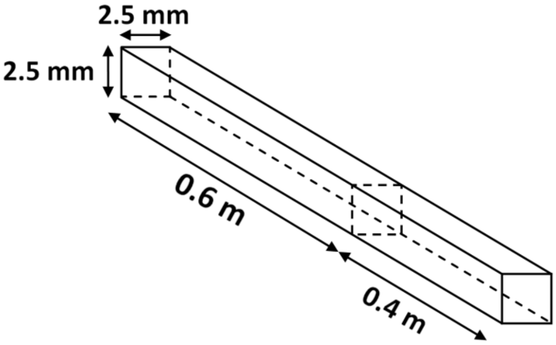

Figure 31: Dimensions du tube à choc 3D.

Several tests are done in order to observe the influence of the smoothing steps number on the correction of the shock. The solutions are projected onto the symmetry axis parallel to the shock tube. We can then compare the 3D results to the 1D results previously obtained. The solutions are presented in Figure 32 at the same physical time ($t = 32\mu s$) :

- In the absence of correction (green curves) we can see again the convergence issue at the shock.

- The correction algorithm used in the 1D test case is reemployed here (pink curve). It corresponds to the case where no smoothing operator is applied (0 smooth). The parameters are identical to the 1D case ($\varepsilon_{sh} = 0.01$ and $\varepsilon_{res} = 0.001$). The convergence at the shock is still inaccurate.

- We now perform tests using 1 to 4 smoothing cycles for the same values of ε_{sh} and ε_{res} . The same number of smoothing steps is applied to both indicators. When the number of cycles increases, the shock state converges to the exact solution.

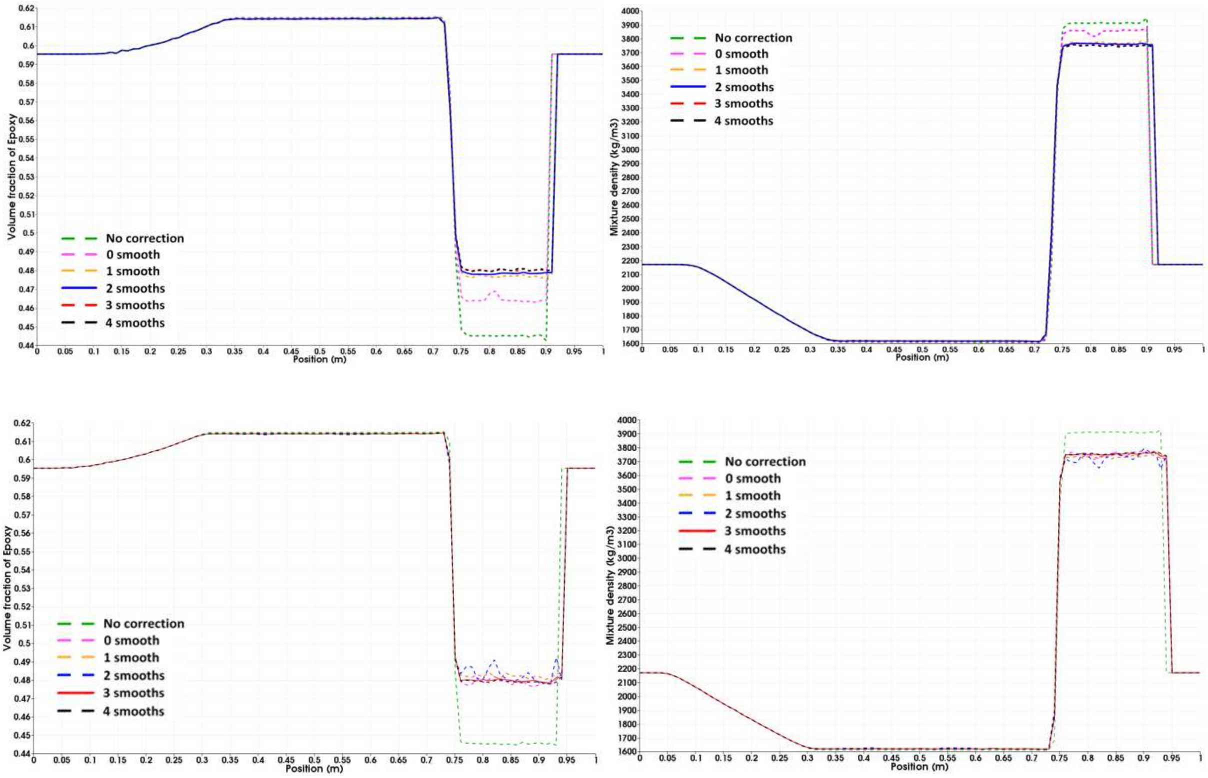

Figure 32: Convergence study as a function of the number of smoothing steps on an unstructured 3D mesh at $t = 32\mu s$ (top: order 1, bottom: order 2 with Venkatakrishnan limiter).

Looking at the results in Figure 32, it seems that the recommended number of smoothing steps is 2 for 1st order and 3 for 2nd order. When 2nd order computations are adressed a larger number of smoothing steps is needed. It is explained by the fact that 2nd order tends to sharpen the shock wave and so to decrease the number of cells detected by the indicator. Given that going from 2 to 3 smoothing steps tends to increase the accuracy of 1st order computations as well, this last value is then recommended for this test case.

The method applied to unstructured grids can be summarized as follows:

1. **Shock indicator**

   The cells satisfying $p_M^{n+1} \geq (1+\varepsilon_{sh}) p_M^n$, with $\varepsilon_{sh} = 0.01$, are corrected in the relaxation step using relations (30).

2. **Shock indicator smoothing**

   If a control volume has at least one of its neighbors for which the shock indicator is activated then it is also activated inside this cell. This procedure is repeated once (2 smoothing steps in total). This increases the total number of cells inside which the correction is done in the pressure relaxation stage.

3. **Non-reset indicator**

   The (p_k^i, v_k^i) belonging to the cells for which at least one of its neighbors satisfies the condition $p_M^{n+1} \geq (1+\varepsilon_{res}) p_M^n$, with $\varepsilon_{res} = 0.001$, are not reset.

4. **Non-reset smoothing**
If a control volume has at least one of its neighbors for which the non-reset indicator is activated then it is also activated inside this cell. As for the shock indicator, this procedure is repeated once. Therefore, the total number of cells where the reset of the Hugoniot poles is not performed is increased.

5. **Remaining cells**
The $\left(p_k^i, v_k^i\right)$ belonging to all remaining cells are reinitialized: $\left(p_k^i, v_k^i\right) = \left(p_k, v_k\right)$.

This method converges under mesh refinement as shown in Figure 33.

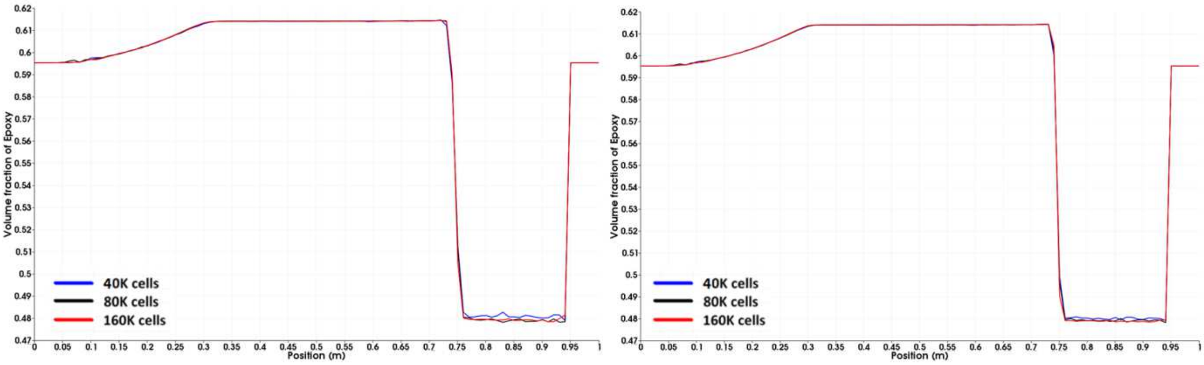

Figure 33: Mesh refinement study for the volume fraction of Epoxy. The meshes presented here contain 20 000, 80 000 and 160 000 cells. Left: 1st order and right: 2nd order (Venkatakrishnan limiter) at time $t = 32\mu s$

2.2.3. Tests on reflected shock waves

So far, the method has been tested for a single free shock wave. In the following, we study the robustness of our approach on a more complex test case: when a shock wave reflects a solid wall. To do so, we conduct the same shock tube problem as previously mentioned but replace the boundary condition at the low-pressure side by a solid wall. The final simulation time is also increased to $t = 70\mu s$ in order to make the shock reach the wall and reflect.

In order to compare the numerical solution, the exact Riemann solver based on the Kapila et al. (2001) model and Saurel et al. (2007) Hogoniot relations is used. This reference solution for a reflected shock is obtained in two steps as shown in Figure 34:

1. Solution to the Riemann problem with the initial condition described earlier for the left and right states. This step gives the star states at the right side of the contact discontinuity (post-shock).
2. Solution of the Riemann problem with left and right states obtained from the first step. The right state velocity has a reversed sign in order to simulate the presence of a wall.

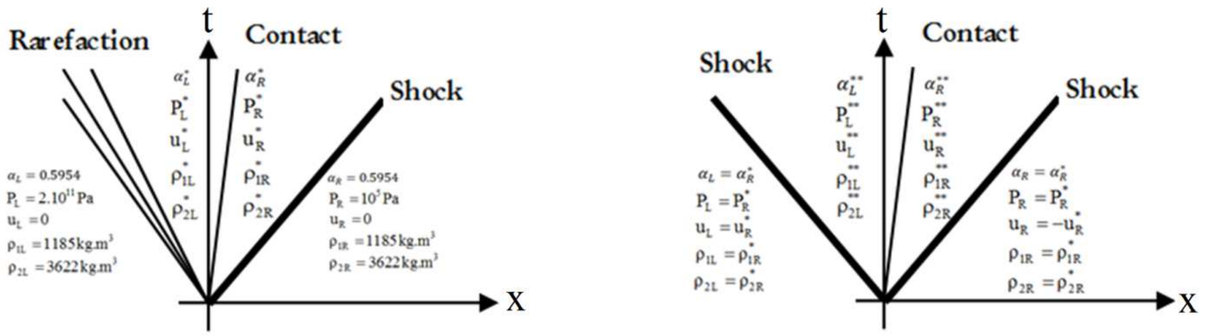

Figure 34: Two-step resolution for the reference solution determination of a reflected shock at a solid wall.

The star states of both problems are summarized in Table 2.

$\alpha_R^* = 0.478$	$\alpha_L^{**} = 0.4646$
$P_R^* = 8.81*10^{11}$ Pa	$P_L^{**} = 2.85*10^{11}$ Pa
$u_R^* = 4.15*10^3$ m.s^{-1}	$u_L^{**} = 0$ m.s^{-1}
$\rho_{1R}^* = 2.56*10^3$ kg.m^{-3}	$\rho_{1L}^{**} = 3.93*10^3$ kg.m^{-3}
$\rho_{2R}^* = 4.87*10^3$ kg.m^{-3}	$\rho_{2L}^{**} = 7.09*10^3$ kg.m^{-3}
$\rho_{MIX,R}^* = 3.77*10^3$ kg.m^{-3}	$\rho_{MIX,L}^{**} = 5.62*10^3$ kg.m^{-3}

Table 2: Exact solutions obtained from the exact Riemann solver based on Kapila et al. (2001) model.

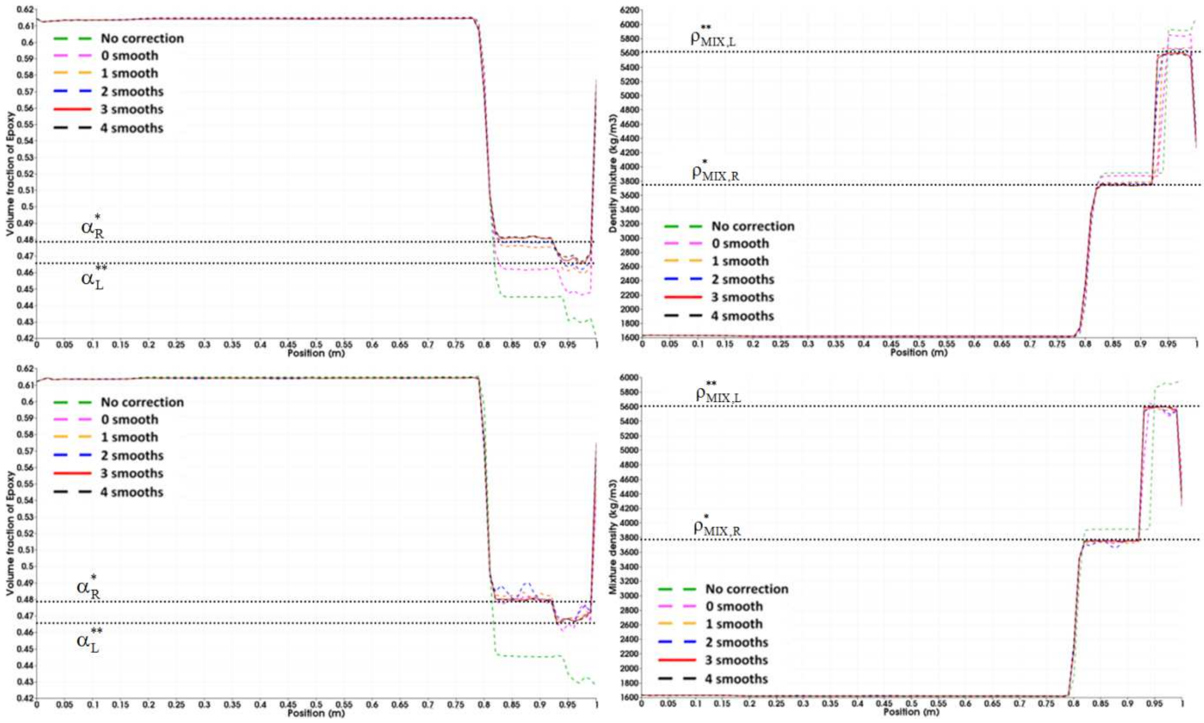

Figure 35: Convergence of the method for a reflected shock wave on a 3D unstructured mesh at $t = 49\mu s$ (top: 1st order, bottom: 2nd order with Venkatakrishnan limiter).

As done in the case of a single shock wave, a convergence study as a function of the number of smoothing steps is presented in Figure 35. The volume fraction of Epoxy has two post-shock states, one before and one after relfection to the wall. These two locally constant states are in perfect agreement with the results obtained with the exact Riemann solver based on the model equations of Kapila ($\alpha_R^* \, and \, \alpha_L^{**}$ from Table 2). The mixture density is also naturally very well predicted. It is important to remark that if no correction is given then the resulting values are very different from the exact ones.

A mesh refinement study is finally conducted and presented in Figure 36 after the wall reflection at time $t = 70\mu s$. Three smoothing steps have been used. It can be seen that when the number of mesh elements increases the volume fraction of Epoxy tends to the exact value of Table 2.

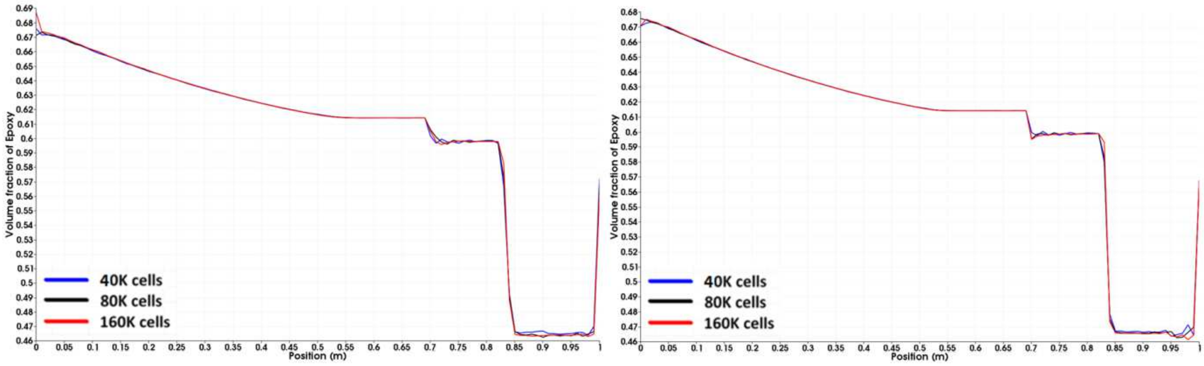

Figure 36: Refinement study for the reflected shock on a 3D unstructured mesh composed of 20 000, 80 000 and 160 000 cells. Left: 1st order and right: 2nd order (Venkatakrishnan limiter) at time $t = 70\mu s$

2.3. Conclusion

A numerical technique consisting in enforcing the correct energy partition at a discrete level in agreement with the multiphase shock relations has been built and extended to 3D unstructured meshes. In particular, a robust and efficient method wad developed to detect shock waves.

Chapitre 3

Extension du solveur de Riemann de type HLLC au cas multiphasique

3.1. Introduction

In Abgrall and Saurel (2003) the two-phase computational cell is divided in two sub volumes, each one corresponding to a given phase (Figure 37). At each cell boundary and for each type of contact, the Riemann problem for the Euler equations is solved.

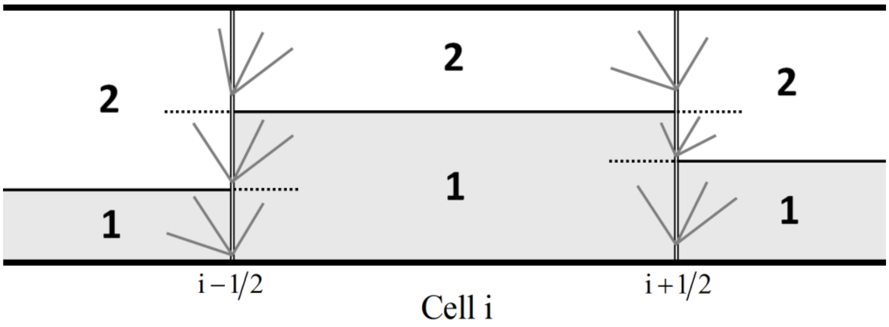

Figure 37: Stratified two-phase flow topology. At each cell boundary and for each type of contact, the Riemann problem for the Euler equations is solved.

These solutions are then averaged in each sub volume and provide a set of discrete equations that correspond to some kind of two-phase Godunov method (Discrete Equations Method – DEM – see Section 1.3.1).

In the continuous limit, when both space and time steps tend to zero, the Saurel et al. (2003) symmetric variant of the BN model is recovered:

Phase1

$$\frac{\partial \alpha_1}{\partial t}+u_I\frac{\partial \alpha_1}{\partial x}=\mu(P_1-P_2)$$

$$\frac{\partial \alpha_1\rho_1}{\partial t}+\frac{\partial \alpha_1\rho_1u_1}{\partial x}=0$$

$$\frac{\partial \alpha_1\rho_1u_1}{\partial t}+\frac{\partial \alpha_1\rho_1u_1{}^2+\alpha_1P_1}{\partial x}=P_I\frac{\partial \alpha_1}{\partial x}+\lambda(u_2-u_1)$$

$$\frac{\partial \alpha_1\rho_1E_1}{\partial t}+\frac{\partial \alpha_1(\rho_1E_1+P_1)u_1}{\partial x}=P_Iu_I\frac{\partial \alpha_1}{\partial x}+\lambda\overline{u_I}(u_2-u_1)-\mu\overline{P_I}(P_1-P_2)$$

Phase2

$$\frac{\partial \alpha_2\rho_2}{\partial t}+\frac{\partial \alpha_2\rho_2u_2}{\partial x}=0$$

$$\frac{\partial \alpha_2\rho_2u_2}{\partial t}+\frac{\partial \alpha_2\rho_2u_2{}^2+\alpha_2P_2}{\partial x}=P_I\frac{\partial \alpha_2}{\partial x}-\lambda(u_2-u_1)$$

$$\frac{\partial \alpha_2\rho_2E_2}{\partial t}+\frac{\partial \alpha_2(\rho_2E_2+P_2)u_2}{\partial x}=P_Iu_I\frac{\partial \alpha_2}{\partial x}-\lambda\overline{u_I}(u_2-u_1)+\mu\overline{P_I}(P_1-P_2)$$

This model is the starting point of the new two-phase method (Chapter 1).

The multiphase extension of the two-phase HLLC type Riemann solver requires the knowledge of a continuous multiphase model. In this aim, the continuous limit of the multiphase discrete equations obtained in the frame of the DEM has to be considered.

In the case of a N-phase mixture (with N an arbitrary integer number) and in the frame of the DEM, the computational cell is divided in N sub-volumes, each one corresponding to a given phase. A 3-phase flow example is given in Figure 38.

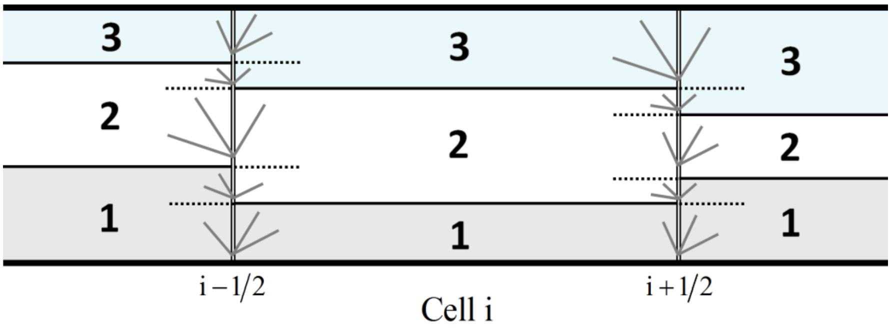

Figure 38: Example of a stratified 3-phase flow topology. In the same way as the two-phase case, the Riemann problem for the Euler equations is solved at each cell boundary and for each type of contact.

In the same way as the two-phase case, a set of discrete equations is obtained. However, the search for the continuous limit of this N-phase discrete system is tedious. Indeed, when both space and time steps tend to zero, the continuous form of the non-conservative terms is complex.

The following semi-discrete N-phase model is thus considered, $\forall k\in\{1,\ldots,N\}$:

$$\begin{aligned}
&\frac{\partial \alpha_k}{\partial t}+\frac{\sum_{l,m}\left(h\left[\chi_k^*\right]u^*\right)_{lm,i-1/2}+\sum_{l,m}\left(h\left[\chi_k^*\right]u^*\right)_{lm,i+1/2}}{\Delta x}=0\\
&\frac{\partial \alpha_k\rho_k}{\partial t}+\frac{\partial \alpha_k\rho_k u_k}{\partial x}=0\\
&\frac{\partial \alpha_k\rho_k u_k}{\partial t}+\frac{\partial \alpha_k\rho_k u_k{}^2+\alpha_k P_k}{\partial x}=\frac{\sum_{l,m}\left(h\left[\chi_k^*\right]P^*\right)_{lm,i-1/2}+\sum_{l,m}\left(h\left[\chi_k^*\right]P^*\right)_{lm,i+1/2}}{\Delta x}\\
&\frac{\partial \alpha_k\rho_k E_k}{\partial t}+\frac{\partial \alpha_k\left(\rho_k E_k+P_k\right)u_k}{\partial x}=\frac{\sum_{l,m}\left(h\left[\chi_k^*\right]P^*u^*\right)_{lm,i-1/2}+\sum_{l,m}\left(h\left[\chi_k^*\right]P^*u^*\right)_{lm,i+1/2}}{\Delta x},
\end{aligned}\tag{31}$$

with the temporal terms and the Eulerian fluxes written under their continuous form. Moreover, we have to keep in mind that the space step is very small: $\Delta x=\varepsilon<<1$. Let's focus our attention on non-conservative terms that pose the main difficulties for numerical approximation.

Non-conservative terms

For a given cell, non-conservative terms can be expressed with the following general form,

$$\frac{\sum_{l,m}\left(h\left[\chi_k^*\right]F^{Lag,*}\right)_{lm,i-1/2}+\sum_{l,m}\left(h\left[\chi_k^*\right]F^{Lag,*}\right)_{lm,i+1/2}}{\Delta x}$$

where :

- $(l,m)\in\{1,\dots,N\}\times\{1,\dots,N\}$ represent the various possible contacts among the phases,
- $l\neq m$
- h_{lm} is the height of the flow channel representing the contact 'l-m' on a given cell boundary. Determination of the contact surfaces at the cell boundaries for an arbitrary number of fluids was proposed by Chinnayya et al. (2004) (Appendix 3.A).
- $\left[\chi_k^*\right]_{lm}$ is the phase function jump following the x direction through the contact 'l-m'. More exactly, we have:

  $$\left[\chi_k^*\right]_{lm}=\chi_{k,m}-\chi_{k,l},\tag{32}$$

  where for example $\chi_{k,m}=\begin{cases}1 \text{ if } k=m\\ 0 \text{ if } k\neq m\end{cases}$

  Let us note that $\left[\chi_k^*\right]_{lm}\neq 0$ if the contact 'l-m' goes into the cell considered. In that case, $\left[\chi_k^*\right]_{lm}=\begin{cases}1 \text{ if } k=m\\ -1 \text{ if } k=l\end{cases}$
- $F_{lm}^{Lag,*}=\left(-u_{lm}^* \quad 0 \quad P_{lm}^* \quad P_{lm}^*u_{lm}^*\right)^T$ is the Lagrangian flux solution of the Riemann problem for the Euler equations and for the contact 'l-m' on a given cell boundary.

System (31) can be rewritten as follows, $\forall k\in\{1,\dots,N\}$,

$$\frac{\partial U_k}{\partial t}+\frac{\partial F_k}{\partial x}=\frac{\sum_{l,m}\left(h\left[\chi_k^*\right]F^{*,lag}\right)_{lm,i-1/2}+\sum_{l,m}\left(h\left[\chi_k^*\right]F^{*,lag}\right)_{lm,i+1/2}}{\Delta x},\tag{33}$$

with,

$$U_k = \begin{pmatrix} \alpha_k \\ \alpha_k\rho_k \\ \alpha_k\rho_k u_k \\ \alpha_k\rho_k E_k \end{pmatrix},\ F_k = \begin{pmatrix} 0 \\ \alpha_k\rho_k u_k \\ \alpha_k\left(\rho_k u_k{}^2 + P_k\right) \\ \alpha_k\left(\rho_k E_k + P_k\right)u_k \end{pmatrix}.$$

We now adress HLLC type Riemann solver builing for a given phase k.

3.2. Multiphase Riemann solver

3.2.1. Local conservative formulation

In this section, the Riemann problem only is considered on a given cell boundary. Keeping in mind that $\Delta x = \varepsilon << 1$, system (33) can be expressed locally under the following form:

$$\frac{\partial U_k}{\partial t} + \frac{\partial F_k}{\partial x} = \frac{\sum\limits_{l,m}\left(h\left[\chi_k^*\right]F^{*,lag}\right)_{lm}}{\Delta x}$$

Thanks to the definition (32), this expression can be rewritten as,

$$\frac{\partial U_k}{\partial t} + \frac{\partial F_k}{\partial x} = \sum_{l,m}\frac{h_{lm}F_{lm}^{*,lag}\left(\chi_{k,m} - \chi_{k,l}\right)}{\Delta x}.$$

The velocity u_{lm}^* and the pressure P_{lm}^* present in non-conservative terms are solutions of the Riemann problem of the Euler equations and for the contact ‘l-m’. As the Riemann problem solution depends only of the initial left and right states, variables u_{lm}^* and P_{lm}^* are locally constant during a time step at a given cell boundary and for a given contact ‘l-m’. They are computed by an appropriate Riemann solver of the Euler equations (exact or approximate) with correct initial states as inputs.

Moreover, h_{lm} is locally constant too and $\Delta x = \varepsilon << 1$. We can thus write:

$$\frac{\partial U_k}{\partial t} + \frac{\partial F_k}{\partial x} = \sum_{l,m} h_{lm}F_{lm}^{*,lag}\frac{\partial\left(\chi_k\right)_{lm}}{\partial x}$$

The term $h_{lm}F_{lm}^{*,lag}$ being a local constant at a given cell boundary the previous system becomes,

$$\frac{\partial U_k}{\partial t} + \frac{\partial F_k}{\partial x} - \sum_{l,m}\frac{\partial\left(hF^{*,lag}\chi_k\right)_{lm}}{\partial x} = 0$$

$$\Leftrightarrow \frac{\partial U_k}{\partial t} + \frac{\partial F_k}{\partial x} - \frac{\partial\sum\limits_{l,m}\left(hF^{*,lag}\chi_k\right)_{lm}}{\partial x} = 0$$

We thus obtain a locally conservative system:

$$\frac{\partial U_k}{\partial t} + \frac{\partial\left(F_k - \sum\limits_{l,m}\left(hF^{*,lag}\chi_k\right)_{lm}\right)}{\partial x} = 0 \tag{34}$$

3.2.2. Phase k wave pattern

The variables u_{lm}^* and P_{lm}^* being local constants, another important simplification appears. The Riemann problem for a given phase is decoupled to the one of the other phases. Thus, for a given phase k, the Riemann problem is based on system (34) and on its own wave pattern composed of $(N+2)$ waves. The various waves speeds are computed as follows:

- The left- and right-facing wave speeds $S_{L,k}$ and $S_{R,k}$ are for example determined by the Davis (1988) estimates:

  $$S_{R,k} = \mathrm{Max}(u_{L,k} + c_{L,k}, u_{R,k} + c_{R,k}),$$
  $$S_{L,k} = \mathrm{Min}(u_{L,k} - c_{L,k}, u_{R,k} - c_{R,k}).$$

- With the help of these wave speeds, the intermediate contact wave is estimated under HLL approximation as:

  $$S_{M,k} = \frac{\alpha_{R,k}\left(\rho u^2 + P\right)_{R,k} - \alpha_{L,k}\left(\rho u^2 + P\right)_{L,k} + S_{L,k}\left(\alpha\rho u\right)_{L,k} - S_{R,k}\left(\alpha\rho u\right)_{R,k} - \left[\sum_{l,m}\left(hP^{*,lag}\chi_k\right)_{lm}\right]_R + \left[\sum_{l,m}\left(hP^{*,lag}\chi_k\right)_{lm}\right]_L}{\left(\alpha\rho u\right)_{R,k} - \left(\alpha\rho u\right)_{L,k} + S_{L,k}\left(\alpha\rho\right)_{L,k} - S_{R,k}\left(\alpha\rho\right)_{R,k}}$$

  where pressures P^*_{lm} and heights h_{lm} are already computed and local constants.
  With the help of (32), the discrete part of the previous expressions read,

  $$\left[\sum_{l,m}\left(hP^{*,lag}\chi_k\right)_{lm}\right]_L - \left[\sum_{l,m}\left(hP^{*,lag}\chi_k\right)_{lm}\right]_R = \sum_{l,m}\left[\left(hP^{*,lag}\chi_k\right)_{lm}\right]_L - \sum_{l,m}\left[\left(hP^{*,lag}\chi_k\right)_{lm}\right]_R$$
  $$= \sum_{l,m}\left(hP^{*,lag}\left(\chi_{k,l} - \chi_{k,m}\right)\right)_{lm} = -\sum_{l,m}\left(hP^{*,lag}\left[\chi_k^*\right]\right)_{lm}$$

  $S_{M,k}$ thus reads:

  $$S_{M,k} = \frac{\alpha_{R,k}\left(\rho u^2 + P\right)_{R,k} - \alpha_{L,k}\left(\rho u^2 + P\right)_{L,k} + S_{L,k}\left(\alpha\rho u\right)_{L,k} - S_{R,k}\left(\alpha\rho u\right)_{R,k} - \sum_{l,m} h_{lm} P^{*,lag}_{lm}\left[\chi_k^*\right]_{lm}}{\left(\alpha\rho u\right)_{R,k} - \left(\alpha\rho u\right)_{L,k} + S_{L,k}\left(\alpha\rho\right)_{L,k} - S_{R,k}\left(\alpha\rho\right)_{R,k}}$$

- $(N-1)$ interfacial wave speeds $u^{(q)}_{I,k}$, $q \in \{1,\ldots,N-1\}$, represent the different contacts between the phase k and the other ones.

  For example, let us consider the case $N = 4$ and the Riemann solver associated with the phase 1. On a given cell boundary, existing interfacial contacts may be contacts '1-2', '3-1' and '1-4'. In this case, we could denote by:
  $u^{(1)}_{I,1} = u^*_{12}$, $u^{(2)}_{I,1} = u^*_{31}$ et $u^{(3)}_{I,1} = u^*_{14}$.

Thus, there are $(N+1)$ intermediate states per phase and on each cell boundary. In order to build a simple algorithm, it's necessary to rank in ascending order all the N intermediate wave speeds $\{S_{M,k}, u^{(q)}_{I,k}\}$, $q \in \{1,\ldots,N-1\}$. To do that, we use a quicksort algorithm.

Let us define the intermediate waves by $\sigma^{(j)}_k$, $j \in \{1,\ldots,N\}$ and check:

$$\sigma^{(1)}_k < \ldots < \sigma^{(j-1)}_k < \sigma^{(j)}_k < \sigma^{(j+1)}_k < \ldots < \sigma^{(N)}_k.$$

It's important to detect the index j_M verifying $\sigma^{(j_M)}_k = S_{M,k}$.

The phase-k wave pattern is shown in Figure 39.

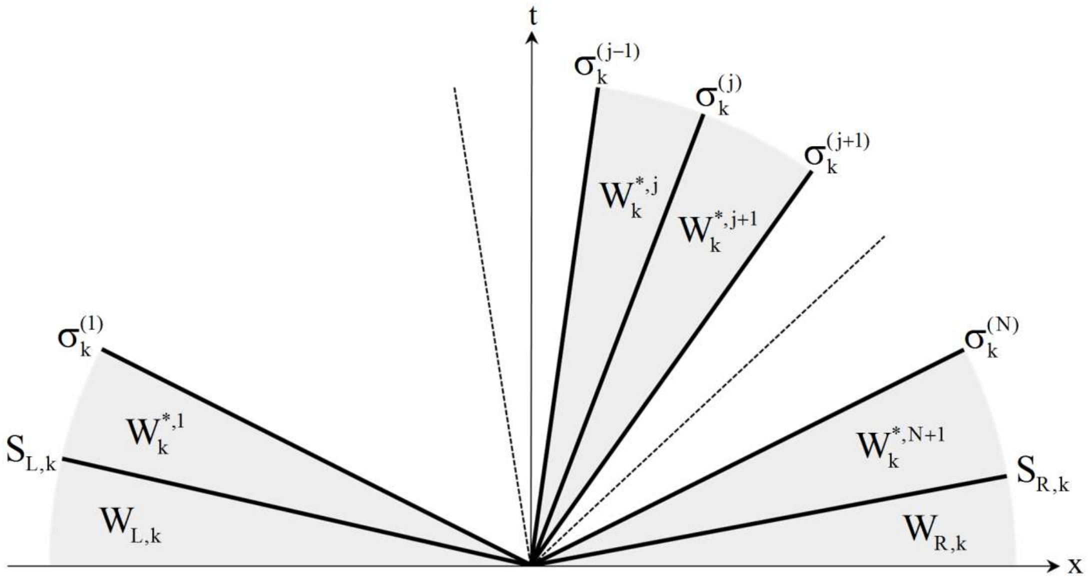

Figure 39: Schematic representation of the Riemann problem for a given phase k in the HLLC frame. 'W' represents the set of variables of the N-phase model.

In Figure 39, W_k denotes the vector of primitive variables of a given phase:

$W_k = (\alpha_k, \quad \rho_k, \quad u_k, \quad P_k)^T$.

$W_{L,k}$ and $W_{R,k}$ are respectively the left and right initial states, known at each time step. The Rankine-Hugoniot relations across the various waves link the initial data to the intermediate states $W_k^{*,z}$, $\forall z \in \{1, \ldots, N+1\}$.

3.2.3. Comment on Rankine-Hugoniot relations

Let us consider a given wave of speed D, separating the unshocked state '0' and the shocked one 'S'. Across this wave, the Rankine-Hugoniot relations of system (5) read :

$$F_k^S - \sum_{l,m} \left(hF^{*,lag}\chi_k\right)_{lm}^S - DU_k^S = F_k^0 - \sum_{l,m} \left(hF^{*,lag}\chi_k\right)_{lm}^0 - DU_k^0 .$$

$$\Leftrightarrow F_k^S = F_k^0 + D\left(U_k^S - U_k^0\right) + \sum_{l,m} \left(hF^{*,lag}\left(\chi_k^S - \chi_k^0\right)\right)_{lm}$$

$$\Leftrightarrow F_k^S = F_k^0 + D\left(U_k^S - U_k^0\right) + \sum_{l,m} \left(hF^{*,lag}\left[\chi_k^*\right]\right)_{lm}$$

Let us note that $\left[\chi_k^*\right]_{lm} \neq 0$ only through the interface separating the phase l from the phase m. In other words, we only have $\left[\chi_k^*\right]_{lm} \neq 0$ through the wave of speed u_{lm}^*.

Thus, the Rankine-Hugoniot relations across this wave $\left(D = u_{lm}^*\right)$ reduce to,

$$F_k^S = F_k^0 + D\left(U_k^S - U_k^0\right) + \left(hF^{*,lag}\left[\chi_k^*\right]\right)_{lm} .$$

In the following, the term $\left(hF^{*,lag}\left[\chi_k^*\right]\right)_{lm}$ will be called the discrete correction linked to the wave of speed u_{lm}^*.

Moreover, if $D \in \{S_{L,k}, S_{M,k}, S_{R,k}\}$, the discrete term $\sum_{l,m}\left(hF^{*,lag}\left[\chi_k^*\right]\right)_{lm}$ disappears. For example, if $D = S_{M,k}$, we recognize the conventional RH relation:

$$F_k^S = F_k^0 + S_{M,k}\left(U_k^S - U_k^0\right)$$

In that respect, it is important to know the index j_M verifying $\sigma_k^{(j_M)} = S_{M,k}$.

3.2.4. Determination of the Riemann problem solution state – Algorithm

1. If $S_{L,k} \geq 0$ or $S_{R,k} \leq 0$, solutions are obvious and are respectively the states $W_{L,k}$ or $W_{R,k}$.

Otherwise, determining the index j_{Sol} of the Riemann problem solution state is easy, as all the N intermediate wave speeds are ranked. This index respects the following condition :

$\sigma_k^{(j_{sol}-1)} \leq 0 < \sigma_k^{(j_{sol})}$, $j \in \{1, ..., N+1\}$, with the convention $\sigma_k^{(0)} \equiv S_{L,k}$ and $\sigma_k^{(N+1)} \equiv S_{R,k}$.

Two instances have to be considered:

- $j_{Sol} \leq j_M$. In this case the contact discontinuity of that phase faces to right. The method is described at step 2.
- $j_{Sol} > j_M$. In this case the contact discontinuity of that phase faces to left. The method is described at step 4.

2. Determine the state $W_k^{*,1}$. To do this we use the Rankine-Hugoniot relations through the left-facing wave speed $S_{L,k}$:

   $$F_k^{*,1} = F_{L,k} + S_{L,k}\left(U_k^{*,1} - U_{L,k}\right).$$

   We thus obtain the following results :

   $$\alpha_k^{*,1} = \alpha_{L,k},$$

   $$\rho_k^{*,1} = \rho_{L,k}\frac{u_{L,k} - S_{L,k}}{S_{M,k} - S_{L,k}},$$

   $$u_k^{*,1} = S_{M,k},$$

   $$P_k^{*,1} = P_{L,k} + \rho_{L,k}\left(u_{L,k} - S_{L,k}\right)\left(u_{L,k} - S_{M,k}\right),$$

   $$E_k^{*,1} = E_{L,k} + \frac{(Pu)_{L,k} - P_k^{*,1}S_{M,k}}{\rho_{L,k}\left(u_{L,k} - S_{L,k}\right)}.$$

3. If $j_{Sol} \neq 1$ then set $j = 1$ and continue by the procedure that follows.

   The Rankine-Hugoniot relations through the wave of speed $\sigma_k^{(j)}$ are used in order to determine the state $W_k^{*,j+1}$:

   $$F_k^{*,j+1} = F_k^{*,j} + \sigma_k^{(j)}\left(U_k^{*,j+1} - U_k^{*,j}\right) + \psi_k^{(j)},$$

   with $\psi_k^{(j)}$ the discrete correction linked to the wave of speed $\sigma_k^{(j)}$. Obvisously, $\psi_k^{(j_M)} = 0$.

   In this context, we get :

   $$\alpha_k^{*,j+1} = \alpha_k^{*,j} + \left(h\left[X_k^*\right]\right)_{(j)}$$

$$\rho_k^{*,j+1} = \frac{\alpha_k^{*,j}}{\alpha_k^{*,j+1}} \rho_k^{*,j}$$

$$u_k^{*,j+1} = S_{M,k}$$

$$P_k^{*,j+1} = \frac{\alpha_k^{*,j}}{\alpha_k^{*,j+1}} P_k^{*,j} + \frac{\left(h\left[X_k^*\right]P^*\right)_{(j)}}{\alpha_k^{*,j+1}}$$

$$E_k^{*,j+1} = E_k^{*,j} + \frac{\left(\alpha_k^{*,j}P_k^{*,j} - \alpha_k^{*,j+1}P_k^{*,j+1}\right)S_{M,k} + \left(h\left[X_k\right]P^*u^*\right)_{(j)}}{\alpha_k^{*,j}\rho_k^{*,j}\left(S_{M,k} - \sigma_k^{(j)}\right)},$$

where the index (j) recalls the link between the discrete correction and the wave of speed $\sigma_k^{(j)}$.

Then increment j as $j = j + 1$.

This step is repeated as long as $j < j_M$ or $j \neq j_{sol}$.

4. At this stage, if j_{sol} has not been reached, determine the state $W_k^{*,N+1}$ thanks to the RH relations through the wave of speed $S_{R,k}$:

   $$F_k^{*,N+1} = F_{R,k} + S_{R,k}\left(U_k^{*,N+1} - U_{R,k}\right).$$

   The following results are obtained:

   $$\alpha_k^{*,N+1} = \alpha_{R,k},$$

   $$\rho_k^{*,N+1} = \rho_{R,k}\frac{u_{R,k} - S_{R,k}}{S_{M,k} - S_{R,k}},$$

   $$u_k^{*,N+1} = S_{M,k},$$

   $$P_k^{*,N+1} = P_{R,k} + \rho_{R,k}\left(u_{R,k} - S_{R,k}\right)\left(u_{R,k} - S_{M,k}\right),$$

   $$E_k^{*,N+1} = E_{R,k} + \frac{(Pu)_{R,k} - P_k^{*,N+1}S_{M,k}}{\rho_{R,k}\left(u_{R,k} - S_{R,k}\right)}.$$

5. If $j_{Sol} \neq N+1$, initialize $j = N$.

   The Rankine-Hugoniot relations through the wave of speed $\sigma_k^{(j)}$ are used in order to determine the state $W_k^{*,j}$:

   $$F_k^{*,j} = F_k^{*,j+1} + \sigma_k^{(j)}\left(U_k^{*,j} - U_k^{*,j+1}\right) - \psi_k^{(j)}.$$

   In this context, we obtain :

   $$\alpha_k^{*,j} = \alpha_k^{*,j+1} - \left(h\left[X_k^*\right]\right)_{(j)}$$

   $$\rho_k^{*,j} = \frac{\alpha_k^{*,j+1}}{\alpha_k^{*,j}} \rho_k^{*,j+1}$$

   $$u_k^{*,j} = S_{M,k}$$

$$P_k^{*,j} = \frac{\alpha_k^{*,j+1}}{\alpha_k^{*,j}} P_k^{*,j+1} - \frac{\left(h\left[X_k^*\right]P^*\right)_{(j)}}{\alpha_k^{*,j}}$$

$$E_k^{*,j} = E_k^{*,j+1} + \frac{\left(\alpha_k^{*,j+1}P_k^{*,j+1} - \alpha_k^{*,j}P_k^{*,j}\right)S_{M,k} - \left(h\left[X_k\right]P^*u^*\right)_{(j)}}{\alpha_k^{*,j}\rho_k^{*,j}\left(S_{M,k} - \sigma_k^{(j)}\right)}$$

Then increment $j = j - 1$.

This step is repeated as far as $j > j_M$ or $j \neq j_{sol}$.

We now have in hands the conservative variable vector of the Riemann problem solution state,

$$U_k^{*,j_{sol}} = \begin{pmatrix} \alpha_k^{*,j_{sol}} \\ (\alpha\rho)_k^{*,j_{sol}} \\ (\alpha\rho)_k^{*,j_{sol}} S_{M,k} \\ (\alpha\rho)_k^{*,j_{sol}} E_k^{*,j_{sol}} \end{pmatrix}.$$

The associated flux is deduced from the Rankine-Hugoniot relations across the wave of speed $\sigma_k^{(j_{sol})}$ or $\sigma_k^{(j_{sol}-1)}$.

3.3. Godunov type scheme

Having the HLLC multiphase Riemann solver in hands, it is now possible to derive a Godunov type scheme. For the sake of simplicity, the first-order version only is presented. As the entire cell is now considered, it is not possible to consider local conservative formulation. The system is thus considered under the form (33),

$$\frac{\partial U_k}{\partial t} + \frac{\partial F_k}{\partial x} = \frac{\sum_{l,m}\left(h\left[\chi_k^*\right]F^{*,lag}\right)_{lm,i-1/2} + \sum_{l,m}\left(h\left[\chi_k^*\right]F^{*,lag}\right)_{lm,i+1/2}}{\Delta x}, \ \forall k \in \{1,\dots,N\}$$

with

$$U_k = \begin{pmatrix} \alpha_k \\ \alpha_k\rho_k \\ \alpha_k\rho_k u_k \\ \alpha_k\rho_k E_k \end{pmatrix}, \ F_k = \begin{pmatrix} 0 \\ \alpha_k\rho_k u_k \\ \alpha_k\left(\rho_k u_k{}^2 + P_k\right) \\ \alpha_k\left(\rho_k E_k + P_k\right)u_k \end{pmatrix} \text{ and } F_{lm}^{Lag,*} = \begin{pmatrix} -u_{lm}^* \\ 0 \\ P_{lm}^* \\ P_{lm}^* u_{lm}^* \end{pmatrix}, \ (l,m) \in \{1,\dots,N\} \times \{1,\dots,N\}.$$

For a given cell i, the Godunov scheme we consider reads,

$$U_{k,i}^{n+1} = U_{k,i}^n - \frac{\Delta t}{\Delta x}\left[F_{k,i+\frac{1}{2}}^* - F_{k,i-\frac{1}{2}}^* - \sum_{l,m}\left(h\left[\chi_k^*\right]F^{*,lag}\right)_{lm,i-1/2} - \sum_{l,m}\left(h\left[\chi_k^*\right]F^{*,lag}\right)_{lm,i+1/2}\right],$$

$\forall k \in \{1,\dots,N\}$,

Δx and Δt represent respectively the space and time step. The superscripts n and $n+1$ denote two successive time steps t^n and t^{n+1}. Moreover, let us recall that $\left[\chi_k^*\right]_{lm} \neq 0$ if the contact 'l-m' goes into the cell considered.

This method is stable under conventional CFL restriction $\Delta t = CFL \dfrac{\Delta x}{Max\left(S_{L,k}, S_{R,k}\right)}$.

3.4. Computations and validations

3.4.1. Three-phase shock tube test

In this test, a shock tube with a mixture made of gas, copper and liquid water is considered in order to observe the method capabilities.

The materials are assumed governed by the 'stiffened-gas' (SG) equation of state (EOS):

$P_k = (\gamma_k - 1)\rho_k e_k - \gamma_k P_{\infty,k}$, with $k \in \{1,2,3\}$.

Parameters for the gas phase are $\gamma = 1.4$ and $P_\infty = 0\,\mathrm{Pa}$ while for the liquid phase they are $\gamma = 4.4$ and $P_\infty = 6\times10^8\,\mathrm{Pa}$. For the copper phase, $\gamma = 4.22$ and $P_\infty = 324\times10^8\,\mathrm{Pa}$.

The initial data are given as follows:

- High pressure chamber:
  Volume fractions of the gas, copper and water are respectively set to 0.8, 0.1 and 0.1. The pressure is set to $1000\,\mathrm{MPa}$.

- Low pressure chamber:
  Volume fractions of the gas, copper and water are respectively set to 0.25, 0.5 and 0.25. The pressure is atmospheric.

The densities of the gas, copper and water are respectively set to $1\,\mathrm{kg/m^3}$, $8960\,\mathrm{kg/m^3}$ and $1000\,\mathrm{kg/m^3}$. The three phases have zero initial velocities.

Stiff pressure relaxation is used everywhere contrarily to velocity drag that is absent. The results are shown at time $7.6\,\mu\mathrm{s}$ in Figure 40 and compared to those of the DEM showing very good agreement. This test is done with a uniform mesh involving 200 cells.

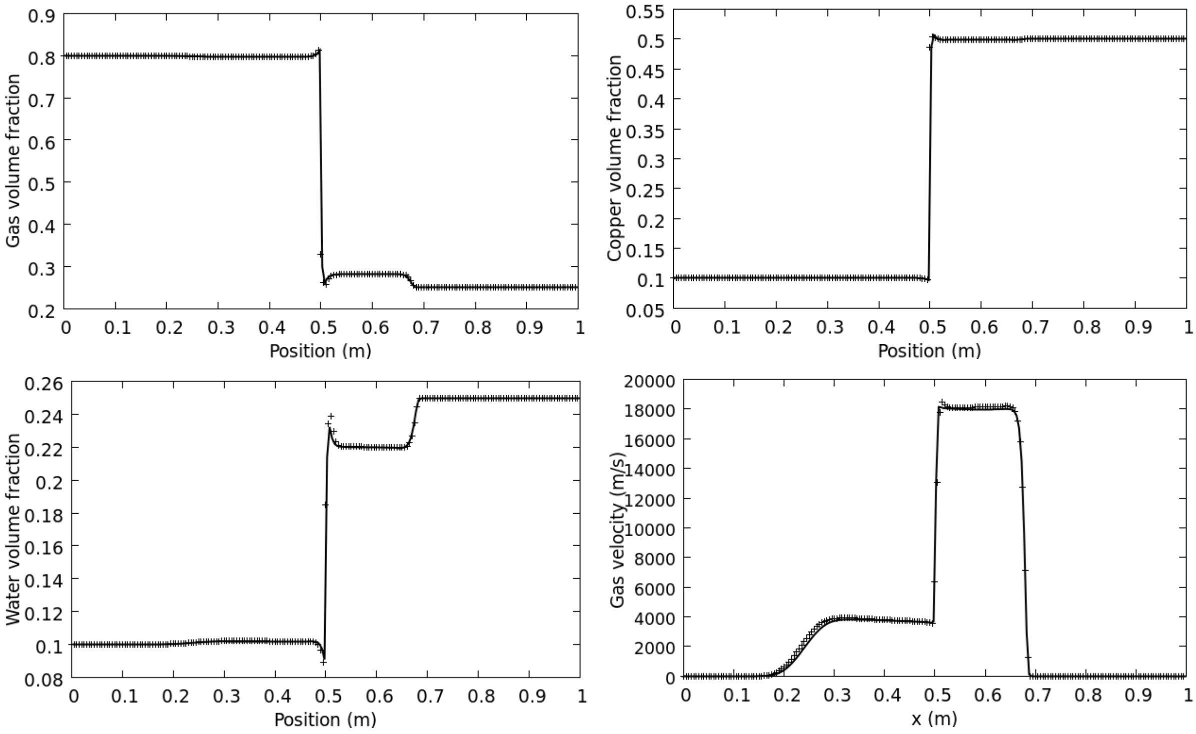

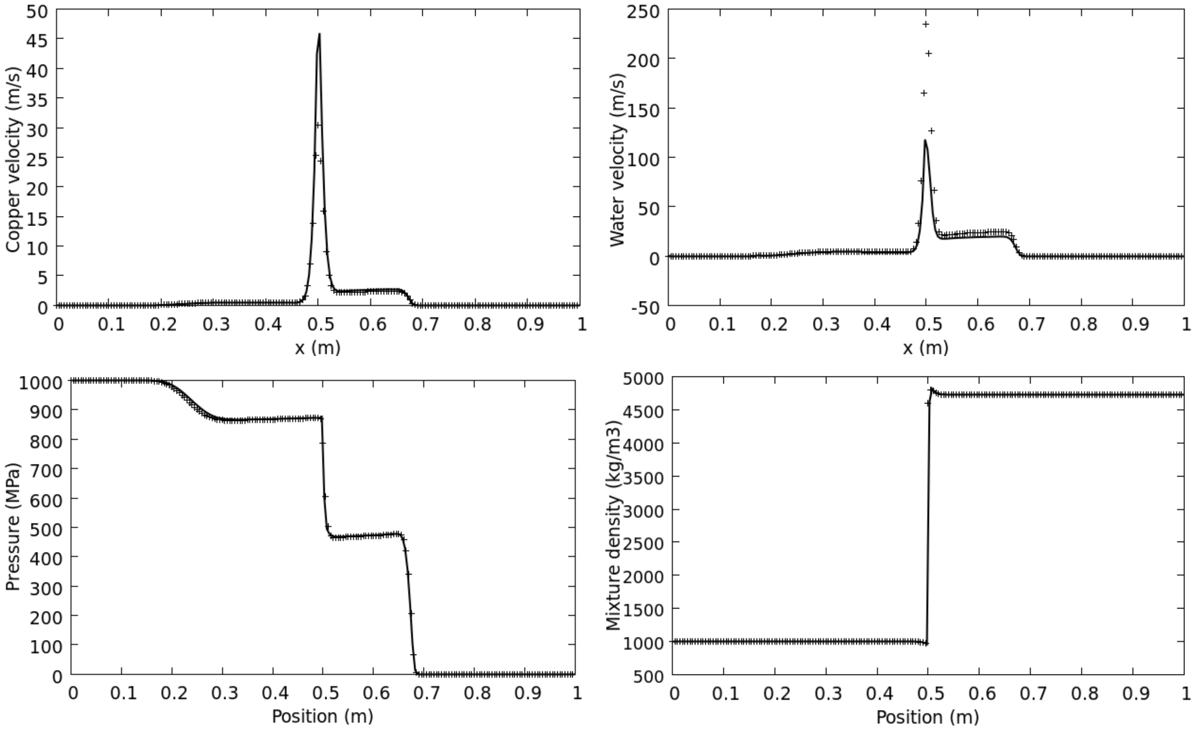

Figure 40: Three-phase shock tube test. Results of the new method are shown with symbols while those of the DEM are shown with lines. Results of the new method and those of the DEM are in very good agreement.

3.4.2. Three-phase 3D impact test

3D extension has been done in the context of arbitrary number of fluids. The process follows the lines of the previous chapter, in the frame of unstructured meshes.

A 300m/s copper projectile impacts a copper tank filled with liquid water at rest (see Figure 41). The rest of the domain is made of (nearly) pure air.

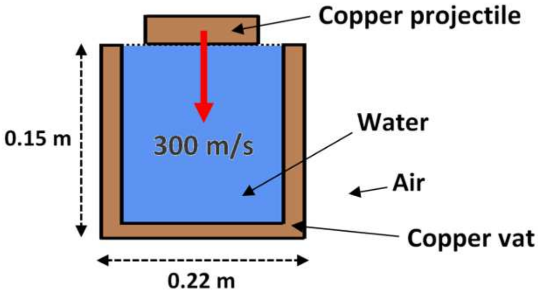

Figure 41: Impact test initial state

Copper and water are assumed governed by the 'stiffened-gas' (SG) equation of state (EOS). Parameters for the liquid water phase are $\gamma = 4.4$ and $P_\infty = 6\times10^8\,\mathrm{Pa}$, while for the copper phase they are $\gamma = 4.22$ and $P_\infty = 324\times10^8\,\mathrm{Pa}$.

The air is assumed governed by the Noble-Abel EOS. Details regarding this EOS are given in Appendix 3.B. The air covolume is taken as η=0.0003 m^3/kg and the specific heat ratio is $\gamma = 1.4$.

The densities of the gas, copper and water are respectively set to $1.225\,\mathrm{kg/m^3}$, $8960\,\mathrm{kg/m^3}$ and $1000\,\mathrm{kg/m^3}$. The pressure is atmospheric in the initial state. Moreover, in a given sub-volume (for example the copper tank), volume fractions of the two phases in minor proportions are set to 0.0005 (for the same example, air and water).

Stiff pressure and velocity relaxations are used everywhere. The results are shown at different times in Figure 42. This test is done with a uniform unstructured mesh involving 711.000 tetrahedrons.

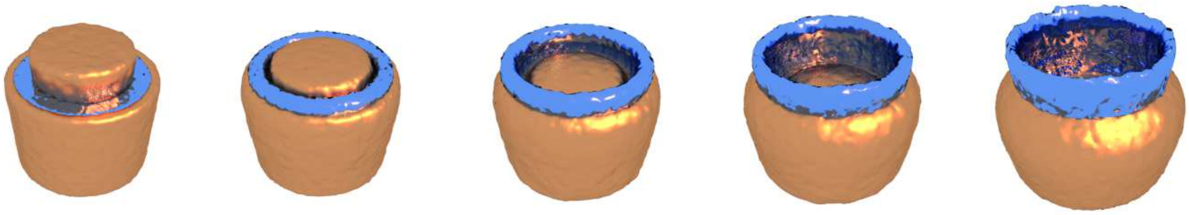

Figure 42: Impact test – Numerical results at different times ($t=0$, $t=90\,\mu s$, $t=170\,\mu s$, $t=250\,\mu s$ and $t=360\,\mu s$).

3.5. Conclusion

The multiphase extension of the HLLC-type Riemann solver has been realized and allows the simulation of a wide range of applications. Numerical results obtained have been compared to those of the DEM showing very good agreement.

Appendix 3.A. Determination of the contact surfaces at the cell boundaries for an arbitrary number of fluids

We develop here the calculation procedure in the case of a multiphase mixture.

At a given cell boundary each fluid occupies on the right and left sides a fraction of the cross section. We denote this surface fraction by S_{kR} and S_{kL} , where the index k represents the phase and the subscripts R and L the right and left sides respectively, relative to the cell boundary.

These surface fractions are defined by: $S_{kR}=\overline{X}_k=\frac{1}{\Delta y}\int_0^{\Delta y} X_k dy$.

In the following procedure, these surface fractions are assumed equal to the volume fractions: $S_k=\alpha_k$.

Let us first examine the particular case of two phases. The method proceeds as a recurrence process in which the initial data corresponds to the left and right surface fractions with respect to the cell boundary ($i-1/2$ in this example):

$$S^{(0)}_{1,L}=\alpha_{1,i-1} \qquad S^{(0)}_{1,R}=\alpha_{1,i}$$

$$S^{(0)}_{2,L}=\alpha_{2,i-1} \qquad S^{(0)}_{2,R}=\alpha_{2,i}$$

The superscript (0) represents the initial state of the recurrence procedure. To proceed to the next step, some kind of continuity assumption has to be formulated for each phase. We assume that each phase has the maximum possible contact surface with itself. This maximum contact surface cannot exceed the smallest of the two surfaces of a given phase present at the cell boundary. This assumption provides the first two contact surfaces at the cell boundary:

$$S_{11}=\min\left(S^{(0)}_{1,L}\ ,\ S^{(0)}_{1,R}\right) \quad \text{and} \quad S_{22}=\min\left(S^{(0)}_{2,L}\ ,\ S^{(0)}_{2,R}\right).$$

From this result, the remaining available surfaces on the right and left sides of the cell boundary are readily obtained. It determines the next step of the recurrence formula:

$$S^{(1)}{}_{1,L} = S^{(0)}{}_{1,L} - S_{11} \qquad S^{(1)}{}_{1,R} = S^{(0)}{}_{1,R} - S_{11}$$

$$S^{(1)}{}_{2,L} = S^{(0)}{}_{2,L} - S_{22} \qquad S^{(1)}{}_{2,R} = S^{(0)}{}_{2,R} - S_{22}$$

The contact between two surfaces will occur necessary with the smallest of the two remaining surfaces: $S_{12} = \min\left(S^{(1)}_{1,L}\ ,\ S^{(1)}_{2,R}\right)$ and $S_{21} = \min\left(S^{(1)}_{2,L}\ ,\ S^{(1)}_{1,R}\right)$.

These results are summarized in Table 3:

Contact type	Contact surface
1-1	$S_{11} = \mathrm{Min}\ (\alpha_{1,i-1},\ \alpha_{1,i})$
1-2	$S_{12} = \mathrm{Min}\ (\alpha_{1,i-1} - S_{11}\ ,\ \alpha_{2,i} - S_{22})$
2-1	$S_{21} = \mathrm{Min}\ (\alpha_{1,i} - S_{11}\ ,\ \alpha_{2,i-1} - S_{22})$
2-2	$S_{22} = \mathrm{Min}\ (\alpha_{2,i-1}\quad \alpha_{2,i})$

Table 3: Contact surfaces at cell boundary (*i*-1/2) for a two-phase mixture.

It can be easily checked that $S_{11} + S_{12} + S_{21} + S_{22} = 1$ as well as $S_{11} + S_{12} = \alpha_{1,i-1}$, $S_{11} + S_{12} = \alpha_{1,i-1}$, $S_{11} + S_{21} = \alpha_{1,i}$ and $S_{22} + S_{12} = \alpha_{2,i}$.

We now examine the case with 3 phases. As previously the initial data corresponds to the left and right surface fractions with respect to the cell boundary:

$$S^{(0)}{}_{1,L} = \alpha_{1,i-1} \qquad S^{(0)}{}_{1,R} = \alpha_{1,i}$$

$$S^{(0)}{}_{2,L} = \alpha_{2,i-1} \qquad S^{(0)}{}_{2,R} = \alpha_{2,i}$$

$$S^{(0)}{}_{3,L} = \alpha_{3,i-1} \qquad S^{(0)}{}_{3,R} = \alpha_{3,i}$$

With the help of the continuity assumption we get :

$$S_{11} = \min\left(S^{(0)}_{1,L}\ ,\ S^{(0)}_{1,R}\right) \quad , \quad S_{22} = \min\left(S^{(0)}_{2,L}\ ,\ S^{(0)}_{2,R}\right) \quad , \quad S_{33} = \min\left(S^{(0)}_{3,L}\ ,\ S^{(0)}_{3,R}\right).$$

From which we determine the remaining surfaces:

$$S^{(1)}{}_{1,L} = S^{(0)}{}_{1,L} - S_{11} \qquad S^{(1)}{}_{1,R} = S^{(0)}{}_{1,R} - S_{11}$$

$$S^{(1)}{}_{2,L} = S^{(0)}{}_{2,L} - S_{22} \qquad S^{(1)}{}_{2,R} = S^{(0)}{}_{2,R} - S_{22}$$

$$S^{(1)}{}_{3,L} = S^{(0)}{}_{3,L} - S_{33} \qquad S^{(1)}{}_{3,R} = S^{(0)}{}_{3,R} - S_{33}$$

We now need another assumption associated with the mixture topology. A “priority” has to be defined for the contact of the various phases. Imagine that phase 1 is the solid reacting phase, phase 2 its reaction product and phase 3 an inert phase. It is legitimate to give a priority to contact between the solid phase and its reaction products. But the contact surface between these two phases cannot exceed the smallest of the two surfaces present at the cell boundary. Thus,

$$S_{12} = \min\left(S^{(1)}_{1,L}\ ,\ S^{(1)}_{2,R}\right) \quad \text{and} \quad S_{21} = \min\left(S^{(1)}_{2,L}\ ,\ S^{(1)}_{1,R}\right).$$

We then deduce :

$$S^{(2)}{}_{1,L} = S^{(1)}{}_{1,L} - S_{12} \qquad S^{(2)}{}_{1,R} = S^{(1)}{}_{1,R} - S_{21}$$

$$S^{(2)}{}_{2,L} = S^{(1)}{}_{2,L} - S_{21} \qquad S^{(2)}{}_{2,R} = S^{(0)}{}_{2,R} - S_{12}$$

$$S^{(2)}{}_{3,L} = S^{(1)}{}_{3,L} \qquad S^{(2)}{}_{3,R} = S^{(1)}{}_{3,R}$$

From which the remaining contact surfaces are deduced :

$S_{13} = \min\left(S^{(2)}_{1,L}\ , S^{(2)}_{3,R}\right)$, $S_{23} = \min\left(S^{(2)}_{2,L}\ , S^{(2)}_{3,R}\right)$, $S_{31} = \min\left(S^{(2)}_{3,L}\ , S^{(2)}_{1,R}\right)$, $S_{32} = \min\left(S^{(2)}_{3,L}\ , S^{(2)}_{2,R}\right)$.

These results are summarized in Table 4.

Contact type	Contact surface
1-1	$S_{11} = \mathrm{Min}\ (\alpha_{1,i-1}\ ,\ \alpha_{1,i})$
1-2	$S_{12} = \mathrm{Min}\ (\alpha_{1,i-1} - S_{11}\ , \alpha_{2,i} - S_{22})$
2-1	$S_{21} = \mathrm{Min}\ (\alpha_{1,i} - S_{11}\ , \alpha_{2,i-1} - S_{22})$
2-2	$S_{22} = \mathrm{Min}(\alpha_{2,i-1} \quad \alpha_{2,i})$
1-3	$S_{13} = \mathrm{Min}\ \ (\alpha_{1,i-1} - S_{11} - S_{12}, \alpha_{3,i} - S_{33})$
2-3	$S_{23} = \mathrm{Min}(\alpha_{2,i-1} - S_{22} - S_{21}, \alpha_{3,i} - S_{33})$
3-1	$S_{31} = \mathrm{Min}(\alpha_{3,i-1} - S_{33}, \alpha_{1,i} - S_{11} - S_{21})$
3-2	$S_{32} = \mathrm{Min}(\alpha_{3,i-1} - S_{33}, \alpha_{2,i} - S_{22} - S_{12})$
3-3	$S_{33} = \mathrm{Min}\ \ (\alpha_{3,i}, \alpha_{3,i-1})$

Table 4 : Contact surfaces at cell boundary (*i*-1/2) for a mixture with three phases : phase 1 is a reactive material, phase 2 its reaction products and phase 3 an inert material.

This procedure shows certain degrees of freedom for the choice of these contact surfaces, provided that the various saturation constraints are fulfilled.

Table 4 gives an example when the contact of the phases with themselves is the first priority, and when the contact between the reactive material and its products is the second priority.

From these observations, a general recurrence procedure can be proposed. It requires the definition of contact priorities at each step m of the recurrence process between two phases: phase k and its priority phase p_k^m during step m.

Example: Preceding system with 3 phases.

m=0 $p_1^0 = 1$, $p_2^0 = 2$ and $p_3^0 = 3$

m=1 $p_1^1 = 2$

m=2 $p_1^2 = 3$ and $p_2^2 = 3$

From these priorities, the contact surfaces at the cell boundary are computed at each step by the formulae: $S_{k,p_k^m} = \min(S^m_{k,L}\ , S^m_{p_k^m,R})$ and $S_{p_k^m,k} = \min(S^m_{p_k^m,L}\ , S^m_{k,R})$

The remaining surfaces at the next step of the recurrence procedure are obtained by:

$S^{m+1}_{k,L} = S^m_{k,L} - S_{k,p_k^m}$ and $S^{m+1}_{k,R} = S^m_{k,R} - S_{p_k^m,k}$.

It must be checked at the last step (m=2 here) that all $S^{m+1}_{k,L}$ and $S^{m+1}_{k,R}$ are zero.

Appendix 3.B. – Noble-Abel EOS

The Noble-Abel EOS reads,

$$p(\rho, e) = \frac{(\gamma - 1)\rho(e - q)}{1 - \eta\rho},$$

$$e(T) = c_v T + q .$$

Using this EOS, the following expressions are obtained,

$$p(\rho, T) = \frac{(\gamma - 1)\rho c_v T}{1 - \eta\rho} ,$$

$$c^2 = \frac{p(\gamma - \eta\rho)}{\rho(1 - \eta\rho)} .$$

Chapitre 4

Modélisation du changement de phase de gouttelettes liquides en présence d'un gaz multi-constituant

4.1. Introduction

Dispersed droplet flows with phase change appear in many fundamental and applied science situations such as for example combustion in automotive and spacecraft engines, cryogenic combustion and atmospheric liquid dispersion to cite a few. In most situations phase change occurs between liquid drops and corresponding vapour mixed with other gas phase chemical species, such as for example air. In such instances, phase change involves both heat diffusion in the liquid and gas phases as well as mass diffusion of the chemical species in the gas phase.

Main difficulties related to such modelling are related to multidimensional effects that have to be summarized by ODEs and algebraic systems, i.e. in 0D. Many efforts have been carried out in this direction, mainly in the frame of two-phase spray combustion (Spalding, 1953, Williams, 1958, Law, 1982, Abramzon and Sirignano, 1989, Abramzon and Sazhin 2005, Sirignano, 2014, and references therein). In the last reference arrays of droplets were considered while in former ones isolated droplets only were studied.

The present work considers the behaviour of a single droplet, cumulative effects to the mean flow being accounted for through the specific interfacial area of the droplets cloud, under the assumption of absence of interaction between drops. Moreover, the liquid phase is described with a single size of drops, space and time varying.

The present contribution follows the lines of Abramzon and Sirignano (1989) (AS89) in the sense that:

- Gas phase boundary layer effects around the droplet are considered through Nusselt and Sherwood numbers correlations. This method enables computation of heat and mass diffusion fluxes through the gas to the interface without spatial resolution of the surrounding gas. Also, this approach considers velocity slip between the liquid and gas phases as Sherwood and Nusselt numbers correlations account for it through the particle Reynolds number.
- Local thermodynamic equilibrium is considered at the interface.

- Droplet heating is considered through a heat exchange coefficient between the liquid-gas interface and the droplet core. In AS89 two-dimensional flow internal to the droplet was considered to this respect.

However, the AS89 model was derived in the aim of spray combustion modelling. In such a situation phase change occurs as a result of heat exchange from the (hot) gas to the (initially cold) droplet. The internal heat exchange to the droplet is needed to compute:

- droplet heating before reaching the saturation temperature,
- heat losses from the interface to the cold droplet core that lower the mass transfer rate through the interface energy balance.

In AS89 the energy exchange internal to the droplet is thus a corrective term to the main heat flux that comes from the gas to the interface.

In situations different to spray combustion the mass transfer rate may be a result of the energy already stored in the liquid droplet. Such situations occur for instance when the surrounding gas is suddenly depressurized, as for example in nozzle flows or in the whole sequence of spherical explosions. In these situations the liquid core temperature is higher than the saturation temperature at local pressure. Consequently droplet flashing occurs as a limit case.

In the present work a phase transition model valid in any situation is built as a generalisation and non-linear extension of the AS89 model. Both liquid and gas diffusion effects are considered without giving priority to the gas transfer heat exchange to the interface. In this sense, the model becomes symmetric and as a consequence, highly non-linear.

Rather than having weakly coupled relations for the mass and heat transfers terms such as in the AS89 model a fully coupled non-linear system of three algebraic equations is obtained. This is the first main difference. These algebraic equations are clearly established from local jump conditions of mass and energy at the interface, the closure being realised by the assumption of local thermodynamic equilibrium at the interface.

A second important difference is made for the computation of the liquid heat transfer flux. In AS89 multi-D motion inside the droplet was considered through a reduction method to compute the interfacial heat flux. In the present work, the temperature inside the drop is assumed to obey a specific profile, corresponding to a boundary layer near the interface and a core zone at uniform temperature. The boundary layer thickness is determined from the assumed temperature profile and knowledge of the liquid average temperature. The average liquid temperature is a direct consequence of the two-phase average flow model resolution.

With this method, no parameter is present. Moreover :

- The interfacial heat flux is in perfect agreement with the direct resolution of the heat equation inside the drop at any time.
- The only constraint used is energy conservation through the explicit use of the average liquid temperature.

Therefore, whatever the flow complexity is inside the drop, the present approach provides accurate interfacial heat flux provided that a core zone with uniform temperature is present and connected to the interface through a boundary layer profile. No internal mesh to the liquid droplet is used.

The mass transfer model thus consists in a set of three non-linear algebraic equations. There is no parameter in the model except physical properties of fluids in presence. The solution of this system is reached numerically in each computational cell and at each time step of the two-phase average equations resolution. It results in the computation of the mass flow rate from liquid to gas, positive in evaporation conditions and negative in condensation. It also provides mass, momentum and energy transfer terms to embed in volume average two-phase flow models.

The paper is organized as follows. The two-phase flow model under examination, with heat and mass transfers added as source terms is presented in Section 2. The conventional closure relations of this model are addressed in Section 3. The local and symmetric heat and mass transfer model for a single liquid droplet is built as follows: mass and energy interface conditions are addressed in Section 4 while the local thermodynamic equilibrium interface condition is derived in Section 5. The heat exchange coefficients, in particular the one related to heat exchange internal to the droplet are determined in Section 6. The heat and mass transfer sub-model resolution method is given in Section 7 and validation results are shown in Section 8.

4.2. Two-phase flow model and properties

Two phases are considered here: gas (g) and liquid (L). The hydrodynamic part of the model is based on the Saurel et al. (2003) symmetric variant of the Baer and Nunziato (1986) model. Heat and mass transfers have been added as source terms.

Gas phase

$$\begin{aligned}
&\frac{\partial \alpha_g}{\partial t} + u_I \frac{\partial \alpha_g}{\partial x} = \mu\left(P_g - P_L\right) + \frac{A_I \dot{m}_g}{\rho_I} \\
&\frac{\partial \alpha_g \rho_g Y_{g,air}}{\partial t} + \frac{\partial \alpha_g \rho_g Y_{g,air} u_g}{\partial x} = A_I \dot{m}_g \left(1 - Y_{g,wat,I}\right) \\
&\frac{\partial \alpha_g \rho_g Y_{g,wat}}{\partial t} + \frac{\partial \alpha_g \rho_g Y_{g,wat} u_g}{\partial x} = A_I \dot{m}_g Y_{g,wat,I} \\
&\frac{\partial \alpha_g \rho_g u_g}{\partial t} + \frac{\partial \alpha_g \rho_g u_g{}^2 + \alpha_g P_g}{\partial x} = P_I \frac{\partial \alpha_g}{\partial x} + \lambda\left(u_L - u_g\right) + A_I \dot{m}_g u_I \\
&\frac{\partial \alpha_g \rho_g E_g}{\partial t} + \frac{\partial \alpha_g \left(\rho_g E_g + P_g\right) u_g}{\partial x} = P_I u_I \frac{\partial \alpha_g}{\partial x} + \lambda \overline{u_I}\left(u_L - u_g\right) - \mu \overline{P_I}\left(P_g - P_L\right) \\
&\qquad - \frac{A_I \dot{m}_g P_I}{\rho_I} + A_I \dot{m}_g \left[Y_{g,wat,I} H_{g,wat,I} + \left(1 - Y_{g,wat,I}\right) H_{g,air,I}\right] \\
&\qquad + A_I H_{Tg}\left(T_I - T_g\right)
\end{aligned} \tag{35}$$

Liquid phase

$$\begin{aligned}
&\frac{\partial \alpha_L}{\partial t} + u_I \frac{\partial \alpha_L}{\partial x} = -\mu\left(P_g - P_L\right) - \frac{A_I \dot{m}_g}{\rho_I} \\
&\frac{\partial \alpha_L \rho_L}{\partial t} + \frac{\partial \alpha_L \rho_L u_L}{\partial x} = -A_I \dot{m}_g \\
&\frac{\partial \alpha_L \rho_L u_L}{\partial t} + \frac{\partial \alpha_L \rho_L u_L{}^2 + \alpha_L P_L}{\partial x} = P_I \frac{\partial \alpha_L}{\partial x} - \lambda\left(u_L - u_g\right) - A_I \dot{m}_g u_I \\
&\frac{\partial \alpha_L \rho_L E_L}{\partial t} + \frac{\partial \alpha_L \left(\rho_L E_L + P_L\right) u_L}{\partial x} = P_I u_I \frac{\partial \alpha_L}{\partial x} - \lambda \overline{u_I}\left(u_L - u_g\right) + \mu \overline{P_I}\left(P_g - P_L\right) \\
&\qquad + \frac{A_I \dot{m}_g P_I}{\rho_I} - A_I \dot{m}_g H_{L,I} + A_I H_{TL}\left(T_I - T_c\right) \\
&\frac{\partial \alpha_L \rho_L n_L}{\partial t} + \frac{\partial \alpha_L \rho_L u_L n_L}{\partial x} = \alpha_L \rho_L \dot{n}_L
\end{aligned} \tag{36}$$

This model considers each phase as compressible, evolving with its own velocity, temperature and pressure. The notations are conventional in the two-phase flow literature. The variable α_k represents the volume fraction of phase k ($k \in \{g, L\}$), such that $\sum_k \alpha_k = 1$. ρ, u, P, T, e and E represent respectively the density, the velocity, the pressure, the temperature, the internal energy and the total energy ($E = e + \frac{1}{2} u^2$).

The gas phase contains two chemical species, air and water vapour, whose mass concentrations are denoted by $Y_{g,air}$ and $Y_{g,wat}$ respectively. Obviously, $Y_{g,air} + Y_{g,wat} = 1$.

In the absence of source terms, it can be shown easily that this system is hyperbolic with wave speeds u_I, $u_k \pm c_k$ and u_k for $k \in \{g, L\}$.

Closure relations are needed for the practical use of these equations. Some of them are conventional while others, in particular those related to heat and mass transfer, are the aim of the present paper.

4.3. Conventional closure relations

Many closure relations and correlations are needed. For the sake of simplicity the most popular ones are presented hereafter.

4.3.1. Equations of state

The gas phase is assumed governed by the ideal gas caloric equation of state:

$$P_g = \rho_g R_g T_g,$$

with $R_g = \frac{\hat{R}}{\hat{M}_g}$; $\hat{R} = 8.314 J.K^{-1}.mol^{-1}$ and ,

$$\frac{1}{\hat{M}_g} = \frac{Y_{g,air}}{M_{g,air}} + \frac{Y_{g,wat}}{M_{g,wat}}, \text{ with } \begin{cases} M_{g,air} = 29 \times 10^{-3} kg.mol^{-1} \\ M_{g,wat} = 18 \times 10^{-3} kg.mol^{-1} \end{cases}.$$

The temperature is deduced from the thermal equation of state,

$$e_g - \sum_{j=air,wat} Y_{gj} e_j^0 = \int_0^T \sum_{j=air,wat} Y_{gj} c_{vj} dT,$$

with $e_{wat}^0 = 2030 kJ/kg$ and $e_{air}^0 = 0$.

The specific heats at constant volume $c_{v,j}$ are taken from the CHEMKIN-II thermodynamic database (Robert, 1989).

The liquid phase is assumed governed by the stiffened gas equation of state (Le Metayer et al., 2004):

$$P_L = (\gamma_L - 1)\rho_L (e_L - e_L^0) - \gamma_L P_{\infty,L},$$

with $\gamma_L = 2.35$, $P_{\infty,L} = 10^9 Pa$ and $e_L^0 = -1167 kJ/kg$, this last parameter being linked to the liquid water specific heat of formation.

This EOS involves both molecular thermal agitation through the term $(\gamma_L\text{-}1)\rho_L\left(e_L - e_L^0\right)$ and attractive short distance intermolecular effects through the term $\text{-}\gamma_L P_{\infty,L}$. An improved version of this EOS, including short distance repulsive effects is in construction (Le Metayer and Saurel, 2015).
In the frame of the stiffened gas EOS the thermal one reads,

$$e_L = c_{v,L} T_L + \frac{P_{\infty,L}}{\rho_L} + e_L^0,$$

with $c_{v,L} = 1816 \mathrm{J.kg^{-1}.K^{-1}}$
Obviously, both liquid and gas may be governed by other equations of state. Here, the liquid and gas parameters are such that the phase diagram is correctly reproduced in a given temperature range (Le Metayer et al., 2004).

4.3.2. Interfacial variables

The interfacial pressure and velocity are expressed with formulas symmetric with respect to the phase's indexes,

$$P_I = \frac{Z_L P_g + Z_g P_L}{Z_g + Z_L} + \operatorname{sgn}\left(\frac{\partial \alpha_g}{\partial x}\right) \frac{Z_g Z_L}{Z_g + Z_L}\left(u_L - u_g\right),$$

$$u_I = \frac{Z_g u_g + Z_L u_L}{Z_g + Z_L} + \operatorname{sgn}\left(\frac{\partial \alpha_g}{\partial x}\right) \frac{P_L - P_g}{Z_g + Z_L},$$

where $Z_k = \rho_k c_k$ represents the acoustic impedance of phase k with c_k the associated sound speed. These interfacial variables control the dynamics of droplet clouds, as they express velocity transport and forces acting at volume fraction gradients. They are consequences of local Riemann problem resolution in volume fraction gradient zones (Saurel et al., 2003).
The volume average pressure and interface velocities are given by,

$$\overline{u_I} = \frac{Z_g u_g + Z_L u_L}{Z_g + Z_L},$$

$$\overline{P_I} = \frac{Z_L P_g + Z_g P_L}{Z_g + Z_L}.$$

These variables express the transport velocity and pressure force acting inside the cloud of droplets.
The interfacial density appearing in the first equation of System (35) is expressed as well by a symmetric formula with respect to the phases (Saurel et al., 2008):

$$\rho_I = \frac{\dfrac{\rho_g {c_g}^2}{\alpha_g} + \dfrac{\rho_L {c_L}^2}{\alpha_L}}{\dfrac{{c_g}^2}{\alpha_g} + \dfrac{{c_L}^2}{\alpha_L}}.$$

When the gas phase is much compressible than the liquid phase, these formulas tend to,

$P_I \to P_g$; $\overline{P_I} \to P_g$; $u_I \to u_L$; $\overline{u_I} \to u_L$ and $\rho_I \to \rho_L$.

and the limit estimates of Baer and Nunziato (1986) are recovered. However, in specific thermodynamic conditions, such as in detonation waves for example, the gas compressibility is comparable to the one of the liquid and validity of these limit estimates fails.

The interfacial total enthalpies $H_{g,wat,I}$, $H_{g,air,I}$ and $H_{L,I}$ require the determination of the interfacial temperature T_I , whose determination will be addressed in Section 4. Stagnation interfacial enthalpies are defined as,

$$H_{g,wat,I} = c_{p,g,wat} T_I + e^0_{wat} + \frac{1}{2} u_I{}^2,$$

$$H_{g,air,I} = c_{p,g,air} T_I + e^0_{air} + \frac{1}{2} u_I{}^2,$$

$$H_{L,I} = c_{p,L} T_I + e^0_L + \frac{1}{2} u_I{}^2,$$

with $c_{p,g,wat} = 1487\ \mathrm{J.kg^{-1}.K^{-1}}$, $c_{p,g,air} = 1007\ \mathrm{J.kg^{-1}.K^{-1}}$ and $c_{p,L} = \gamma_L c_{v,L}$.

4.3.3. Mechanical relaxation rates

The pressure relaxation is controlled by the following relaxation parameter:

$$\mu = \frac{A_I}{Z_g + Z_L}.$$

In practical computations, as the pressure relaxation time is typically less than one micro-second (Chinnayya et al., 2004), instantaneous pressure relaxation is achieved after each computational time step with the help of relaxation solvers such as those given in Lallemand and Saurel (2000). With stiff pressure relaxation solvers knowledge of the relaxation parameter μ and specific interfacial area A_I are useless. However, the interfacial area is needed to express drag effects as well as heat and mass transfers as they occur through interfaces on typical time scales much larger than the pressure relaxation one.

The specific interfacial area is expressed from the particle droplet size, that is evolving in the present context as mass transfer is considered. Here, the droplets are assumed spherical with the same average size (radius r_L) given by:

$$\alpha_L = \frac{4}{3} \pi r_L^3 (\alpha_L \rho_L n_L) \text{ or alternatively, } r_L = \left(\frac{3}{4\pi \rho_L n_L} \right)^{1/3}. \qquad (37)$$

The number density of particles per unit mass n_L is necessary to compute the particle radius. Its evolution is given by the last equation of System (36). The product $(\alpha_L \rho_L n_L)$ can also be denoted as N_L, the number density per unit volume.

When the particle radius is determined, there is no difficulty to compute the specific interfacial area, $A_I = 4\pi r_L^2 (\alpha_L \rho_L n_L)$.

In this equation, a **droplet fragmentation** term may be present $\dot{n}_L$. This source term is estimated with the algorithm that follows:

- The fragmentation time t_F is computed as,

$$t_F = \tau \frac{2 r_L}{|u_L - u_g|} \sqrt{\frac{\rho_L}{\rho_g}},$$

where τ is a dimensionless time given by correlations based on the Weber number (Pilch and Erdman, 1987). It reads,

$$\tau = \frac{\pi}{4}\left[\frac{\sigma}{\rho_l D^3} - 6.25\frac{\mu_l}{\rho_l D^2}\right]^{-0.5} \qquad \mathrm{We} \le 12$$

$$\tau = 6(\mathrm{We}-12)^{-0.25} \qquad 12 < \mathrm{We} \le 18$$

$$\tau = 2.45(\mathrm{We}-12)^{0.25} \qquad 18 < \mathrm{We} \le 50$$

$$\tau = 14.1(\mathrm{We}-12)^{-0.25} \qquad 50 < \mathrm{We} \le 350$$

$$\tau = 0.766(\mathrm{We}-12)^{0.25} \qquad 350 < \mathrm{We} \le 2760$$

$$\tau = 5.5 \qquad 2760 < \mathrm{We}$$

The Weber number is defined as,

$$\mathrm{We} = \frac{2\rho_g \left|u_L - u_g\right|^2 r_L}{\sigma},$$

where σ denotes the liquid-gas surface tension coefficient.

- The droplet radius at the end of the fragmentation process is estimated as,

$$r_f = \frac{\sigma \mathrm{We}^*}{2\rho_g \left|u_L - u_g\right|^2},$$

where We* =12 denotes the critical Weber number, the lower limit of the fragmentation process.

From these relations the following relaxation equation is obtained for the droplet size determination:

$$\frac{dr_L}{dt} = \frac{r_f - r_L}{t_F}.$$

With the help of Relation (37) and mass conservation equation of System (36) it becomes:

$$\frac{\partial \alpha_L \rho_L n_L}{\partial t} + \frac{\partial \alpha_L \rho_L u_L n_L}{\partial x} = -\frac{3\alpha_L \rho_L}{r_L}\frac{r_f - r_L}{t_F}.$$

As the droplet radius decreases during fragmentation, the number density increases.

To close this mechanical relaxation subsection it remains to examine velocity relaxation.

Drag effects

The drag parameter λ appearing in systems (35) and (36) is actually a function of the particle Reynolds number defined as,

$$\mathrm{Re}_p = \frac{2\rho_g r_L \left\|\vec{u}_g - \vec{u}_l\right\|}{\mu_g},$$

where μ_g represents the gas viscosity.

With the help of this Reynolds number it is possible to determine the drag coefficient (Clift et al., 1978),

$$\mathrm{Cd} = \begin{cases} \dfrac{24}{\mathrm{Re}_p}(1 + 0.15\,\mathrm{Re}_p^{0.687}) & \text{if} \quad \mathrm{Re}_p < 1000 \\ 0.432 & \text{otherwise} \end{cases}.$$

Then, the drag parameter is obtained as,

$$\lambda = \frac{3\alpha_L C_d \alpha_g \rho_g \left|u_g - u_L\right|}{8 r_L}.$$

Conventional closure relations being now given, we now address the aim of the present paper, i.e., heat and mass transfer closure relations.

4.4. Building the symmetric heat and mass transfer model

We now address building of the algebraic flow model to determine the last unknown functions appearing in Systems (1-2):

- The gas mass flow rate $\dot{m}_g$.
- The interfacial temperature T_I.
- The interfacial water vapor mass fraction in the gas phase $Y_{g,wat,I}$.

The gas heat exchange coefficient H_{Tg} is determined on the basis of conventional Nusselt number correlations while the internal heat exchange coefficient H_{TL} and the droplet core temperature T_c (appearing in the liquid energy equation of System 2) will be the subject of special attention in a forthcoming section.

The algebraic system giving the three unknowns $\dot{m}_g$, T_I and $Y_{g,wat,I}$ is a consequence of jump conditions of mass, energy and local thermodynamic equilibrium. These jump conditions are determined and examined hereafter.

4.4.1. Interface conditions

Local balance equations

In the present approach drops are made of pure liquid and surrounded by a gas mixture made of air and water vapour.

The mass conservation equation for each chemical species $i \in \{air, wat\}$ in a given phase $k \in \{L, g\}$ reads:

$$\frac{\partial \rho_k Y_{k,i}}{\partial t} + \vec{\nabla} \cdot \left(\rho_k Y_{k,i} \vec{u}_k - \rho_k D_{k,i} \vec{\nabla}(Y_{k,i}) \right) = 0 .$$

In the gas phase, it is assumed that each mass diffusion coefficients $D_{g,air} = D_{g,wat} = D_g$ are equal. In the liquid phase, knowledge of this coefficient is useless as the liquid is assumed pure: $Y_{L,air} = 0$ and $Y_{L,water} = 1$.

Neglecting viscous dissipation the energy conservation equation for each phase k reads,

$$\frac{\partial \rho_k E_k}{\partial t} + \vec{\nabla} \cdot \left(\rho_k E_k \vec{u}_k + P_k \vec{u}_k + \vec{q}_k \right) = 0 , \ k \in \{g, L\},$$

where $\vec{q}_k$ denotes the heat flux,

$$\vec{q}_k = -\lambda_{T,k} \vec{\nabla} T_k - \rho_k D_k \sum_i h_{k,i} \vec{\nabla} Y_{k,i} ,$$

and $\lambda_{T,k}$ denotes the phase k thermal conductivity.

In the following, the flow is assumed locally isobaric and at low Mach number in both phases, similarly as in flames dynamics (Klein, 2005). These assumptions are realistic as evaporation fronts propagate at low speed compared to the speed of sound. Acoustic waves propagate fast and are responsible for pressure uniformity, at least at leading order. Two consequences follow:

- The energy equation reduces to,

$$\frac{\partial \rho_k e_k}{\partial t} + \vec{\nabla} \cdot \left(\rho_k h_k \vec{u}_k + \vec{q}_k \right) = 0 ,$$

where e_k and h_k represent respectively the specific internal energy and enthalpy ($h_k = e_k + \frac{P_k}{\rho_k}$).

- The momentum equation is replaced by the uniform pressure condition.

The above mass and energy equations being frame invariant the system remains the same when expressed in the frame of the interface. The only change appears in the definition of the phases velocity,

$\hat{\vec{u}}_k = \vec{u}_k - \vec{\sigma}$,

where $\vec{\sigma}$ represents the local interfacial velocity.

With these notations the system reads,

$$\frac{\partial \rho_k Y_{k,i}}{\partial t} + \vec{\nabla}.\left(\rho_k Y_{k,i}\hat{\vec{u}}_k - \rho_k D_k \vec{\nabla} Y_{k,i}\right) = 0 \tag{38}$$

$$\frac{\partial \rho_k E_k}{\partial t} + \vec{\nabla}\cdot\left(\rho_k h_k \hat{\vec{u}}_k + \vec{q}_k\right) = 0,$$

with $\vec{q}_k = -\lambda_{T,k}\vec{\nabla} T_k - \rho_k D_k \sum_i h_{k,i}\vec{\nabla} Y_{k,i}$, $i \in \{air, wat\}$ and $k \in \{L, g\}$.

In the following, the notation '^' is omitted.

Jump conditions

Figure 43 represents a control volume at the drop boundary. System (38) is integrated in this control volume. The local interface velocity $\vec{\sigma}$ is assumed constant so that the flow configuration is steady and the time derivatives of the System (38) vanish. It means that the drop is large enough or that the front velocity is not varying significantly in the time range of observation. Thanks to these assumptions System (38) imply the following jump conditions:

$$\int_{S_g}\left(\rho_g Y_{g,i}\vec{u}_g - \rho_g D_g \vec{\nabla} Y_{g,i}\right).\vec{n}_g\, dS + \int_{S_L}\left(\rho_L Y_{L,i}\vec{u}_L - \rho_L D_L \vec{\nabla} Y_{L,i}\right).\vec{n}_L\, dS = 0 \tag{39}$$

$$\int_{S_g}\left(\rho_g h_g \vec{u}_g + \vec{q}_g\right).\vec{n}_g\, dS + \int_{S_L}\left(\rho_L h_L \vec{u}_L + \vec{q}_L\right).\vec{n}_L\, dS = 0 \tag{40}$$

where $\vec{n}_g$ and $\vec{n}_L$ denote the outward unit normal vectors of the corresponding phases. When the lateral surface ε tends to zero the liquid and gas surfaces S_g and S_L merge.

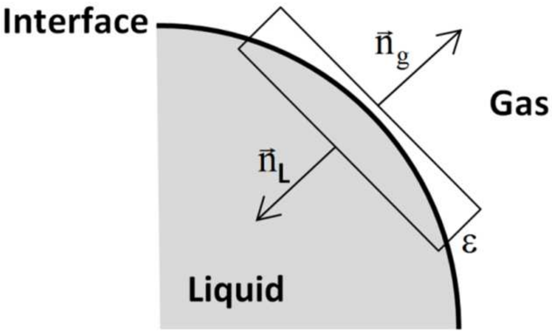

Figure 43. Schematic representation of a small control volume containing the interface.

4.4.2. Examination of the mass interface condition

For each species $i \in \{air, wat\}$, equation (39) implies:

$$\left(\rho_g Y_{g,i}\vec{u}_g - \rho_g D_g \vec{\nabla} Y_{g,i}\right).\vec{n}_g + \left(\rho_L Y_{L,i}\vec{u}_L - \rho_L D_L \vec{\nabla} Y_{L,i}\right).\vec{n}_L = 0$$

Upon summation it reads,

$$\left(\rho_g \vec{u}_g \sum_i Y_{g,i} - \rho_g D_g \sum_i \vec{\nabla} Y_{g,i}\right).\vec{n}_g + \left(\rho_L \vec{u}_L \sum_i Y_{L,i} - \rho_L D_L \sum_i \vec{\nabla} Y_{L,i}\right).\vec{n}_L = 0$$

and simplifies as,

$$\sum_k \rho_k \vec{u}_k.\vec{n}_k = 0$$

i.e.,

$$\dot{m}_g + \dot{m}_L = 0 \ , \tag{41}$$

with the following definition for the mass flux: $\dot{m}_k = \rho_k \vec{u}_k.\vec{n}_k$.

The conservation equation for each chemical species i then reads :

$$\dot{m}_g Y_{g,i} - \rho_g D_g \vec{\nabla} Y_{g,i}.\vec{n}_g + \dot{m}_L Y_{L,i} - \rho_L D_L \vec{\nabla} Y_{L,i}.\vec{n}_L = 0$$

The liquid being pure extra simplification appears:

$$\dot{m}_g Y_{g,i} - \rho_g D_g \vec{\nabla} Y_{g,i}.\vec{n}_g + \dot{m}_L Y_{L,i} = 0 \tag{42}$$

Furthermore, considering Fick's first law of diffusion for each species of the gas phase,

$$\vec{J}_{g,i} = -\rho_g D_g \vec{\nabla} Y_{g,i} \, ,$$

Equation (42) becomes,

$$\dot{m}_g Y_{g,i} + \vec{J}_{g,i}.\vec{n}_g + \dot{m}_L Y_{L,i} = 0$$

As $\sum_i Y_{g,i} = 1$ it implies $\vec{\nabla}\left(\sum_i Y_{g,i}\right) = 0$ and consequently $\sum_i \vec{J}_{g,i} = 0$.

It is worth to mention that the above simplified expressions are differential equations since gradients are present in the Fick's law. In order to transform these ODEs to an algebraic system mass exchange coefficient is introduced,

$$\vec{J}_{g,i} = \rho_g H_{Mg}\left(Y_{g,i,I} - Y_{g,i,\infty}\right)\vec{n}_g$$

where,

- $Y_{g,i,I}$ denotes the concentration of species i in the phase g at the interface,
- $Y_{g,i,\infty}$ represents the concentration of species i in the phase g far from the interface,
- H_{Mg} denotes the mass exchange coefficient in the gas phase.

Estimation of the mass exchange coefficient

The mass exchange coefficient between the gas phase and the interface is expressed with the help of the Sherwood number definition:

$$S_h = \frac{2 r_L H_{Mg}}{D_g} \, .$$

Sherwood number correlations are deduced from Nusselt number ones. The popular Frossling (1956) correlation is reported hereafter:

$$N_u = 2 + 0.522 {R_{ep}}^{1/2} {P_r}^{1/3} \tag{43}$$

The particle Reynolds number R_{ep} has already been defined and the Prandtl number P_r is defined as:

$$P_r = \frac{\mu_v c_p}{\lambda_{T,g}},$$

with μ_v the gas dynamic viscosity, c_p the gas heat capacity at constant pressure and $\lambda_{T,g}$ the gas thermal conductivity.

The Sherwood number is deduced from (43),

$$S_h = 2 + 0.522\, R_{ep}{}^{1/2} S_c{}^{1/3},$$

where S_c is the Schmidt number defined by,

$$S_c = \frac{\mu_v}{\rho_g D_g}.$$

Algebraic form of the mass interface condition

Thanks to the previous definitions it is possible to express System (42) as,

$$\dot{m}_g Y_{g,air,I} + \rho_g H_{Mg}\left(Y_{g,air,I} - Y_{g,air,\infty}\right) = 0$$

$$\dot{m}_g Y_{g,wat,I} + \rho_g H_{Mg}\left(Y_{g,wat,I} - Y_{g,wat,\infty}\right) + \dot{m}_L = 0$$

As their sum reduces to,

$$\dot{m}_g + \dot{m}_L = 0,$$

the gas mass flux reads,

$$\dot{m}_g = \frac{\rho_g H_{Mg}\left(Y_{g,wat,I} - Y_{g,wat,\infty}\right)}{1 - Y_{g,wat,I}} \tag{44}$$

This equation expresses the gas mass flow rate emitted by a liquid surface under the sole effect of molecular mass diffusion. Such mass flux is valid when the liquid and gas temperatures are in equilibrium, as for example when a wet piece of cloth is put in dry air or inversely when a dry cloth is put in humid air.

Thereafter energetic effects are considered as they are of leading importance when thermal disequilibrium is present.

4.4.3. Examination of the energy jump relation at the interface

Equation (40) implies,

$$\left(\rho_g h_g \vec{u}_g + \vec{q}_g\right).\vec{n}_g + \left(\rho_L h_L \vec{u}_L + \vec{q}_L\right).\vec{n}_L = 0, \tag{45}$$

where the heat flux is given by the sum of the Fourier's law and energy transport by mass diffusion terms,

$$\vec{q}_k = -\lambda_{t,k}\nabla T_k - \rho_k D_k \sum_i h_{k,i}\nabla Y_{k,i},\ i \in \{air, wat\} \text{ and } k \in \{L, g\}.$$

The enthalpy of the phase k is defined by $h_k = \sum_i Y_{k,i} h_{k,i}$.

In the liquid phase, the heat flux reduces to $\vec{q}_L = -\lambda_{T,L}\nabla T_L$

With the help of the mass flux definition (45) becomes,

$\dot{m}_g h_g + \vec{q}_g.\vec{n}_g + \dot{m}_L h_L + \vec{q}_L.\vec{n}_L = 0$.

Inserting the heat flux definition it becomes,

$$\dot{m}_g \sum_i Y_{g,i} h_{g,i} - \rho_g D_g \sum_i h_{g,i} \vec{\nabla} Y_{g,i}.\vec{n}_g - \lambda_{T,g} \vec{\nabla} T_g.\vec{n}_g + \dot{m}_L \sum_i Y_{L,i} h_{L,i} - \lambda_{T,l} \vec{\nabla} T_L.\vec{n}_L = 0$$

i.e.,

$$\sum_i h_{g,i} \left(\dot{m}_g Y_{g,i} - \rho_g D_g \vec{\nabla} Y_{g,i}.\vec{n}_g \right) - \lambda_{T,g} \vec{\nabla} T_g.\vec{n}_g + \sum_i h_{L,i} \dot{m}_L Y_{L,i} - \lambda_{T,L} \vec{\nabla} T_L.\vec{n}_L = 0$$

With the help of the mass conservation at the interface for each species i,

$\dot{m}_g Y_{g,i} - \rho_g D_g \vec{\nabla} Y_{g,i}.\vec{n}_g + \dot{m}_L Y_{L,i} = 0$,

the energy equation becomes,

$$\sum_i \left(h_{L,i} - h_{g,i} \right) \dot{m}_L Y_{L,i} - \lambda_{T,g} \vec{\nabla} T_g.\vec{n}_g - \lambda_{T,L} \vec{\nabla} T_L.\vec{n}_L = 0 .$$

As done previously with mass exchanges, the Fourier's law is re-expressed with the help of a heat exchange correlation,

$-\lambda_{T,k} \vec{\nabla} T_k.\vec{n}_k = H_{Tk} \left(T_I - T_{k,\infty} \right)$

where,

- H_{Tk} represents the heat exchange coefficient, whose determination will be addressed later, particularly in the liquid phase.
- T_I represents the interfacial temperature.
- $T_{k,\infty}$ denotes the temperature of the phase k far from the interface. In particular $T_{L,\infty} = T_c$, the droplet core temperature.

The energy jump relation at the interface now becomes:

$$\sum_i \left(h_{l,i} - h_{g,i} \right) \dot{m}_l Y_{l,i} + H_{Tg} \left(T_I - T_{g,\infty} \right) + H_{TL} \left(T_I - T_c \right) = 0$$

In the liquid phase as $Y_{l,air} = 0$ and $Y_{l,water} = 1$ the previous equation then reads:

$$\left(h_{L,wat,I} - h_{g,wat,I} \right) \dot{m}_L + H_{Tg} \left(T_I - T_{g,\infty} \right) + H_{TL} \left(T_I - T_c \right) = 0 .$$

Using the interface mass condition (41), a second expression for the gas mass flux appears,

$$\dot{m}_g = \frac{H_{Tg} \left(T_{g,\infty} - T_I \right) + H_{TL} \left(T_c - T_I \right)}{L_{v,wat} \left(T_I \right)} , \qquad (46)$$

where $L_{v,wat} \left(T_I \right) = h_{g,wat,I} - h_{L,wat,I}$ represents the latent heat of vaporization.

Relation (46) can be used to determine the mass flow rate when molecular mass diffusion is absent. Such situation corresponds for example to the case of a liquid drop placed in its vapour.

In this case, the interface mass condition (44) is not defined and not considered for the mass transfer rate determination.

When both molecular and heat diffusion effects are present both relations (44) and (46) must be considered. This system involves the following unknowns,

$\dot{m}_g$, $Y_{g,wat,I}$, T_I, H_{TL} and T_c.

As only two relations are available at present (Relations 10 and 13), closure relations are needed.

The heat transfer coefficient internal to the liquid phase and the droplet core temperature determination will be addressed in Section 6. We now address mass concentration $Y_{g,wat,I}$ determination at the interface.

4.5. Local thermodynamic equilibrium

The interface is assumed at local thermodynamic equilibrium, meaning:

- $T_{g,I} = T_{L,I} = T_I$ (local thermal equilibrium),
- $P_{g,I} = P_{L,I} = P_I = P$ (mechanical equilibrium), (47)
- $g_{g,I} = g_{L,I}$ (chemical equilibrium – see Appendix 4.A for details regarding this relation).

g_k represents the Gibbs free energy of a given phase ($g_k = h_k - T_k s_k$).

In the second relation of System (47) surface tension effects have been neglected, as well as in Appendix 4.A.

Any thermodynamic state function, such as g_k is function of two thermodynamic variables: $g_k = g_k(T_k, P_k)$. From System (47) it appears that,

$g_{g,I}(T_I, P) = g_{L,I}(T_I, P)$.

This relation implies the well known saturation condition,

$T_I = T_{sat}(P)$ or alternatively, $P = P_{sat}(T_I)$.

In the present particular situation, the vapor partial pressure at the drop interface is equal to the saturation pressure at local temperature T_I :

$$P_{g,wat,I} = P_{sat,wat}(T_I)$$

The gas mixture is now assumed ideal in the sense that each gas is supposed to obey the ideal gas law. From the Dalton law for ideal gases, the gas mixture pressure is equal to the sum of the individual gas species partial pressures. In the present context the water vapor partial pressure obeys,

$$P_{g,wat,I} V_g = n_{g,wat,I} \hat{R} T_I ,$$

and the gas mixture obeys,

$$P V_g = \sum_i n_{g,i,I} \hat{R} T_I ,$$

both expressed in the gas at the interface.

Molar fractions are defined as,

$$x_{g,i} = \frac{n_{g,i}}{\sum_i n_{g,i}} .$$

Consequently,

$$x_{g,wat,I} = \frac{P_{g,wat,I}}{P} = \frac{P_{sat,wat}(T_I)}{P} .$$

It remains to convert mole to mass fractions:

$$Y_{g,i} = x_{g,i} \frac{M_{g,i}}{\hat{M}_g}$$

The water vapor mass fraction at the interface is thus given by,

$$Y_{g,wat,I} = \frac{M_{g,wat}}{\hat{M}_g\left(Y_{g,wat,I}\right)} \frac{P_{sat,wat}\left(T_I\right)}{P} \quad (48)$$

with $\frac{1}{\hat{M}_g} = \frac{Y_{g,wat,I}}{M_{g,wat}} + \frac{1-Y_{g,wat,I}}{M_{g,air}}$.

Water saturation pressure

Based on the Rankine's popular relation for the saturation pressure as a function of temperature, we propose the following formula, valid in the temperature range $[273\text{K}, 647\text{K}]$:

$$P_{sat,wat}(T) = \exp\left(12.98 - \frac{4900}{T}\right) \text{bars}.$$

This relation represents very well the experimental curve, as shown in the Figure 44. It is also a very good approximation of the theoretical relation resulting of System (47) and stiffened gas equation of state for the liquid and vapor pair (Le Metayer et al., 2014).

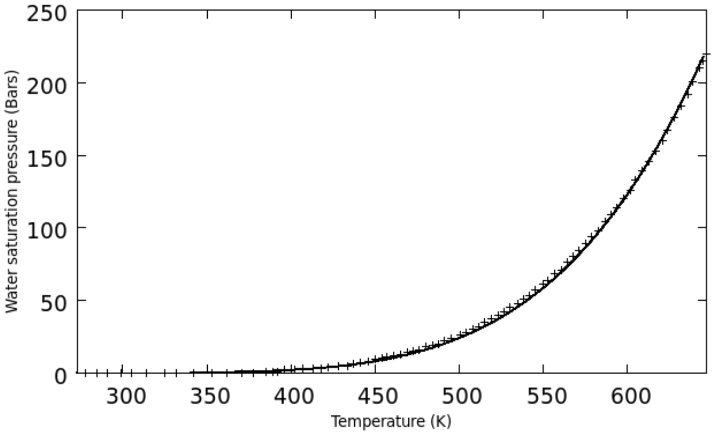

Figure 44. Comparison between the Rankine's formula adaptation (lines) and experimental data (symbols) showing excellent agreement.

Phase change model

System composed of equations (10, 13, 16) corresponds to an algebraic non-linear system with five unknowns. Solution of this system provides all variables needed to model phase change. It needs drops internal heat exchange H_{TL} and core temperature T_c determination. Their estimation is addressed in the next section.

4.6. Heat exchanges

The gas-interface heat exchange coefficient H_{Tg} is readily obtained from the Nusselt number correlation (43) and the following definition:

$$H_{Tg} = \frac{\lambda_{Tg} N_u}{2r_L}.$$

Determination of the heat exchange coefficient internal to the droplet (H_{TL}), between its core and the interface is more challenging. Attempt in this direction was done in AS89 with a constant Nusselt number of 6.58, corrected by a coefficient to account for internal fluid motion.

The present contribution departs significantly from these authors at this level as we consider that unsteady effects in drop heating (or cooling in flashing situations) may be of primary importance.

Indeed, whatever the multidimensional behavior the flow has in the droplet, at short time scales, a sharp thermal boundary layer develops near the interface. The boundary layer width is precisely linked to the interfacial heat flux that may be very large at short time scales.

As we consider challenging to account for recirculation effects inside the drop, at least with a fast method (0D or 1D), we examine an approach that:

- considers unsteadiness through radial 1D variable depth boundary layer,
- is free of adjustable parameter.

To do this the droplet is divided in two zones as shown in Figure 45.

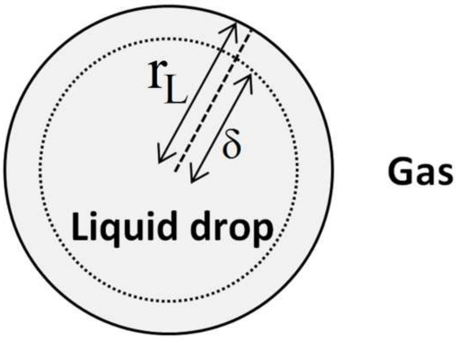

Figure 45 : Schematic representation of the liquid drop divided in two zones, a boundary layer of $r_L - \delta$ depth and a core zone of radius δ. In the boundary layer, the temperature has steep variations while it is assumed uniform in the core.

This representation addresses short terms heating or cooling of drops. When the boundary layer reaches the drop center another representation is used, preserving continuity with the two temperature profiles.

The boundary layer thickness is determined unambiguously with the method that follows. It uses:

- Approximate temperature profiles, more based on physical arguments than any given set of partial differential equations, as we consider that their solution is unreachable.
- Knowledge of volume average liquid temperature, given by the energy equation of System (36).

This last information forces the subscale model and the average one to be compatible. In particular the subscale model doesn't address any set of PDEs but fulfills the only unambiguous data that are:

- Given surface temperature T_I as it is already an unknown of System (10, 13, 16).
- Liquid energy conservation.

4.6.1. Short-term solutions

Let’s consider the following temperature profile,

$$\begin{cases} T = T_c + \left(T_I - T_c\right)\left(\dfrac{\delta - r}{\delta - r_L}\right)^n & \text{if} \quad 0 \le \delta \le r \le r_L \\ T = T_c & \text{otherwise} \end{cases} , \qquad (49)$$

where $r_L - \delta$ denotes the thermal boundary layer thickness. The parameter n is given. It will be shown latter that method's accuracy has weak dependence to this parameter.

The core temperature T_c is given too, as it corresponds in most situations to the initial liquid temperature or liquid temperature at injection. Thus, in most situations,

$T_c = \text{cst}.$

However, if the liquid is injected with time varying temperature, it will be necessary to add a transport equation to System (36):

$\frac{\partial T_c}{\partial t} + \vec{u}_L.\mathrm{grad}(T_c) = 0$, or alternatively $\frac{\partial \alpha_L \rho_L T_c}{\partial t} + \frac{\partial \alpha_L \rho_L u_L T_c}{\partial x} = 0$.

Now, if liquid compressibility induces large temperature variations, the core temperature will be better determined from the liquid entropy equation, to add to System (36) instead of the previous one,

$$\frac{\partial \alpha_L \rho_L s_L}{\partial t} + \frac{\partial \alpha_L \rho_L u_L s_L}{\partial x} = 0,$$

with a specific treatment at shocks, such as the one detailed in Petitpas et al. (2009).

From the temperature profile (49), when T_c is determined by one of the former methods the next step consists in the consideration of the local heat flux at the liquid interface:

$$\vec{q}_{L,I}.\vec{n}_L = -\lambda_{T,L} \left.\frac{\partial T}{\partial r}\right|_{r=r_L} \vec{u}_r.\vec{n}_L = \lambda_{T,L} \left.\frac{\partial T}{\partial r}\right|_{r=r_L} \equiv H_{TL}\left(T_I - T_c\right)$$

Using (49) in the previous relation implies,

$$\frac{\lambda_{T,L} n\left(T_I - T_c\right)}{\left(r_L - \delta\right)} = H_{TL}\left(T_I - T_c\right).$$

Thus,

$$H_{TL} = \frac{\lambda_{T,L} n}{\left(r_L - \delta\right)}.$$

The only remaining unknown is the distance δ. To determine it let's consider the volume average liquid drop temperature definition,

$$\overline{T}_L = \frac{1}{V}\int_0^{r_L} T dV = \frac{1}{\frac{4}{3}\pi r_L{}^3}\int_0^{r_L} T 4\pi r^2 dr = \frac{3}{r_L{}^3}\int_0^{r_L} T r^2 dr. \tag{50}$$

Inserting the temperature profile (49) in (50) results in,

$$\overline{T}_L = \frac{3\left(r_L - \delta\right)}{r_L{}^3}\left[T_c\left(\delta^2 + \frac{\left(\delta - r_L\right)^2}{3} - \delta\left(\delta - r_L\right) - \frac{\delta^3}{3\left(\delta - r_L\right)}\right) + \left(T_I - T_c\right)\left(\frac{\delta^2}{n+1} - \frac{2\delta\left(\delta - r_L\right)}{n+2} + \frac{\left(\delta - r_L\right)^2}{n+3}\right)\right]. \tag{51}$$

As $\overline{T}_L$ is an output of System (36), the only unknowns are δ and T_I. For a given T_I during the numerical resolution process of System (10, 13, 16), the distance δ is determined by solving (51) with the Newton-Raphson method.

4.6.2. Long-term solutions

"Long-term" profile happens when the boundary layer reaches the liquid drop center, e.g. $\delta = 0$. Setting $\delta = 0$ in (49) the "long -term" temperature profile is obtained:

$$T = T_c + \left(T_I - T_c\right)\left(\frac{r}{r_L}\right)^n \quad \text{if} \quad 0 \le r \le r_L \tag{52}$$

It is clear that this solution is continuity preserving with the former approximate solution (49).

Now the unknown is the liquid core temperature T_c. But its determination isn't needed for the heat exchange coefficient H_{TL} calculation. Indeed,

$$\vec{q}_{L,I}.\vec{n}_L = -\lambda_{T,L}\left.\frac{\partial T}{\partial r}\right|_{r=r_L}\vec{u}_r.\vec{n}_L = \lambda_{T,L}\left.\frac{\partial T}{\partial r}\right|_{r=r_L} \equiv H_{TL}\left(T_I - T_c\right)$$

Using (52) it appears,

$$\frac{\lambda_{T,L} n\left(T_I - T_c\right)}{r_L} = H_{TL}\left(T_I - T_c\right).$$

Thus,

$$H_{Tl} = \frac{\lambda_{t,l} n}{r_L}.$$

In order to determine the core temperature T_c that appears in the heat exchange, we use the volume average liquid temperature definition (50). Inserting the temperature profile (52),

$$\overline{T_L} = \frac{3}{{r_L}^3}\int_0^{r_L}\left(T_c + \left(T_I - T_c\right)\left(\frac{r}{r_L}\right)^n\right)r^2 dr = T_c + 3\frac{\left(T_I - T_c\right)}{\left(n+3\right)},$$

resulting in an explicit formulation for T_c,

$$T_c = \frac{\left(n+3\right)\overline{T_L} - 3T_I}{n}. \qquad (53)$$

The “long-term” temperature profile is now determined for given n, T_I and $\overline{T}_L$.

4.6.3. Validation

System (2) is considered in the absence of fluid motion and without gradients of the various flow variables. Heat exchanges only are considered resulting in the following ODE system:

$$\frac{\partial \alpha_L}{\partial t} = -\mu\left(P_g - P_L\right)$$

$$\frac{\partial \alpha_L \rho_L}{\partial t} = 0$$

$$\frac{\partial \alpha_L \rho_L u_L}{\partial t} = 0$$

$$\frac{\partial \alpha_L \rho_L E_L}{\partial t} = A_I H_{TL}\left(T_I - T_c\right) + \mu\overline{P}_I\left(P_g - P_L\right)$$

Assuming now weak pressure differential $\left(P_g - P_L\right)$ and weak liquid compressibility the energy equation becomes,

$$\frac{\partial \overline{T}_L}{\partial t} = \frac{3}{r_L \rho_L c_{p,L}} H_{TL}\left(T_I - T_c\right). \qquad (54)$$

Equation (54) is solved numerically with constant interface temperature T_I to provide the volume average temperature as a function of time $\overline{T}_L(t)$.

At each time step, the heat exchange coefficient is varying as a function of the core zone radius,

$$H_{TL}(\delta) = \begin{cases} \dfrac{\lambda_{T,L} n}{r_L - \delta} \text{ if } \delta \in \left]0; r_L\right[\\ \dfrac{\lambda_{t,l} n}{r_L} \text{ otherwise} \end{cases}.$$

Likewise, T_c varies as discussed in section 6.2. through relation (53).

Algorithm for the validation of the liquid-interface heat exchange coefficient

The following algorithm is used to determine the liquid-interface heat exchange coefficient H_{TL} and associated time varying heat flux (for given exponent n and interfacial temperature T_I in the approximate temperature profile).

1. The mean liquid temperature $\overline{T}_L(t)$ is computed from (54) in 0D computations and from System (36) in 1D computations. At the initial state $\overline{T}^0 = T_c^0$ and $\delta^0 = R - \varepsilon$. Thus, $H_{TL}^0 = \dfrac{\lambda_{t,L} n}{\varepsilon}$.
2. We first consider the "short-term" stage. The core zone radius δ is determined by solving (51). If $\delta \in]0; r_L[$, then the "short-term" assumption is checked. The heat exchange coefficient is computed and the algorithm then goes to step 1 for the next time step.
3. If $\delta \leq 0$, the heat exchange coefficient H_{TL} has to be computed with the "long-term" solution. Therefore, the liquid core temperature T_c is computed with (53). The algorithm then goes to step 1 for the next time step.

Comparison with the heat equation

Let's consider the following data:

- Interfacial temperature : $T_I = 600K$
- Liquid drop core initial temperature : $T_c^0 = 300K$
- Liquid drop radius : $r_L = 100\mu m$
- Liquid thermal conductivity : $\lambda_{T,L} = 0.6788 W.m^{-1}.K^{-1}$
- Liquid drop density : $\rho_L = 1000 kg.m^{-3}$
- Liquid drop specific heat: $c_{p,L} = 4267.6 J.kg^{-1}.K^{-1}$

The first step with this method deals with the exponent n determination. To do this, let's compare the temperature profiles for "short-terms" and different values of n (Figure 46). It appears that the solution dependence to this parameter is of minor importance. Moreover the main goal of this method is to provide an accurate approximation of the interface heat flux. This doesn't require necessarily an accurate internal temperature profile.

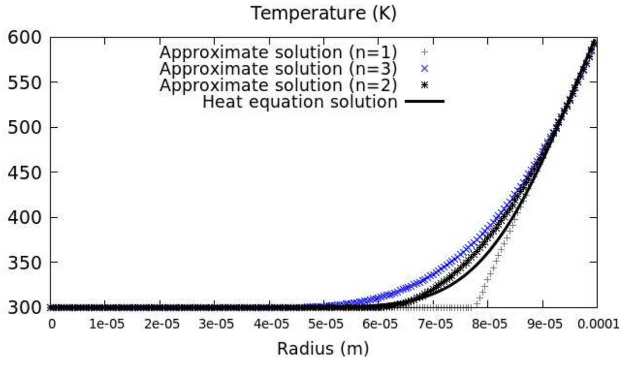

Figure 46: Short terms temperature profiles for different values of n. The dependence of the approximate solution to this parameter is not of minor importance.

To check time accuracy of the interface heat flux computation with the reduced method comparison is done with the heat equation:

$$\frac{\partial T}{\partial t} = \frac{D_{T,L}}{r^2}\frac{\partial}{\partial r}\left(r^2 \frac{\partial T}{\partial r}\right),$$

where $D_{T,L} = \frac{\lambda_{T,L}}{\rho_L c_{p,L}}$ represents the thermal diffusion coefficient in the drop.

Introducing the following change of variables,

$$\theta = \frac{T - T_c^0}{T_I - T_c^0},\ \eta = \frac{r}{r_L} \text{ and } \tau = \frac{D_L t}{{r_L}^2},$$

with T_c^0 the initial drop core temperature, the dimensionless heat equation reads:

$$\frac{\partial \theta}{\partial \tau} = \frac{1}{\eta^2}\frac{\partial}{\partial \eta}\left(\eta^2 \frac{\partial \theta}{\partial \eta}\right).$$

Consequently the interfacial heat flux reads,

$$\vec{q}_{L,I}.\vec{n}_L = \lambda_{T,L}\left.\frac{\partial T}{\partial r}\right|_{r=r_L} = \frac{\lambda_{T,L}\left(T_I - T_c^0\right)}{r_L}\left.\frac{\partial \theta}{\partial \eta}\right|_{\eta=1},$$

i.e.,

$$\frac{\vec{q}_{L,I}.\vec{n}_L}{\frac{\lambda_{T,L}\left(T_I - T_c^0\right)}{r_L}} = \left.\frac{\partial \theta}{\partial \eta}\right|_{\eta=1}.$$

The dimensionless heat flux $q_{HeatEq} = \left.\frac{\partial \theta}{\partial \eta}\right|_{\eta=1}$ is determined by solving the dimensionless heat equation with the help of finite differences. Then it is compared to the one determined with the approximate method,

$$q_{Method} = \frac{H_{TL}\left(T_I - T_c\right)}{\left(\frac{\lambda_{T,L}\left(T_I - T_c^0\right)}{r_L}\right)} = \frac{H_{TL} r_L \left(T_I - T_c\right)}{\lambda_{T,L}\left(T_I - T_c^0\right)}.$$

Corresponding results are shown in Figure 47 for $n = 2$. They show that the reduced method is accurate for the determination of the interface heat flux for this value.

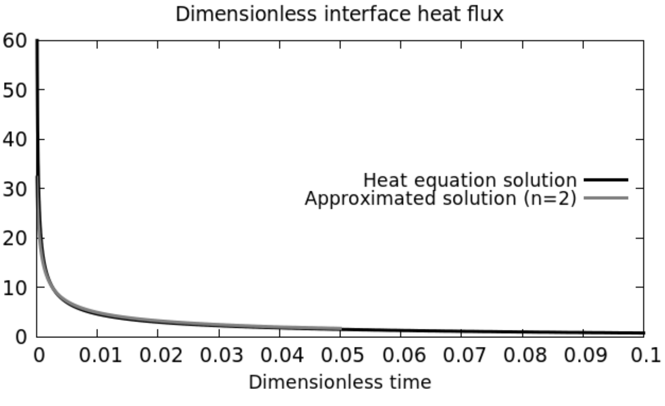

Figure 47: Dimensionless interface heat flux in gray lines for $n = 2$ as a function of dimensionless time. This result is compared to the dimensionless heat equation solution (dark lines) showing very good agreement.

These results show that the method is accurate for the interface heat flux computation at any time. In the rest of the paper, computations are made with $n = 2$.

4.7. Solving the local heat and mass transfer model

Having now in hands all closure relations to solve the mass transfer model we address its numerical resolution. This algebraic system is made of relations (44), (46) and (48):

$$\dot{m}_g = \frac{\rho_g H_{Mg}\left(Y_{g,wat,I} - Y_{g,wat,\infty}\right)}{1 - Y_{g,wat,I}} \tag{55-a}$$

$$\dot{m}_g = \frac{H_{Tg}\left(T_{g,\infty} - T_I\right) + H_{TL}\left(T_c - T_I\right)}{L_{v,wat}\left(T_I\right)} \tag{55-b}$$

$$Y_{g,wat,I} = \frac{M_{g,wat}}{\hat{M}_g\left(Y_{g,wat,I}\right)} \frac{P_{sat,wat}\left(T_I\right)}{P} \tag{55-c}$$

The system involves three unknowns: $\dot{m}_g$, $Y_{g,wat,I}$ and T_I. The core temperature T_c is assumed constant or determined by one of the equations of Section 6.1.

Moreover, $T_{g,\infty}$ is assumed equal to the volume average gas temperature T_g.

However, this system is highly nonlinear and requires a specific resolution method.

Combining (55-a) and (55-b) by eliminating the mass flux the following identity is obtained,

$$\frac{\rho_g H_{Mg}\left(Y_{g,wat,I} - Y_{g,wat,\infty}\right)}{1 - Y_{g,wat,I}} = \frac{H_{Tg}\left(T_{g,\infty} - T_I\right) + H_{TL}\left(T_c - T_I\right)}{L_{v,wat}\left(T_I\right)}.$$

Rearranging it, the interfacial temperature as a function of the vapor mass fraction at the interface is obtained:

$$T_I\left(Y_{g,wat,I}\right) = \frac{H_{Tg}T_{g,\infty} + H_{TL}T_c}{H_{Tg} + H_{TL}} - \frac{L_{v,wat}\left(T_I\right)\rho_g H_{Mg}\left(Y_{g,wat,I} - Y_{g,wat,\infty}\right)}{\left(H_{Tg} + H_{TL}\right)\left(1 - Y_{g,wat,I}\right)} \tag{56}$$

Equation (55-c) can be expressed as,

$$P_{sat,wat}\left(T_I\right) = \frac{\hat{M}_g\left(Y_{g,wat,I}\right)}{M_{g,wat}} P Y_{g,wat,I}.$$

Combining these two last relations the following function is obtained:

$$f\left(Y_{g,wat,I}\right) = P_{sat,wat}\left(\frac{H_{Tg}T_{g,\infty} + H_{TL}T_c}{H_{Tg} + H_{TL}} - \frac{L_{v,wat}\left(T_I\right)\rho_g H_{Mg}\left(Y_{g,wat,I} - Y_{g,wat,\infty}\right)}{\left(H_{Tg} + H_{TL}\right)\left(1 - Y_{g,wat,I}\right)}\right) - \frac{\hat{M}_g\left(Y_{g,wat,I}\right)}{M_{g,wat}} P Y_{g,wat,I} \tag{57}$$

Reversing Relation (56) $Y_{g,wat,I}$ can be expressed as a function of temperature T_I:

$$Y_{g,wat,I}\left(T_I\right) = \frac{Y_{g,wat,\infty} + \left(\dfrac{\dfrac{H_{Tg}T_{g,\infty} + H_{TL}T_c}{H_{Tg} + H_{TL}} - T_I}{\dfrac{\rho_g H_{Mg} L_{v,wat}}{H_{Tg} + H_{TL}}}\right)}{1 + \left(\dfrac{\dfrac{H_{Tg}T_{g,\infty} + H_{TL}T_c}{H_{Tg} + H_{TL}} - T_I}{\dfrac{\rho_g H_{Mg} L_{v,wat}}{H_{Tg} + H_{TL}}}\right)} \tag{58}$$

This expression will be convenient and of particular importance for numerical resolution.

Mathematical analysis of function $Y_{g,wat,I}(T)$ (58)

This function can be rewritten as follows:

$$Y_{g,wat,I}(T) = \frac{C + DY_{g,wat,\infty} - T}{C + D - T},\ \forall T \in \mathbb{R}_+^* - \{T_{ND}\}$$

with $T_{ND} = C + D$ and with the positive constants $C = \frac{H_{Tg}T_{g,\infty} + H_{TL}T_c}{H_{Tg} + H_{TL}}$ and $D = \frac{\rho_g H_{Mg} L_{v,wat}}{H_{Tg} + H_{TL}}$.

The function is monotonically decreasing in the interval $T \in \left]0, T_{ND}\right[\cup \left]T_{ND}, +\infty\right[$,

$$\frac{dY_{g,wat,I}(T)}{dT} = -\frac{D(1 - Y_{g,wat,\infty})}{(C + D - T)^2} < 0.$$

Moreover,

$\lim\limits_{T \to T_{ND}^-} Y_{g,wat,I}(T) = -\infty$; $\lim\limits_{T \to T_{ND}^+} Y_{g,wat,I}(T) = +\infty$; and $\lim\limits_{T \to +\infty} Y_{g,wat,I}(T) = 1$.

By definition, the water vapor mass fraction at the interface has to respect the physical condition $0 < Y_{g,wat,I}(T) < 1$. This condition is only checked for $T \in \left]0; T_0\right[$, with $T_0 = C + DY_{g,wat,\infty} < T_{ND}$ as shown in Figure 48.

Another physical bound has to be considered, i.e., the critical temperature of the liquid ($T_{crit} = 647.14\,\mathrm{K}$). The considered domain upper bound is consequently $\mathrm{Min}(T_0, T_{crit})$.

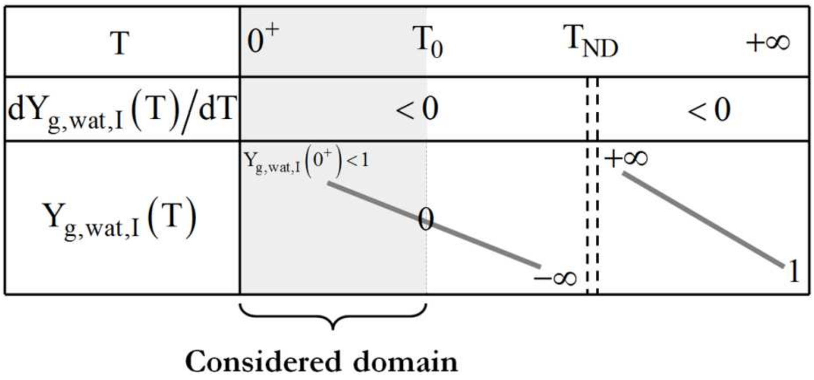

Figure 48: Mathematical analysis of function $Y_{g,wat,I}(T)$ (58).

Mathematical analysis of function $f(Y)$ (57)

Thanks to the previous definitions and using the explicit formula for $P_{sat,wat}(T)$, the function $f(Y)$ is rewritten as,

$$f(Y) = \exp\left(12.98 - \frac{4900(1 - Y)}{T_0 - T_{ND}Y}\right) \times 10^5 - \frac{M_{g,air}PY}{Y(M_{g,air} - M_{g,wat}) + M_{g,wat}},\ \forall Y \in \left]0;1\right[- \{Y_{PB}\},$$

with $Y_{PB} = \frac{T_0}{T_{ND}}$.

This function is monotonically decreasing in the interval $Y \in \left]0; Y_{PB}\right[\cup \left]Y_{PB}; 1\right[$,

$$\frac{df\left(Y\right)}{dY} = 4900\frac{T_0 - T_{ND}}{\left(T_0 - T_{ND}Y\right)^2}\exp\left(12.98 - \frac{4900\left(1-Y\right)}{T_0 - T_{ND}Y}\right)\times 10^5 - \frac{M_{g,air}PM_{g,wat}}{\left(Y\left(M_{g,air}-M_{g,wat}\right)+M_{g,wat}\right)^2} < 0 \cdot$$

Moreover,

$$\lim_{Y\to 0^+} f\left(Y\right) = P_{sat,wat}\left(T_0\right)$$

$$\lim_{Y\to Y_{PB}^-} f\left(Y\right) = f_{Y_{PB}^-} = -\frac{M_{g,air}PT_0}{T_0\left(M_{g,air}-M_{g,wat}\right)+T_{ND}M_{g,wat}} < 0$$

$$\lim_{Y\to Y_{PB}^+} f\left(Y\right) = +\infty$$

$$\lim_{Y\to 1^-} f\left(Y\right) = f_{1^-} = \exp\left(12.98\right)\times 10^5 - P \approx 433653\times 10^5 - P$$

By definition, function $f\left(Y\right)$ admits a single root in the interval $\left]0;Y_{PB}\right[$. This solution is unique, as $f\left(Y\right)$ is strictly positive in the second interval $\left]Y_{PB};1\right[$ provided that the pressure $P < 433653\,\text{bars}$, this condition being not restrictive in practical applications.

Figure 49 summarizes this analysis.

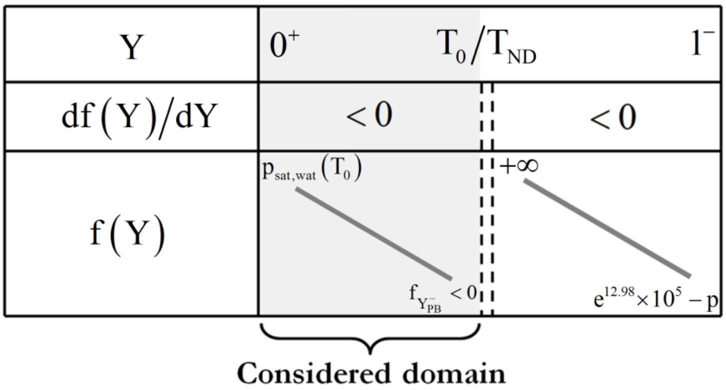

Figure 49: Mathematical analysis of function $f\left(Y\right)$ (57).

The solution algorithm for System (55) is consequently the one that follows.

Algorithm for System (55) resolution

1. Define the accuracy ε and chose an initial guess for $T_I = T_{I,new} = \frac{T_c + T_{g,\infty}}{2}$.
2. Determine the latent heat of vaporization $L_{v,wat}\left(T_{I,new}\right)$.
3. Compute the liquid-interface heat exchange coefficient $H_{Tl}\left(T_{I,new}\right)$.
4. Define admissible temperature bounds:

   $T_{min} = 0.1\ \text{K}$

   $T_{max} = \text{Min}\left(T_0 - 0.1, T_{crit} - 0.1\right)$
5. Compute mass fraction bounds using relation (58) :

   $Y_a = Y_{g,wat,I}\left(T_{max}\right)$

   $Y_b = Y_{g,wat,I}\left(T_{min}\right)$,

   with $Y_b < \lim_{T\to 0^+} Y_{g,wat,I}\left(T\right) = Y_{PB}$.

6. The Ridders' method is used to solve $f\left(Y_{g,wat,I}\right)=0$ in the domain $\left[Y_a, Y_b\right]$ resulting in the determination of $Y_{g,wat,I}$.

7. Update the temperatures using relation (56):

   $T_{I,init} = T_{I,new}$ and $T_{I,new} = T_I\left(Y_{g,wat,I}\right)$

8. If $\left|T_{I,new} - T_{I,init}\right| \geq \varepsilon$, go to step 2.

   Otherwise, $T_I = T_{I,new}$.

   Then the gas mass flow rate $\dot{m}_g$ is determined with (55-a) or (55-b).

System (55) is now solved and its solution is inserted in Systems (35) and (36).

4.8. Computational examples and validations

A simple evaporation test is addressed first, in order to check flow variables relaxation towards their equilibrium value. Model capabilities to deal with unsteady wave propagation (shock and expansion waves) are addressed secondly. Finally, we reconsider the 3D explosive liquid water test-case to observe the impact of the local heat and mass transfer model on numerical results.

4.8.1. Relaxation towards equilibrium

In this test, gas and liquid phase volume fractions are respectively set initially to $\alpha_g = 0.999$ and $\alpha_L = 0.001$. The pressure is atmospheric ($10^5\mathrm{Pa}$) and the initial water vapor mass fraction in the gas phase is set to 0.01. The initial gas phase temperature is $1000\mathrm{K}$ and the liquid phase is at $300\mathrm{K}$ initially. Moreover, the liquid droplet radius is set to $5\mu\mathrm{m}$. All variables are plotted versus time in Figure 50.

As liquid droplet evaporation occurs, the gas mass flow rate $\dot{m}_g$ is positive. Each variable gradually reaches the equilibrium state value.

It is also possible to make distinction between short time scales (with constant drop core temperature T_c which is equal to the initial liquid temperature) and long time ones (where T_c varies).

The initial liquid temperature being greater than the equilibrium one and the pressure decreasing as a result of heat loss, the average liquid temperature, the drop core temperature and the interfacial one decrease until they merge and become constants. Besides, those three temperatures are reached by the gas one T_g at the end of the evaporation process.

Non-intuitively, we observe that T_I is smaller than $\overline{T}_L$ and T_g (Figure 51). This is a consequence of the fast pressure decrease that drives the interface temperature to the saturation one while the core liquid remains hot.

4.8.2. Shock tube with droplets

In all tests that follow, the hyperbolic part of the two-phase flow model (1-2) is solved with the method given in Furfaro and Saurel (2014).

A one-meter long shock tube contains gas and liquid phases with uniform volume fraction everywhere. The gas phase occupies most of the volume ($\alpha_g = 0.999$). The left chamber has the same high pressure for both phases ($10^6\,\mathrm{Pa}$) while the right one has the same low pressure ($10^5\,\mathrm{Pa}$) for both phases. Gas and liquid temperatures are both set to $300\mathrm{K}$ everywhere.

Therefore, in all tests that follow the core temperature T_c is a constant for short terms solutions as defined in Section 6.1 while for long terms, it is computed by (54).

In these computations the right-facing shock and left-facing expansion waves propagate in liquid-gas mixtures at thermodynamic equilibrium. For given initial temperature T^0 and pressure P^0, the initial water vapor mass fraction in the gas phase $Y^0_{g,wat}$ is determined from relation (55-c):

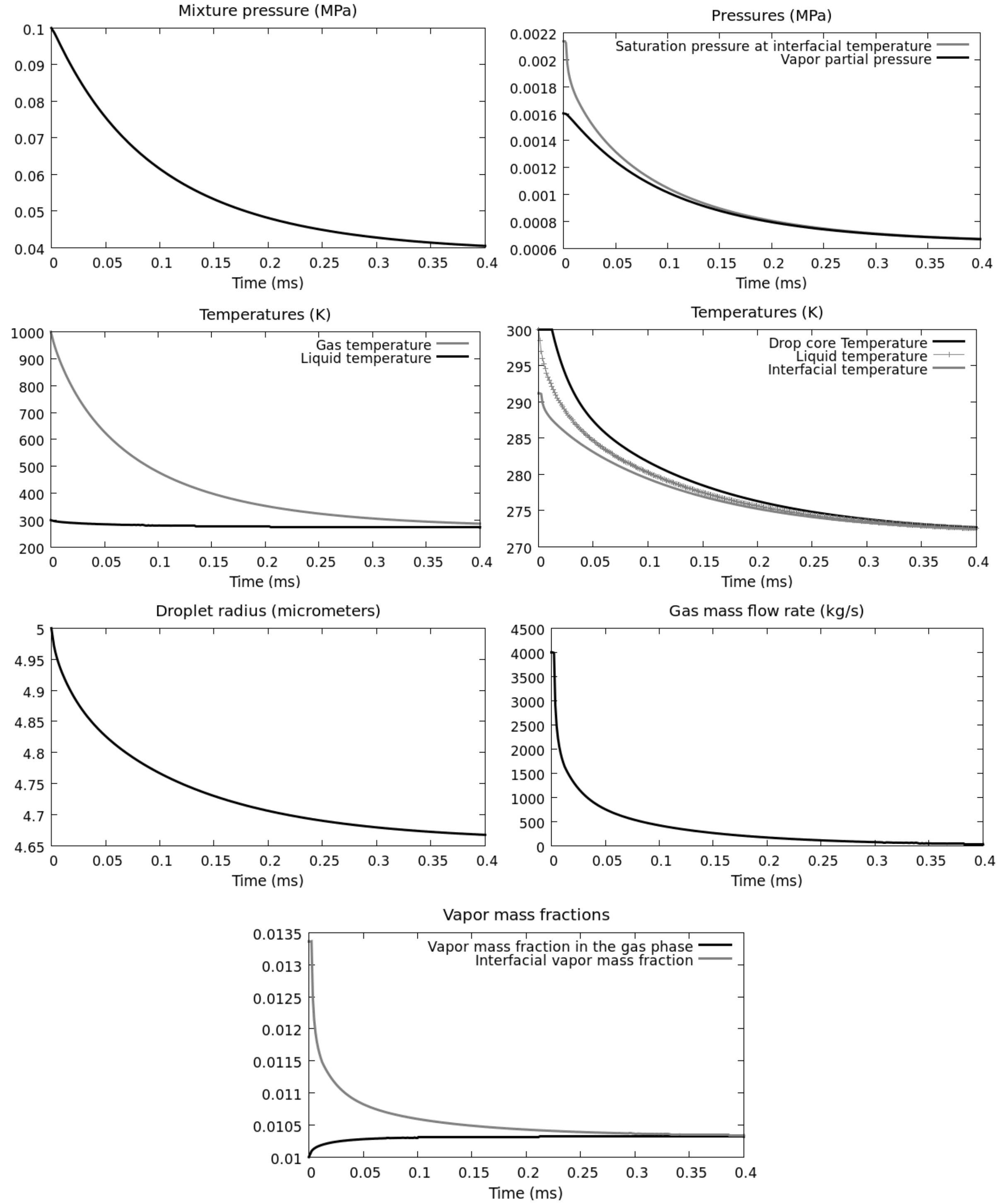

Figure 50: Evaporating droplets at rest. The equilibrium state is correctly reached at the end of the evaporation process.

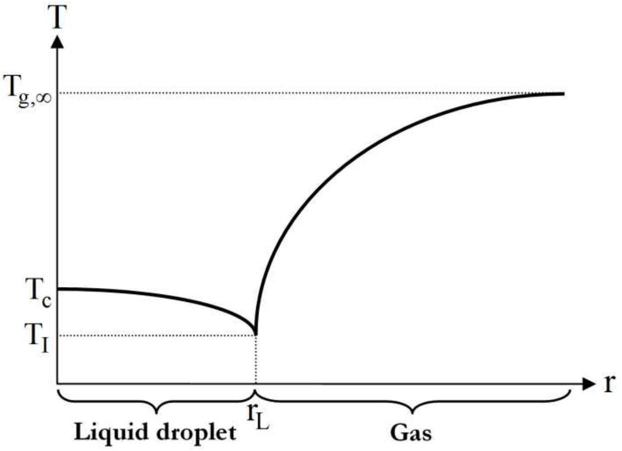

Figure 51: Evaporating droplet at rest. Non-intuitive interfacial and core temperature behaviors.

$$Y^0_{g,wat} = \frac{M_{g,wat}}{\hat{M}_g\left(Y^0_{g,wat}\right)} \frac{P_{sat,wat}\left(T^0\right)}{P^0}$$

where $\frac{1}{\hat{M}_g\left(Y^0_{g,wat}\right)} = \frac{1 - Y^0_{g,wat}}{M_{g,air}} + \frac{Y^0_{g,wat}}{M_{g,wat}}$

Therefore,

$$Y^0_{g,wat}\left(T^0, P^0\right) = \frac{\dfrac{M_{g,wat} P_{sat,wat}\left(T^0\right)}{M_{g,air} P^0}}{1 - \dfrac{P_{sat,wat}\left(T^0\right)}{P^0}\left(1 - \dfrac{M_{g,wat}}{M_{g,air}}\right)}.$$

Three successive tests are considered with different initial liquid droplet radii. In the first test (Figure 52), the droplet radius is set to $1\mu m$. The second and third ones consider same initial conditions and vary only droplet radius that is $10\mu m$ in results shown in Figure 53 and $100\mu m$ in Figure 54. Stiff pressure relaxation is used everywhere whereas velocity relaxation occurs with finite rate λ as given in Section 3.3. Breakup effects are not considered.

These tests are done with a uniform mesh involving 500 cells. The initial pressure discontinuity is located at x=0.5 m.

Let's first remark that relaxation effects imply shock waves dispersion, that do not appear as discontinuities on the various graphs. Second, as expected droplet size is of major importance on temperatures and velocities relaxation and evaporation/condensation mechanism.

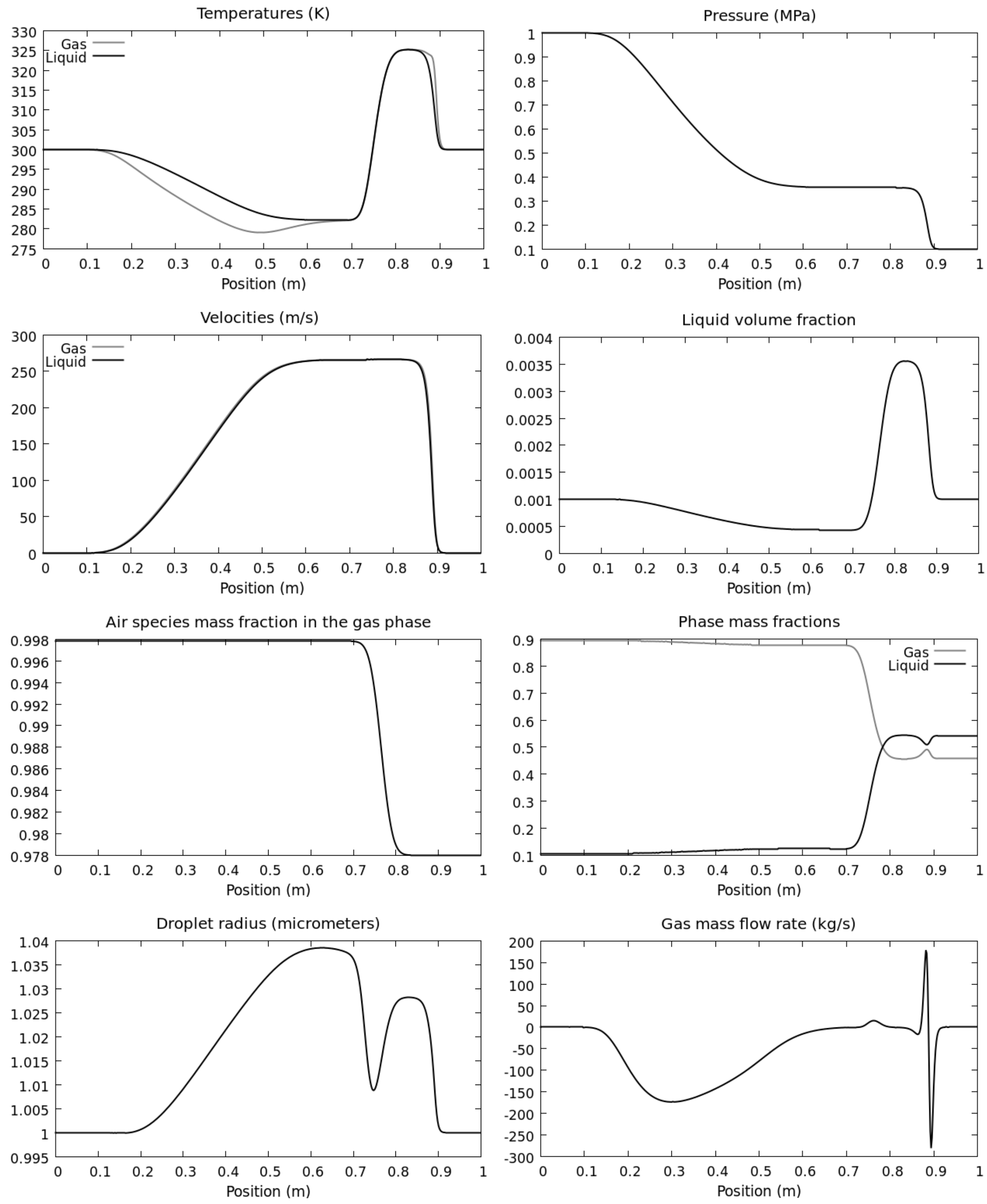

Figure 52: Gas-liquid shock tube with initial uniform volume fraction everywhere ($\alpha_g = 0.999$). The computations are made with finite rate drag and stiff pressure relaxation, on a mesh involving 500 cells. The droplet radius is set to $1 \mu m$. Results are shown at time $1 ms$. Condensation occurs at most places.

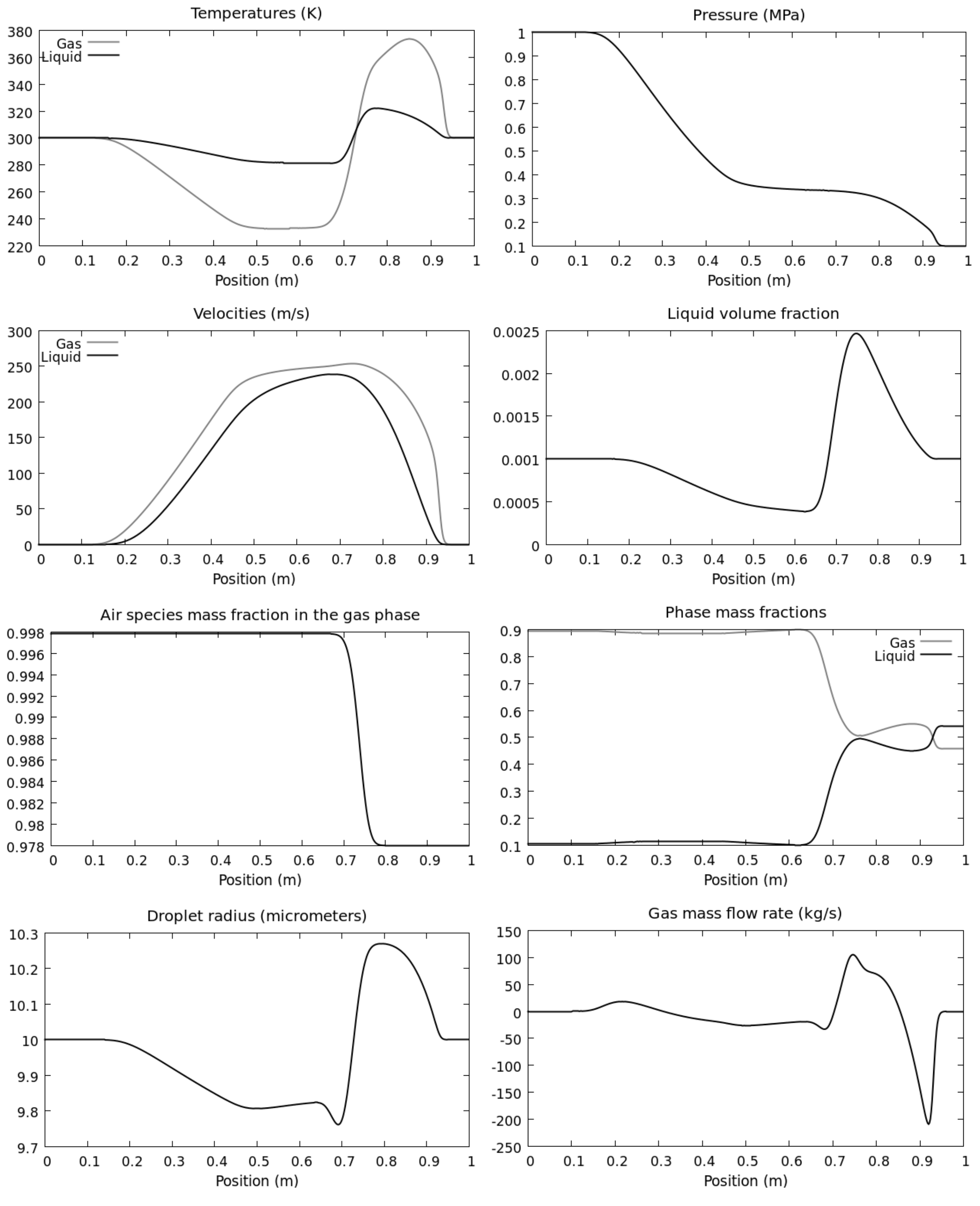

Figure 53: Shock tube containing gas and liquid phases with uniform volume fraction everywhere ($\alpha_g = 0.999$).The computations are made with drag effects and stiff pressure relaxation, on a mesh involving 500 cells. The droplet radius is set to $10\mu\text{m}$. Results are shown at time 0.91ms . Both condensation and evaporation are present.

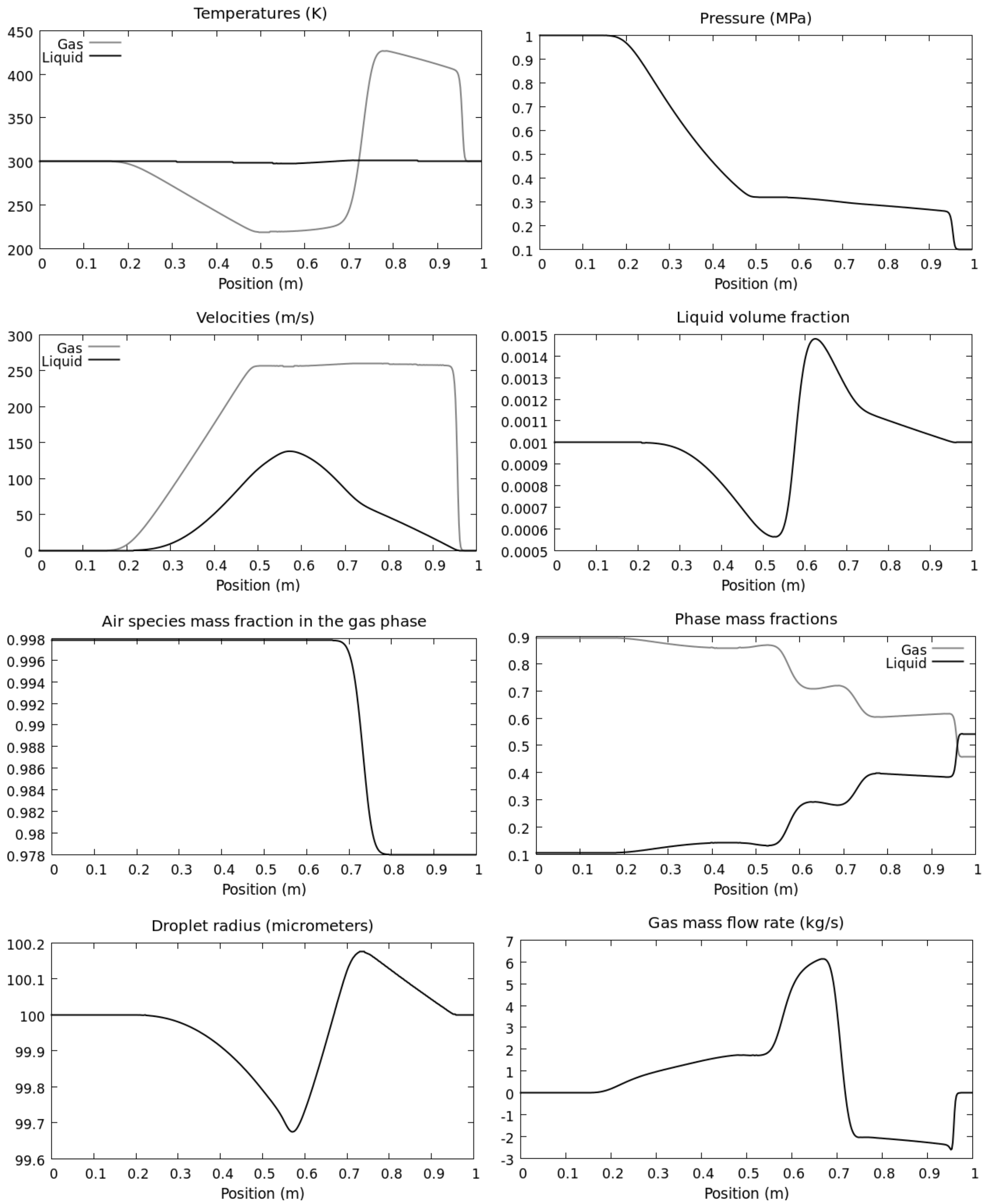

Figure 54: Shock tube containing gas and liquid phases with uniform volume fraction everywhere ($\alpha_g = 0.999$).The computations are made with drag effects and stiff pressure relaxation, on a mesh involving 500 cells. The droplet radius is set to $100\mu m$. Results are shown at time $0.83ms$. Evaporation and condensation effects are mostly related to the dynamics of the gas phase, in particular to its temperature and pressure evolutions. Condensation appears at shock and evaporation in the gas expansion wave.

When the initial droplet radius is very small ($1\mu m$) and for the considered initial liquid volume fraction ($\alpha_L = 0.001$), the interfacial area is big. Drag effects are thus stiff involving velocities merging and temperatures being close each other. Moreover, condensation appears through the rarefaction wave ($\dot{m}_g < 0$), increasing the droplet size. The same phenomenon is present through the shock wave, whereas evaporation prevails in the shocked state ($\dot{m}_g > 0$).

When the droplet radius increases ($10\mu m$) with the same initial liquid volume fraction, relaxation effects are weaker as the interfacial area is smaller. As before, condensation through the shockwave and evaporation in the shocked state are observable. However, the droplet radius behavior is very different through the rarefaction wave, where evaporation now prevails.

The same run is considered with particles radius of $100\mu m$. Mass transfer is very weak because of the low interfacial area. Evaporation occurs through the rarefaction wave and the contact discontinuity. Conversely, condensation prevails through the shock wave and in the shocked state.

It thus appears that changing only the droplet size, non-intuitive effects appear. Condensation zones may become evaporating ones with the same initial thermodynamic states, just changing the droplet size.

4.8.3. 3D explosive liquid water test-case

The local heat and mass transfer model is used hereafter in the context of the 3D unstructured code (DALPHADT). We reconsider the case of cylindrical gas-liquid explosion already introduced in Section 1.7.3. Let us recall the schematic representation of the initial state (Figure 55).

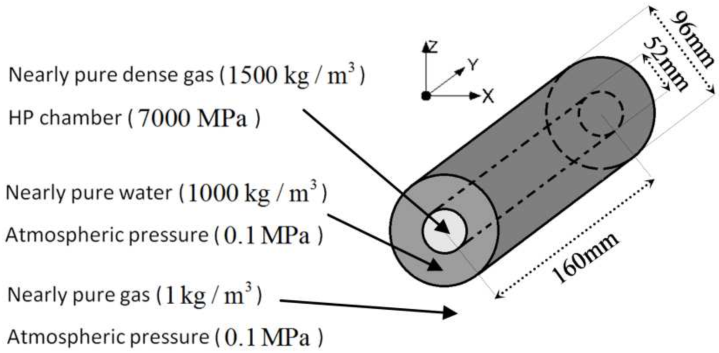

Figure 55: Schematic representation of the cylindrical gas-liquid explosion. A cylindrical explosive charge is surrounded by a liquid water layer.

The thickness of the initial liquid water layer is set to 22mm. The high pressure gradient involves deformation and propagation of the interfaces until the appearance of a cloud of droplets. To take into account this phenomenon, a droplet fragmentation law (see Section 4.3.3.) is used to allow droplets formation.

Numerical results with and without phase transition are compared in Figure 56. Liquid volume fraction contours are shown. When the phase transition model is activated, the liquid volume fraction strongly decreases until the liquid water disappears.

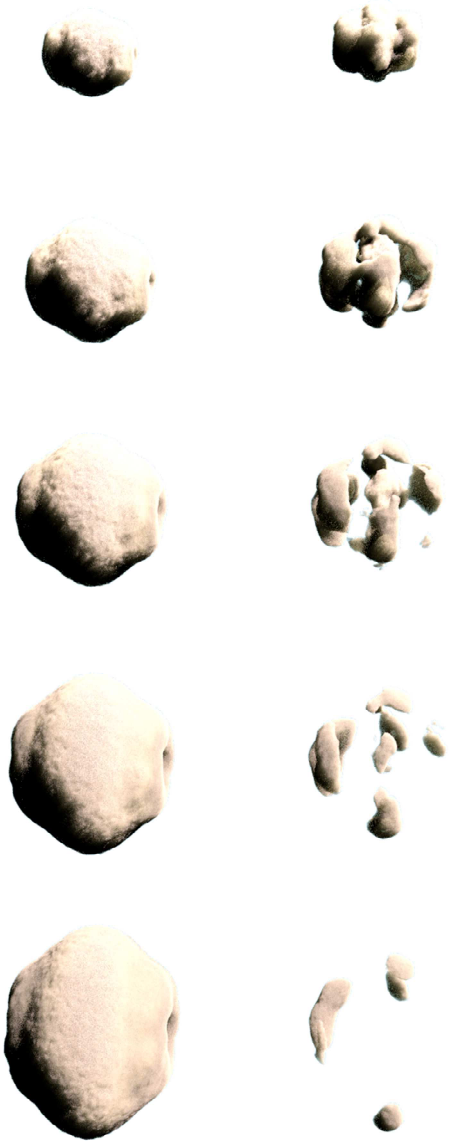

Figure 56: Numerical results of the cylindrical gas-liquid explosion are shown without and with activation of the phase transition model (respectively on the left and on the right) at different times: ($t = 80\mu s$, $t = 160\mu s$, $t = 240\mu s$, $t = 320\mu s$ and $t = 400\mu s$).

4.9. Conclusions

A variant of the AS89 model has been built. The new model considers both liquid and gas compressibility. It is symmetric in the sense that phase change may occur as a consequence of heat and mass diffusion between the interface and the gas and heat diffusion between the interface and the liquid core, where liquid internal energy may be stored. Therefore the present model is valid in any kind of evaporating/condensing situation of gas liquid droplets flows.

Appendix 4.A – Phase equilibrium

Each chemical reaction or phase transformation involves reactants and products. In phase equilibrium the concentrations on both sides of the reaction are time invariant.

Introducing the chemical potential μ as the partial molar free energy of a chemical species of a mixture with n species each one having N_i moles we have:

$$dG = -SdT + Vdp + \sum_{i=1}^{n} \mu_i dN_i$$

At thermal and mechanical equilibrium it reduces to:

$$dG = \sum_{i=1}^{n} \mu_i dN_i$$

Thus each of the μ_i of species i is explicitly defined as,

$$\mu_i = \left.\frac{\partial G}{\partial N_i}\right)_{T,P}$$

At phase equilibrium, the system Gibbs free energy reaches its minimum. It means,

$$dG = 0\ .$$

Which by the above definition gives,

$$\sum_{i=1}^{n} \mu_i dN_i = 0\,.$$

Considering a liquid vapor phase change situation,

$$\mu_L dN_L + \mu_g dN_g = 0$$

Mass conservation implies,

$$dN_L + dN_g = 0,$$

as the liquid and gas molar masses are equal.

Therefore,

$$\left(\mu_L - \mu_g\right) dN_L = 0$$

Close to equilibrium dN_L is small but non zero. The phase equilibrium condition consequently reads,

$$\mu_L = \mu_g\,.$$

Defining $g_k = \frac{\mu_k}{\hat{M}_k}$ it also reads,

$$g_L(P,T) = g_g(P,T)\,.$$

Conclusion générale

Un solveur de Riemann diphasique de type HLLC, à la fois simple, robuste et précis a été développé pour une variante symétrique du modèle de Baer et Nunziato (1986). La méthode numérique présentée a été validée sur des solutions exactes et des données expérimentales, ainsi que sur la méthode de référence jusqu'alors (Abgrall et Saurel, 2003). Elle est apparue plus efficace que cette dernière. La nouvelle méthode a ensuite été développée en 3D sur maillages non-structurés.

La construction d’une technique numérique pour la répartition de l’énergie d’une onde de choc dans les différentes phases constituant le milieu a par ailleurs été établie. Les conditions de choc multiphasiques sont ainsi respectées. En particulier, une procédure robuste et efficace de détection des chocs a été proposée et étendue aux maillages 3D non-structurés.

L’extension à un nombre arbitraire de phase du solveur de Riemann de type HLLC a été réalisée, permettant ainsi la simulation d’une plus large gamme d’applications.

Enfin, un modèle de transfert de chaleur et de masse dans un brouillard de gouttes ou nuage de bulles, en présence d’effets couplés de diffusion thermique et massique, a été proposé et dévoile des résultats intéressants. Le modèle a par la suite été intégré dans le code 3D non-structuré. Cela a permis la simulation de l’explosion d’une charge cylindrique placée à l’air libre. Les conditions violentes imposées dans ce cas-test ont permis de confirmer la robustesse du modèle de transition de phase proposé.

Le solveur de Riemann multiphasique proposé dans le cadre de cette thèse est envisagé comme « moteur hyperbolique » pour la simulation numérique d'autres phénomènes physiques. Par exemple, lorsque l’un des milieux est granulaire et que des pressions et énergies de 'configuration' apparaissent. Le modèle d'écoulement granulaire réactif envisagé est développé dans Saurel et al. (2014). Il sera considéré par la suite pour le traitement de l’allumage d’explosifs par collapse viscoplastique de pores et la transition déflagration-détonation dans ces milieux.

Enfin, la formulation implicite du schéma pourra être envisagée afin d’améliorer la rapidité du code 3D.

Références

R. Abgrall and R. Saurel, Discrete equations for physical and numerical compressible multiphase mixtures, J. Comput. Phys. 186 (2003) 361–396.

B. Abramzon and S. Sazhin, Droplet vaporization model in the presence of thermal radiation. International Journal of Heat and Mass Transfer, 48(9) (2005) 1868-1873

B. Abramzon and W. A. Sirignano, Droplet vaporization model for spray combustion calculations. International journal of heat and mass transfer, 32(9) (1989) 1605-1618

A. Ambroso, C. Chalons and P.-A. Raviart, A Godunov-type method for the seven-equation model of compressible two-phase flow, Computers and Fluids 54 (2012) 67–91

N. Andrianov and G. Warnecke, The Riemann problem for the Baer–Nunziato model of two-phase flows, J. Comput. Phys. 195 (2004) 434–464

M. R. Baer and J.W. Nunziato, A two-phase mixture theory for the deflagration-to-detonation transition (DDT) in reactive granular materials, J. Multiphase Flow 12 (1986) 861–889

DJ. Benson, Computational methods in Lagrangian and Eulerian hydrocodes, Computer Methods in Applied Mechanics and Engineering 99 (1992) 235-394

R. R. Bernecker and D. Price, Studies in the transition from deflagration to detonation in granular explosives – III – Proposed mechanisms for transition and comparison with other proposals in the literature, Combust. Flame, 22 (1974) p. 161

R. A. Berry, R. Saurel and O. Le Metayer, The discrete equation method (DEM) for fully compressible, two-phase flows in ducts of spatially varying cross-section, Nuclear Engineering and Design 240 (2010) 3797-3818

F. Bouchut, Nonlinear stability of finite volume methods for hyperbolic conservation laws, and well-balanced schemes for sources, Frontiers in Mathematics series, Birkhäuser, 2004

C-H. Chang and M-S. Liou, A robust and accurate approach to computing compressible multiphase flow: Stratified flow model and AUSM+-up scheme, J. Comput. Phys. 225 (2007) 840-873

A. Chinnayya, E. Daniel and R. Saurel, Computation of detonation waves in heterogeneous energetic materials, Journal of Computational Physics 196 (2004) 490–538.

R. Clift, J.R. Grace and M.E. Weber, Bubbles, drops, and particles. Academic Press (1978)

R. Courant and K. O. Friedrichs, Supersonic flow and shock waves, Interscience Publishers Inc. (1948)

S. F. Davis, Simplified second-order Godunov-type methods. SIAM J. Sci. and Stat. Comput. 9:445 (1988)

V. Deledicque and M.V. Papalexandris, An exact Riemann solver for compressible two-phase flow models containing non-conservative products, J. Comput. Phys. 222 (2007) 217–245

M. Dumbser, A. Hidalgo, M. Castro, C. Parés and E.F. Toro, FORCE Schemes on Unstructured Meshes II: NonConservative Hyperbolic Systems, Computer Methods in Applied Mechanics and Engineering, 199 (2010) 625-647

M. Dumbser and E.F. Toro, A Simple Extension of the Osher Riemann Solver to Non-Conservative Hyperbolic Systems, Journal of Scientific Computing, 48 (2011) 70-88

S. Ergun, Fluid flow through packed columns, Chem Eng Progress 48 (1952)

C. Farhat and FX. Roux, A method for finite element tearig and interconnecting and its parallel solution algorithm, International Journal for Numerical Methods in Engineering 32 (1991) 1205-1227

N. Frossling, Evaporation, heat transfer, and velocity distribution in two-dimensional and rotationally symmetrical laminar boundary-layer flow. NASA Langley Report, USA (1956)

SK. Godunov, A finite difference method for numerical calculation of discontinuous solutions of the equation of fluid dynamics, Matematicheskii Sbornik 47 (1959) 271–306

A. Harten, P. Lax and B. van Leer, On upstream differencing and Godunov-type schemes for hyperbolic conservation laws. SIAM (1983), Rev. 25, 35-61

T. Y. Hou and P. G. LeFloch, Why nonconservative schemes converge to wrong solutions: error analysis, Math. Comp. 62 (1994) 497-530

A. K. Kapila, R. Menikoff, J.B. Bdzil, S.F. Son and D.S. Stewart, Two-phase modeling of deflagration-to-detonation transition in granular materials: reduced equations, Physics of Fluids 13 (10) (2001) 3002–3024

R. Klein, Multiple spatial scales in engineering and atmospheric low Mach number flows. ESAIM: Mathematical Modelling and Numerical Analysis, 39(03) (2005) 537-559

M-H. Lallemand and R. Saurel, Pressure relaxation procedures for multiphase compressible flows, INRIA Report 4038 (2000)

C. K. Law, Recent advances in droplet vaporization and combustion. Progress in energy and combustion science, 8(3) (1982) 171-201

O. Le Metayer, J. Massoni and R. Saurel, Elaborating equations of state of a liquid and its vapor for two-phase flow models; Elaboration des lois d'état d'un liquide et de sa vapeur pour les modèles d'écoulements diphasiques. International Journal of Thermal Sciences, 43(3) (2004) 265-276

O. Le Metayer, J. Massoni and R. Saurel, Modeling evaporation fronts with reactive Riemann solvers, Journal of Computational Physics 205 (2005) 567–610.

O. Le Metayer, and R. Saurel, An alternative to cubic equations of state: The Noble-Abel-“Stiffened gas” equation of state. Int. J. Thermal Sciences (2015) submitted

Q. Li, H. Feng, T. Cai and C. Hu, Difference scheme for two-phase flow, Applied Mathematics and Mechanics 25 (2004) 536–545

S. Liang, W. Liu and L. Yuan, Solving seven-equation model for compressible two-phase flow using multiple GPUs, Computers & Fluids 99 (2014) 156-171.

S. P. Marsh, LASL Shock Hugoniot Data, University of California Press (1980) 658 pages

W. Mulder, S. Osher and JA. Sethian, Computing interface motion: The compressible Rayleigh-Taylor and Kelvin-Helmholtz instabilities, Journal of Computational Physics 100 (1992) 209

C. Parés, Numerical methods for nonconservative hyperbolic systems: a theoretical framework, SIAM J. Numer. Anal. 44 (2006) 300–321.

F. Petitpas, E. Franquet, R. Saurel and O. Le Metayer, A relaxation-projection method for compressible flows. Part II: Artificial heat exchanges for multiphase shocks. Journal of Computational Physics, 225(2) (2007) 2214-2248

F. Petitpas, R. Saurel, E. Franquet and A. Chinnayya, Modelling detonation waves in condensed energetic materials: Multiphase CJ conditions and multidimensional computations. Shock waves, 19(5) (2009) 377-401

M. Pilch and C.A. Erdman, Use of breakup time data and velocity history data to predict the maximum size of stable fragments for acceleration-induced breakup of a liquid drop. Int. J. Multiphase Flow, 13(6) (1987) 741-757

J. Robert, Chemkin-II: A Fortran chemical kinetics package for the analysis of gas-phase chemical kinetics. Sandia National Laboratories Report, SAND89-8009B (1989)

X. Rogue, G. Rodriguez, J.F. Haas and R. Saurel, Experimental and numerical investigation of the shock-induced fluidization of a particle bed, Shock Waves, 8 (1998), pp. 29–45

R. Saurel and R. Abgrall, A multiphase Godunov method for compressible multifluid and multiphase flows, J. Comput. Phys. 150 (1999) 425–467

R. Saurel, S. Gavrilyuk and F. Renaud, A multiphase model with internal degrees of freedom: application to shock–bubble interaction. Journal of Fluid Mechanics (2003), 495, pp 283-321

R. Saurel, S. Le Martelot, R. Tosello and E. Lapébie, Symmetric model of compressible granular mixtures with permeable interfaces, Physics of Fluids 26(12) (2014) 123304

R. Saurel, O. Le Metayer, J. Massoni and S. Gavrilyuk, Shock jump relations for multiphase mixtures with stiff mechanical relaxation, Shock Waves 16 (3) (2007) 209–232

R. Saurel, F. Petitpas and R. Abgrall, Modelling phase transition in metastable liquids: application to cavitating and flashing flows. Journal of Fluid Mechanics, 607 (2008) 313-350

R. Saurel, F. Petitpas and R. A. Berry, Simple and efficient relaxation methods for interfaces separating compressible fluids, cavitating flows and shocks in multiphase mixtures, J. Comput. Phys. 228 (2009) 1678-1712

S. Schoch, N. Nikiforakis, B. J. Lee and R. Saurel, Multi-phase simulation of ammonium nitrate emulsion detonations, Combustion and Flame 160, Issue 9 (2013) 1883-1899

D.W. Schwendeman, C.W. Wahle and A.K. Kapila, The Riemann problem and a high-resolution Godunov method for a model of compressible two-phase flow, J. Comput. Phys. 212 (2006) 490–526

W.A. Sirignano, Advances in droplet array combustion theory and modeling. Progress in Energy and Combustion Science, 42 (2014) 54-86

D.B. Spalding, The combustion of liquid fuels. In Symposium (Int.) on combustion 4(1) (1953) 847-864

S. Tokareva and E. F. Toro, HLLC-type Riemann solver for the Baer-Nunziato equations of compressible two-phase flow, J. Comput. Phys. 229 (2010) 3573–3604

E.F. Toro, A weighted average flux method for hyperbolic conservation laws. Proceedings of the Royal Society of London. A. Mathematical and Physical Sciences, vol. 423, num 1865 (1989) 401-418.

E. F. Toro, Riemann Solvers and Numerical Methods for Fluid Dynamics, Springer-Verlag, 1997

E.F. Toro, S.J. Billet, Centered TVD schemes for hyperbolic conservation laws, IMA J. Numer. Anal. 20 (2000) 44–79

E.F. Toro, M. Spruce and W. Speares, Restoration of the contact surface in the HLL-Riemann solver, Shock Waves 4 (1994) 25–34

B. Van Leer, Toward the ultimate conservation difference scheme V, A second order sequel to Godunov's method. J Comput Phys 32 (1979) 101–136

F.A. Williams, Spray combustion and atomization. Physics of Fluids 1(6) (1958) 541-545

A. Zein, M. Hantke and G. Warnecke, Modeling phase transition for compressible two-phase flows applied to metastable liquids, J. Comput. Phys. 229 (2010) 2964–2998